DOE/NV/0000939-41

Investigating the Influence of Regional Stress on Fault and Fracture Permeability at Pahute Mesa, Nevada National Security Site

Prepared by

Donald M. Reeves, Kenneth D. Smith, Rishi Parashar,
Cheryl Collins, and Kevin M. Heintz

Submitted to

Nevada Field Office
National Nuclear Security Administration
U.S. Department of Energy
Las Vegas, Nevada

May 2017

Publication No. 45275

Nevada System of Higher Education

Reference herein to any specific commercial product, process, or service by trade name, trademark, manufacturer, or otherwise, does not necessarily constitute or imply its endorsement, recommendation, or favoring by the United States Government or any agency thereof or its contractors or subcontractors.

Available for sale to the public from:

U.S. Department of Commerce
National Technical Information Service
5301 Shawnee Rd.
Alexandria, VA 22312
Phone: 800.553.6847
Fax: 703.605.6900
Email: orders@ntis.gov
Online ordering: http://www.osti.gov/ordering.htm

Available electronically at http://www.osti.gov/bridge.

Available for a processing fee to the U.S. Department of Energy and its contractors, in paper, from:

U.S. Department of Energy
Office of Scientific and Technical Information
P.O. Box 62
Oak Ridge, TN 37831-0062
Phone: 865.576.8401
Fax: 865.576.5728
Email: reports@adonis.osti.gov

DOE/NV/0000939-41

Investigating the Influence of Regional Stress on Fault and Fracture Permeability at Pahute Mesa, Nevada National Security Site

Prepared by

Donald M. Reeves[1], Kenneth D. Smith[2], Rishi Parashar[3],
Cheryl Collins[4], and Kevin M. Heintz[5]

[1]Department of Geosciences, Western Michigan University, Kalamazoo, MI 49008
[2] Nevada Seismological Laboratory, University of Nevada, Reno, NV 89503
[3]Division of Hydrologic Sciences, Desert Research Institute, Reno, NV 89512
[4]Division of Earth and Ecosystem Sciences, Desert Research Institute, Las Vegas, NV 89119
[5]Division of Hydrologic Sciences, Desert Research Institute, Las Vegas, NV 89119

Publication No. 45275

Submitted to
Nevada Field Office
National Nuclear Security Administration
U.S. Department of Energy
Las Vegas, Nevada

May 2017

The work upon which this report is based was supported by the U.S. Department of Energy under Contract #DE-NA0000939. Approved for public release; further dissemination unlimited.

THIS PAGE IS LEFT INTENTIONALLY BLANK

EXECUTIVE SUMMARY

Regional stress may exert considerable control on the permeability and hydraulic function (i.e., barrier to and/or conduit for fluid flow) of faults and fractures at Pahute Mesa, Nevada National Security Site (NNSS). In-situ measurements of the stress field are sparse in this area, and short period earthquake focal mechanisms are used to delineate principal horizontal stress orientations. Stress field inversion solutions to earthquake focal mechanisms indicate that Pahute Mesa is located within a transtensional faulting regime, represented by oblique slip on steeply dipping normal fault structures, with maximum horizontal stress ranging from N29°E to N63°E and average of N42°E. Average horizontal stress directions are in general agreement with large diameter borehole breakouts from Pahute Mesa analyzed in this study and with stress measurements from other locations on the NNSS.

A computer code, RStress, was developed to compute dilation and slip tendency on 394 faults and structural features obtained from the Phase II Pahute Mesa Hydrostratigraphic Framework model (NSTec, 2014) and USGS Slate *et al.* (1999) fault map. RStress incorporates stress field inversion data from earthquake focal mechanisms and uses a traction vector method to resolve normal and shear stresses acting on fault planes of any orientation for both average and space-varying horizontal stress directions. Faults with the highest dilation tendency trend NE-SW for both average and space-varying stress field solutions, and are lowest for NW-SE structures. Differences between dilation and slip tendency values for constant versus space-varying stress field are greatest in the region with the highest density of faults and stress field inversion solutions.

Uncertainty with respect to horizontal stress anisotropy in dilation and slip tendency values is addressed through the use of three maximum to minimum horizontal stress ratios of 1.5, 2.5, and 3.2. These ratios are based on stress magnitudes estimated on the NNSS from overcoring and hydraulic fracturing methods, with the 1.5 ratio obtained from the hydraulic fracturing study of Stock *et al.* (1985) serving as the most likely base case. Horizontal stress anisotropy strongly influences slip tendency values and minimally influences values of dilation tendency. The analysis indicates that none of the faults considered in this study are critically stressed under the more likely 1.5 and 2.5 horizontal stress anisotropy ratios, and that approximately 28 percent of faults are critically stressed under the unrealistically high horizontal stress anisotropy ratio of 3.2. Given the lack of critically stressed structures, the most likely mechanism for enhanced permeability of faults and fractures is aperture dilation as a result of minimal normal stress. This occurs for steeply dipping structures oriented in the direction of maximum horizontal stress.

Identification of faults and geologic structures that are likely enhanced for flow uses all three horizontal stress anisotropy ratios for full inclusion of uncertainty. Approximately 40 percent (157 of 394) of the faults and structural features analyzed are predicted to have enhanced flow. Of the 157 structures designated for enhanced fluid flow, 90 percent of the structures have high values of dilation tendency, whereas only 37 percent of these structures are critically stressed for slip (all using the 3.2 ratio). These results imply that the resolution of normal stress acting on fault planes may exert more influence on fault permeability than shear stress. Low slip rates of faults with Quaternary displacement on the NNSS, relative to other higher slip rates outside of the NNSS, support the lack of critically stressed faults computed in this study for Pahute Mesa.

The potential influence of the stress field on smaller, background fractures was investigated by analyzing hydraulic responses in ER-EC-1, ER-EC-2A, ER-EC-4, ER-EC-5, ER-EC-6, ER-EC-7 and ER-EC-8 from Oberlander *et al.* (2002). A total of 294 fractures were detected in these boreholes with an approximately 40 percent of these fractures located within screened intervals of the wells. Orientations of the borehole fractures are generally representative of the orientations of the major faults in the combined map, although the dip of the borehole fractures are less than the regional faults. A total of 25 conductive fractures, most of which are located in lava and welded tuff units, are correlated to locations of fluid inflow to the wells. Only a single fracture out the 25 conductive fracture population is considered enhanced for fluid flow on the basis of orientation, and the combination of the random pattern in orientation and low dilation tendency values for the other 24 conductive fractures suggest that the stress field does not play a significant role in influencing fluid flow through smaller, background fractures at the borehole scale. This may be explained by the dominance of cooling fractures within lava and welded tuff units, which create complex connectivity patterns for fluid flow that are unrelated to and minimally influenced by tectonic stress.

ACKNOWLEDGEMENTS

The authors would like to acknowledge the contributions of Mr. Wyatt Fereday in compiling existing stress field measurements on the NNSS. The authors would also like to thank Markus Berli, Karl Pohlmann, and Chuck Russell from the Desert Research Institute; Sharad Kelkar and Kenneth Rehfeldt from Navarro Research and Engineering; and Donald Sweetkind from the U.S. Geological Survey for their helpful review comments that significantly strengthened the quality of this report.

THIS PAGE IS LEFT INTENTIONALLY BLANK

CONTENTS

EXECUTIVE SUMMARY iii
ACKNOWLEDGEMENTS v
LIST OF FIGURES viii
LIST OF TABLES xi
LIST OF ACRONYMS xi
INTRODUCTION 1
STRESS FIELD CHARACTERIZATION 2
Earthquake Focal Mechanisms 2
Focal Mechanisms Determination 2
Focal Mechanisms Data 5
Stress Field Inversions 6
NNSS Stress Field Directions and Magnitudes 9
HYDRAULIC FUNCTION OF FAULT AND FRACTURES 15
Fault Dilation and Slip Tendency 16
Dilation and Slip Tendency 23
Trends in Dilated and Critically Stressed Faults 23
Spatial Trends in Dilation Tendency 27
Spatial Trends in Slip Tendency 36
Influence of Constant versus Variable Stress Field 43
PM Faults Dilated or Critically Stressed for Fluid Flow 46
ANALYSIS OF HYDRAULIC TESTS 58
Borehole Fracture Orientation 58
Borehole Inflow Responses 63
ER-EC-1 64
ER-EC-2A 65
ER-EC-4 66
ER-EC-5 67
ER-EC-6 68
ER-EC-8 69
Correspondence between Borehole Inflow Tends and Fractures 70
SUMMARY AND CONCLUSIONS 75

REFERENCES 77
APPENDIX A: Hamilton Earthquake Focal Mechanisms A-1
APPENDIX B: SATSI Stress Field Inversion B-1
APPENDIX C: RStress Dilation and Slip Tendency Verification C-1
APPENDIX D: Compiled Dilation and Slip Tendency Values D-1

LIST OF FIGURES

1. Short period seismograph stations operated by the USGS from 1978 through September 1992 used in developing the regional catalog and earthquake focal mechanisms. 3
2. Digital seismograph network operated by the Nevada Seismological Laboratory for Yucca Mountain Project site characterization. Implemented in 1996. 4
3. Short period focal mechanisms in the northwest NNSS region used in the stress inversion and compiled from various sources along with NNSS boundary and individual CAUs. 5
4. SATSI output T-axis and P-axis orientations along with NNSS boundary and individual CAUs. 7
5. SATSI output T-axis and P-axis orientations along with NNSS boundary and individual CAUs. 8
6. Relationships of borehole breakouts to minimum and maximum horizontal stress and downhole image of borehole elongation and breakout from circular trend 10
7. Location of large diameter boreholes and ER-EC wells used in this study. 12
8. Zoomed in version of Figure 7 with individual labels given to large diameter boreholes and ER-EC wells. 13
9. Representation of the Cauchy stress tensor on an arbitrary Cartesian coordinate system. 17
10. Free body diagram of a tetrahedral portion of a material showing traction vector in relation to the unit normal vector acting on the plane and the stress field. 18
11. Pahute Mesa Phase II structure and fault map. 20
12. Final fault map combining NSTec (2014) PM Phase II faults in Figure 8 with Slate *et al.* (1999) faults. 21
13. Spatial distribution of SATSI stress field inversion solutions to focal mechanisms within PM (n = 91). 22
14. Southern-hemisphere, equal-area stereonet plot of poles to planes of fault dilation tendency given average horizontal stress directions computed from SATSI solutions with locations shown in Figure 9 with S_{Hmax}/S_{hmin} = 1.5 and S_{Hmax}/S_{hmin} = 4.0. 24

15. Southern-hemisphere, equal-area stereonet plot of poles to planes of fault slip tendency given average horizontal stress directions computed from SATSI solutions with locations shown in Figure 9 with S_{Hmax}/S_{hmin} = 1.5 and S_{Hmax}/S_{hmin} = 4.0. 25

16. Fault dilation tendency given average horizontal stress directions computed from SATSI solutions for low horizontal stress anisotropy: S_{Hmax}/S_{hmin} = 1.5. 28

17. Fault dilation tendency given spatially variable horizontal stress directions from SATSI solutions for low horizontal stress anisotropy: S_{Hmax}/S_{hmin} = 1.5. 29

18. Difference in fault dilation tendency, expressed as percent error, between constant and spatially variable SATSI solutions for low horizontal stress anisotropy: S_{Hmax}/S_{hmin} = 1.5. 30

19. Fault dilation tendency given average horizontal stress directions computed from SATSI solutions for moderate horizontal stress anisotropy: S_{Hmax}/S_{hmin} = 2.5. 31

20. Fault dilation tendency given spatially variable horizontal stress directions from SATSI solutions for moderate horizontal stress anisotropy: S_{Hmax}/S_{hmin} = 2.5. 32

21. Fault dilation tendency given average horizontal stress directions computed from SATSI solutions for high horizontal stress anisotropy: S_{Hmax}/S_{hmin} = 3.2. 33

22. Fault dilation tendency given spatially variable horizontal stress directions from SATSI solutions for high horizontal stress anisotropy: S_{Hmax}/S_{hmin} = 3.2. 34

23. Slip tendency given average horizontal stress directions computed from SATSI solutions for low horizontal stress anisotropy: S_{Hmax}/S_{hmin} = 1.5. 35

24. Slip tendency given spatially variable horizontal stress directions from SATSI solutions for low horizontal stress anisotropy: S_{Hmax}/S_{hmin} = 1.5. 37

25. Difference in fault slip 3tendency, expressed as percent error, between constant and spatially variable SATSI solutions for low horizontal stress anisotropy: S_{Hmax}/S_{hmin} = 1.5. 38

26. Slip tendency given average horizontal stress directions computed from SATSI solutions for moderate horizontal stress anisotropy: S_{Hmax}/S_{hmin} = 2.5. 39

27. Slip tendency given spatially variable horizontal stress directions from SATSI solutions for moderate horizontal stress anisotropy: S_{Hmax}/S_{hmin} = 2.5. 40

28. Slip tendency given average horizontal stress directions computed from SATSI solutions for high horizontal stress anisotropy: S_{Hmax}/S_{hmin} = 3.2. 41

29. Slip tendency given spatially variable horizontal stress directions from SATSI solutions for high horizontal stress anisotropy: S_{Hmax}/S_{hmin} = 3.2. 42

30. Probability histogram showing difference in distribution of dilation tendency values and slip tendency values computed using average stress field versus spatially variable stress field for S_{Hmax}/S_{hmin} = 1.5. Overlap is shown in gray. 44

31. Probability histogram showing difference in distribution of dilation tendency values and slip tendency values computed using average stress field versus spatially variable stress field for S_{Hmax}/S_{hmin} = 3.2. 44

32. Plot of average dilation tendency values for all 394 faults for variable versus constant stress directions given S_{Hmax}/S_{hmin} = 1.5. 45

33. Plot of average dilation tendency values for all 394 faults for variable versus constant stress directions given S_{Hmax}/S_{hmin} = 3.2. 45

34. Southern-hemisphere, equal-area projection of all fracture planes logged in boreholes ER-EC-1, ER-EC-2A, ER-EC4, ER-EC-5, ER-EC-6, ER-EC-7 and ER-EC-8 wells to poles and contours of poles to planes. 59

35. Southern-hemisphere, equal-area projection of all fracture planes logged in boreholes ER-EC-1, ER-EC-2A, ER-EC4, ER-EC-5, ER-EC-6, ER-EC-7 and ER-EC-8 wells to poles with dilation and slip tendency values for S_{Hmax}/S_{hmin} = 1.5. 60

36. Southern-hemisphere, equal-area projection of all fracture planes logged in boreholes ER-EC-1, ER-EC-2A, ER-EC4, ER-EC-5, ER-EC-6, ER-EC-7 and ER-EC-8 wells to poles with dilation and slip tendency values for S_{Hmax}/S_{hmin} = 2.5. 60

37. Southern-hemisphere, equal-area projection of all fracture planes logged in boreholes ER-EC-1, ER-EC-2A, ER-EC4, ER-EC-5, ER-EC-6, ER-EC-7 and ER-EC-8 wells to poles with dilation and slip tendency values for S_{Hmax}/S_{hmin} = 3.2. 61

38. Histogram of dilation tendency values and slip tendency values, respectively, for all large-scale faults and structures shown in Figure 12, and dilation and slip tendency values for all borehole fractures, respectively for S_{Hmax}/S_{hmin} = 1.5. 61

39. Histogram of dilation tendency values and slip tendency values, respectively, for all large-scale faults and structures shown in Figure 12, and dilation and slip tendency values for all borehole fractures, respectively for S_{Hmax}/S_{hmin} = 3.2. 62

40. ER-EC-1 borehole inflow rates during pumping at 0.48 m^3/min, and resultant distribution of hydraulic conductivity along borehole derived from Rehfeldt *et al.* (1989) approach 65

41. ER-EC-2A borehole inflow rates during pumping at 0.65 m^3/min, and resultant distribution of hydraulic conductivity along borehole derived from Rehfeldt *et al.* (1989) approach 66

42. ER-EC-4 borehole inflow rates during pumping at 0.70 m^3/min, and resultant distribution of hydraulic conductivity along borehole derived from Rehfeldt *et al.* (1989) approach 67

43. ER-EC-5 borehole inflow rates during pumping at 0.61 m^3/min, and resultant distribution of hydraulic conductivity along borehole derived from Rehfeldt *et al.* (1989) approach 68

44. ER-EC-6 borehole inflow rates during pumping at 0.48 m^3/min, and resultant distribution of hydraulic conductivity along borehole derived from Rehfeldt *et al.* (1989) approach 69

45. ER-EC-8 borehole inflow rates during pumping at 0.67 m^3/min, and resultant distribution of hydraulic conductivity along borehole derived from Rehfeldt *et al.* (1989) approach 70

46. Southern-hemisphere, equal-area projection of 25 conducive fracture planes to poles with dilation tendency for S_{Hmax}/S_{hmin} = 1.5 and slip tendency for S_{Hmax}/S_{hmin} = 3.2. 74

LIST OF TABLES

1. NNSS compilation of average maximum horizontal stress directions. 9
2. Average breakout orientation data (N = 0°) from large diameter boreholes. 11
3. Stress magnitudes (MPa) for the NNSS listed in order of depth below land surface. 14
4. Dilation and slip tendencies for constant stress field. 25
5. Dilation and slip tendencies for spatially variable stress field. 26
6. Root mean square deviation between dilation and slip tendency values for constant and variable stress directions expressed as a percent. 43
7. Average values of dilation and slip tendency for the low, moderate and high stress anisotropy ratios, denoted as S_{Hmax}/S_{hmin} equal to 1.5, 2.5, and 3.2, respectively, for PM Phase II structures. 46
8. Number of dilated fractures computed for each borehole. 62
9. Sharp, diffuse and no inflow categories for screened intervals. 72
10. Conductive fractures identified in the ER-EC wells. 73
11. Detailed fracture statistics over the entire screened intervals with discrete inflows. . 74

LIST OF ACRONYMS

bls	below land surface
CAU	Corrective Action Unit
DFN	discrete fracture network
DOE	Department of Energy
ft	feet
in	inch
HSU	hydrostratigraphic unit
km	kilometer
m	meter
mm/yr	millimeters per year
NE-SW	northeast-southwest
NNSS	Nevada National Security Site

NSL	Nevada Seismological Laboratory
NTS	Nevada Test Site
NW-SE	northwest-southeast
PM	Pahute Mesa
RMSD	root mean square deviation
SATSI	Spatial and Temporal Stress Inversion
UNE	Underground Nuclear Explosion
UNR	University of Nevada, Reno
USGS	U.S. Geological Survey

INTRODUCTION

It is widely known that regional stress often exerts considerable influence on the permeability of faults and joints (e.g., Barton and Zoback [1995], National Research Council [1996], Jaeger *et al.* [1997], Ferrill *et al.* [1999], and Zoback [2010]). Interactions between regional stress and fracture permeability may be particularly important within the Central and Western Pahute Mesa Corrective Action Units (CAUs) on the Nevada National Security Site (NNSS), where radionuclides have migrated on the scale of 100s of meters from the TYBO and BENHAM tests through interconnected fault and fracture networks (Pawloski *et al.*, 2010). Inclusive treatment of all relevant processes affecting fluid flow and radionuclide migration in these CAUs necessitates that conceptual and numerical models consider how regional stress may affect fracture permeability and resultant ground water velocities that govern radionuclide transport.

Stress measurements have been collected at various locations on the NNSS, including Climax Mine-Yucca Flat, Central and Western Pahute Mesa, Rainier Mesa, and Yucca Mountain (Carr, 1974; Haimson, 1981; Smith *et al.*, 1981; Springer and Thorpe, 1981; Ellis, 1982; Springer *et al.*, 1984; Stock *et al.*, 1985; Gillson, 1987; Minor, 1989; Warpinski and Teufel, 1991; Lee and Haimson, 1999). These stress data were collected and/or inferred using a variety of methods, including: borehole breakouts, earthquake focal mechanisms, fault kinematics, hydraulic fracturing, and overcoring in boreholes and tunnel complexes. Only Springer and Thorpe (1981) and Gillson (1987) in the above list are specific to Pahute Mesa, and use borehole breakouts to infer local directions of minimum and maximum horizontal stress and do not estimate stress magnitudes. The most reliable estimates of stress magnitudes for the NNSS are based on hydraulic fracturing experiments at approximately 1 km depth for two Yucca Mountain boreholes (Stock *et al.*, 1985).

Central and Western Pahute Mesa, collectively termed Pahute Mesa (PM) herein, form a structurally complex region comprised of multiple caldera margins and associated structural zones, numerous steeply dipping, northeast-southwest (NE-SW) and northwest-southeast (NW-SE) trending faults, and a smaller subset of faults associated with caldera collapse (Bechtel Nevada, 2002; National Nuclear Security Administration, 2009). The presence of multiple calderas within a relatively small region most likely cause local perturbations within the stress field where directions of minimum and maximum horizontal stress are spatially variable. Characterization of spatial heterogeneity within the stress field at PM cannot be captured by sparse breakout data alone, and stress field inversions based on earthquake focal mechanism data are used to compute horizontal stress directions at multiple locations.

This study is intended to support conceptual and numerical investigations of fluid flow and radionuclide migration within Pahute Mesa. The primary objectives are three-fold:

(1) Provide an updated, spatially variable interpretation of the regional stress field in Pahute Mesa through analysis and inversion of earthquake focal mechanisms.
(2) Infer hydraulic function of faults and smaller-scale fractures within Pahute Mesa based on concepts of fault dilation and slip tendency.
(3) Analyze trends of borehole inflow for selected ER-EC wells to evaluate the findings and inferences from the fault dilation and slip tendency analyses.

This report disseminates study findings on characterization of the stress field on the NNSS and PM using a combination of previous studies and stress field inversion data from short-period earthquake focal mechanisms, inferring hydraulic function of faults and fractures in the vicinity of PM through the computation of dilation and slip tendency metrics, and analyzing fracture and hydraulic inflow logs from selected ER-EC wells to test the utility of these inferences. The report is divided into three sections detailing: stress field characterization and associated uncertainty, determining hydraulic function of faults and fractures under varying stress field configurations, and analysis of fracture and inflow logs for five ER-EC wells. Additional information on earthquake focal mechanisms, stress inversions, verification of RStress computed fault dilation and slip tendency values, and dilation and slip tendency values computed for individual faults are provided as Appendices.

STRESS FIELD CHARACTERIZATION

Characterization of the stress field in this study consists of analyzing available first-motion earthquake focal mechanism data (developed almost exclusively from "short-period," 1 Hz, seismometers) for use in stress field inversions. Solutions to the stress field inversions serve as specific locations within Pahute Mesa where horizontal stress directions are estimated. These estimates, in conjunction with stress field magnitudes collected by Stock *et al.* (1985), are used in the numerical code RStress to compute dilation and shear tendency for compiled faults and structural features at PM. Uncertainty in stress directions and stress magnitudes is addressed through analyses using constant versus spatially variable stress fields and a data derived range of horizontal stress anisotropy ratios.

Earthquake Focal Mechanisms

The stress field in the northwest NNSS region was estimated from short-period focal mechanism data using the Spatial and Temporal Stress Inversion (SATSI) software application of Hardebeck and Michael (2006). First-motion focal mechanisms were compiled from a number of reports on Nevada Test Site (NTS) seismicity developed by the U.S. Geological Survey (USGS) and the Nevada Seismological Laboratory (NSL). Additional mechanisms (post-NTS area reports) were computed from the regional seismicity and phase arrival database maintained at NSL.

Focal Mechanisms Determination

Short-period first-motion focal mechanisms have been routinely determined under NTS and NNSS seismic monitoring activities. The modern period of earthquake monitoring began in 1978 when the USGS installed a regional short-period, primarily vertical component, seismic network in the southern Great Basin, motivated by Department of Energy (DOE) Yucca Mountain Project regional site characterization and NTS Underground Nuclear Explosion (UNE) monitoring (Figure 1). In 1992, the Nevada Seismological Laboratory (NSL) at the University of Nevada, Reno, (UNR) assumed operation of the NTS area network under the DOE Yucca Mountain Project (see Yucca Mountain seismicity report references). In 1996 the network was significantly changed with an upgrade to 3-Component digital seismographs with digital telemetry (Figure 2). Some short-period stations in the Death Valley area and northwest of NNSS were retained. This improved the data recording fidelity. However, many regional short-period monitoring stations used for focal mechanisms were removed as the focus shifted to Yucca Mountain area site-specific monitoring.

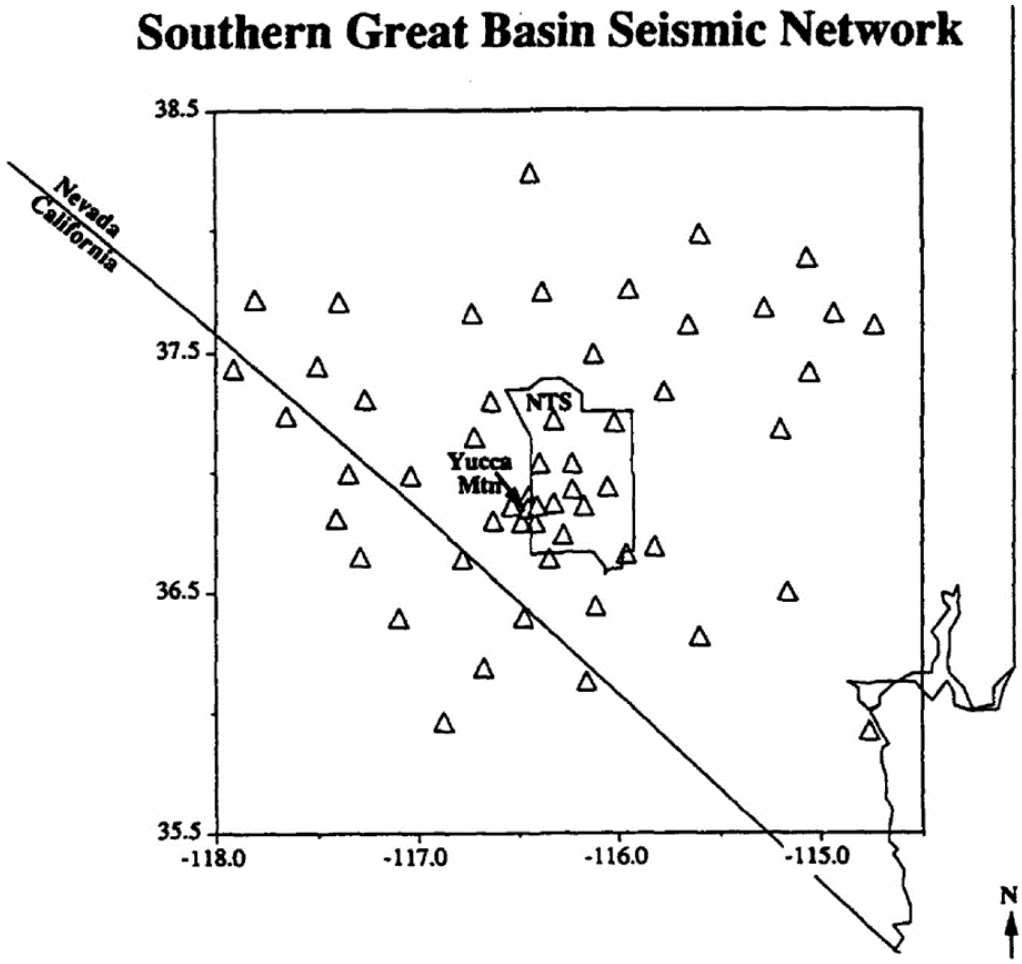

Figure 1. Short period seismograph stations operated by the USGS from 1978 through September 1992 used in developing the regional catalog and earthquake focal mechanisms (from Gomberg [1991]).

Prior to October 1992, earthquake focal mechanisms (USGS monitoring period) were provided in regular reports (see USGS seismicity report references). The regional earthquake catalog was developed using location routines HYPOELLIPSE (Lahr, 1979) and HYPOINVERSE (Klein, 2002; includes references to early versions of the software). During this period, short-period mechanisms were determined with focal mechanism software developed by Kisslinger *et al.* (1981), Snoke *et al.* (1984) and Reasenberg and Oppenheimer (1985; FPFIT). From October 1992 through October 2004, event locations were determined with HYPOINVERSE, and published in yearly reports. During this period, short-period mechanisms were determined with application FPFIT (Reasenberg and Oppenheimer, 1985). From October 2004 through present NSL developed the regional earthquake catalog using the Antelope (commercial network operations software; Boulder Real-Time Systems, Boulder, CO) location routines. Various velocity models have been used in developing the regional earthquake catalog, some being established under Quality Assurance programs. For this study, earthquakes since 2000 to present not included in regular reports, with 20 or more phase arrivals in the NW NNSS region, were reviewed and computed with software

applications HASH (Hardebeck and Shearer, 2002). Events with sufficient phase arrivals were selected from the NSL database and first motions were interactively determined. Software application HASH provides more flexibility than previous software used for determining earthquake focal mechanisms, allowing use of several velocity models and accepting a percentage of misfits in the solution. In any case, only solutions that returned a unique focal mechanism per event were used (uncertainties in the data can result in multiple solutions per event).

All of these software applications, event locations and focal mechanisms, apply slightly different approaches. However, well-constrained short period focal mechanisms depend on reliable events locations (particularly depth control) and identifiable polarities with good azimuthal control. Therefore, there is considerable variation in the constraints on first-motion short period mechanisms. Clearly, in comparing Figures 1 and 2, station coverage changed dramatically with the implementation of the digital network in 1996, sacrificing azimuthal control for regional short period mechanisms for improved recording quality. Despite changes in instrumentation and coverage, all event first motions have been reviewed by an analyst. Qualitatively, increased recording quality tends to compensate for reduced geographic coverage.

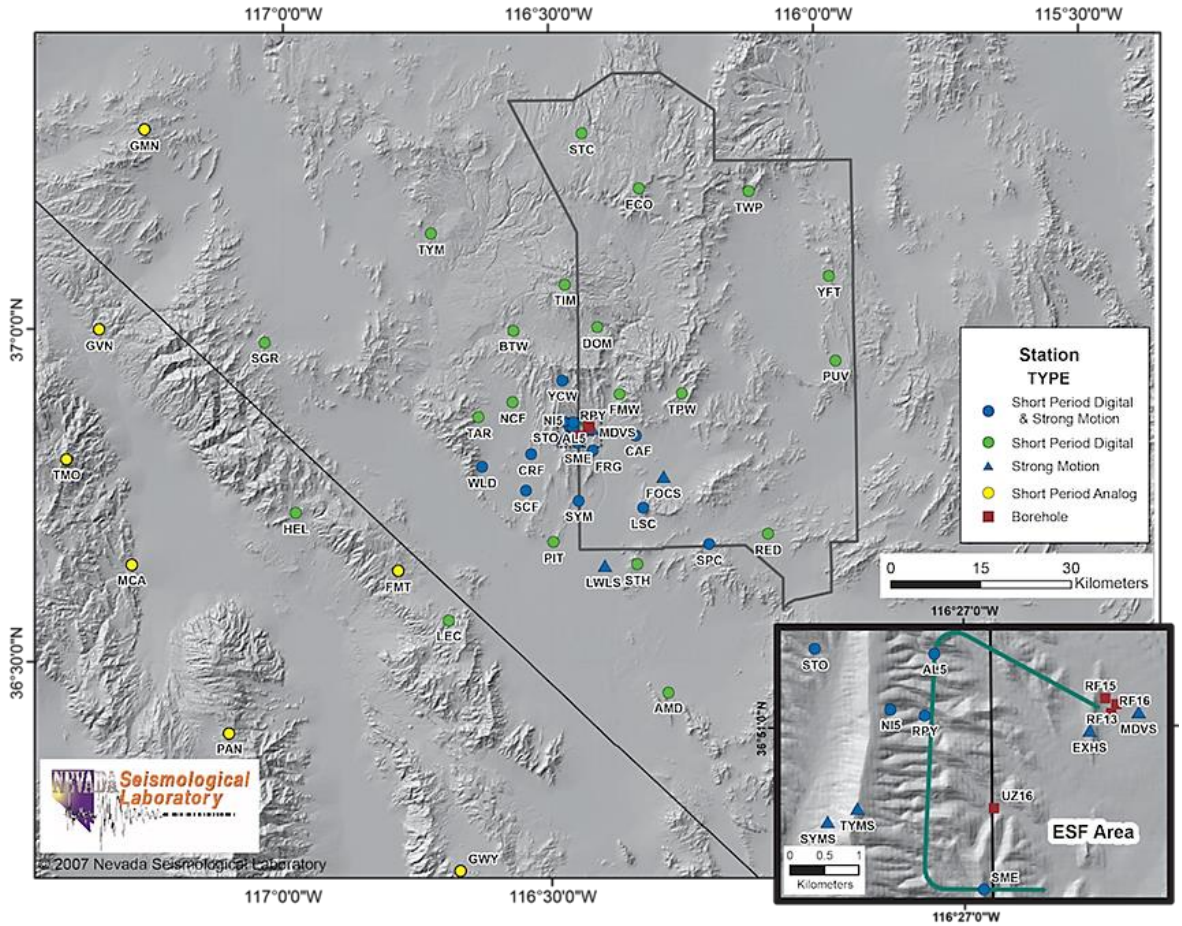

Figure 2. Digital seismograph network operated by the Nevada Seismological Laboratory for Yucca Mountain Project site characterization. Implemented in 1996.

Focal Mechanisms Data

Of the 699 focal mechanisms used in the stress inversion, 235 were determined during the USGS monitoring period using various software applications (Kisslinger *et al.*, 1981; Snoke *et al.*, 1984; Reasenburg and Oppenheimer, 1985), 263 were developed under NSL operations through 2004 from application FPFIT (Reasenburg and Oppenheimer, 1985), 50 were determined from the Hamilton *et al.* (1971) post-Benham explosion induced seismicity study (see Appendix A), and 151 were determined for this study using USGS software application HASH (Hardebeck and Shearer, 2002). Station coverage and uncertainties in the local velocity model will affect first-motion solutions. Ideally, a station within one focal depth will provide better event depth estimates. Unfortunately, these are limitations of the variable network coverage and event distribution in the Pahute Mesa area. Improvements can be made with more comprehensive event relocations (beyond the scope of this study). Stress axes orientations are recovered in a smoothed model through SATSI's weighted least squares approach with larger samples. Figure 3 shows beach ball diagrams of focal mechanisms in the northwest NNSS region. All focal mechanism data was reformatted to conform to input for application SATSI (Hardebeck and Michael, 2006).

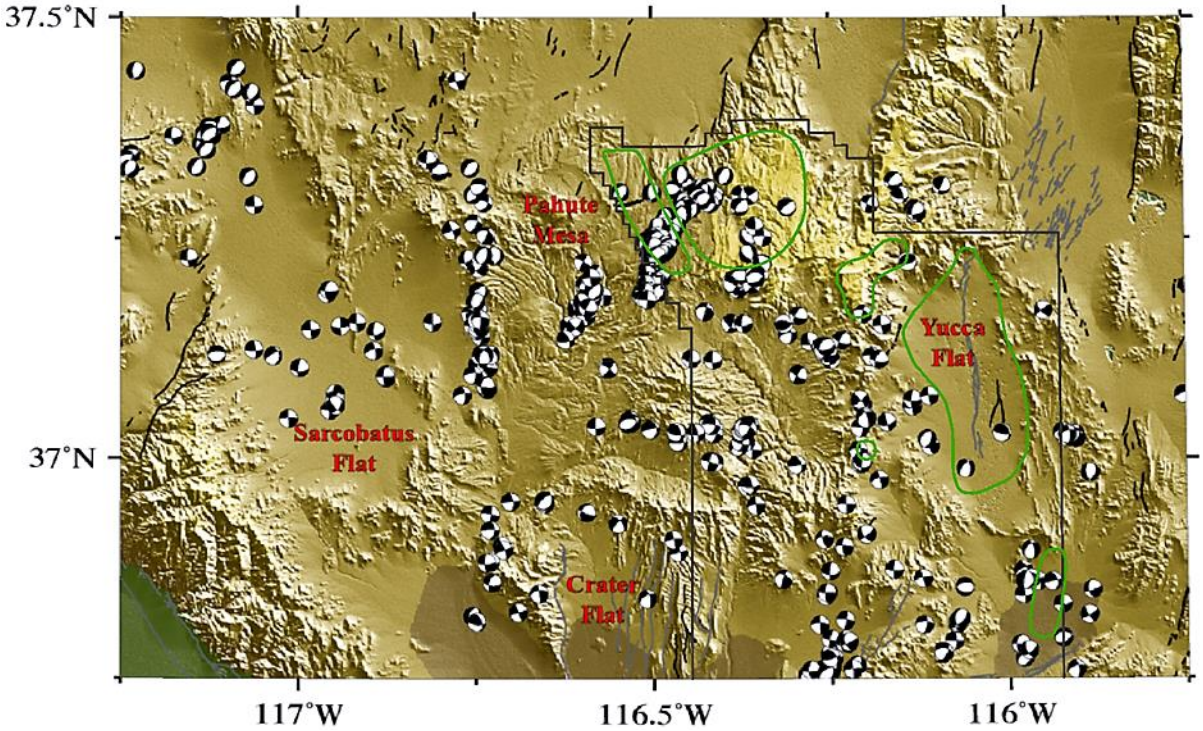

Figure 3. Short period focal mechanisms in the northwest NNSS region used in the stress inversion and compiled from various sources along with NNSS boundary (black line) and individual CAUs (green line). Western and Central Pahute Mesa CAUs are located in the northwest region of the NNSS.

Stress Field Inversions

The SATSI applies a damped least squares inversion method that minimizes the complexity of the stress field (principal stress axes and their uncertainties) by removing artifacts in a solution that incorporates heterogeneities in the stress field warranted by the data (Hardebeck and Michael, 2006). In contrast to other stress inversion methods that apply individual grid solutions or moving window smoothing, SATSI's damped inversion techniques forces a solution constrained to adjacent grid points assuring a result that is both smooth as well as accommodating local variability in the stress field. Although SATSI can be used for temporal and 3-D stress variations for large data sets of high-precision event locations, only the 2-D case is used here which captures variations in the orientation of the regional stress field. Because of the sparse sampling of the available focal mechanisms in the northwest NNSS area, an adapted smoothing strategy was applied to capture both the regional stress field as well as the local stress variations in clusters of resolvable mechanisms. This could be modified to capture sufficient focal mechanisms per grid point, in a distance search, however that has yet to be implemented. In the approach used here, SATSI requires at least three mechanisms per grid point to establish an estimate of the stress field and we used a default damping parameter of 1 (see Hardebeck and Michael, 2006). In all cases we assumed the actual fault plane (i.e., versus the auxiliary fault plane) could not be resolved. This is to be expected in a region of distributed transtensional deformation with sparse station coverage

The area of study is bounded by latitude: 36.75 to 37.50N; longitude: -117.00 to -116.00W in the northwest NNSS region. Grid spacing of 0.5 degrees, 0.1 degrees, 0.050 degrees, and 0.025 degrees were applied in individual stress inversions, and then concatenated to incorporate both estimates of the regional stress field, in areas of sparse coverage, and details of the local stress field where it is better sampled. The highest grid density estimate at a common point is taken as the stress field estimate at that grid point. This was applied to incorporate well sampled areas more effectively but still integrate measurement of the stress field in areas with limited data.

This effective adaptation allows us to use SATSI's inversion method to capture, as best as possible, an estimate of the orientation of the principal stress axes in the Pahute Mesa area. However, all independent variable grid density stress inversion results will be included in the final report. Figures 4 and 5 show results from the grid strategy applied in this study area.

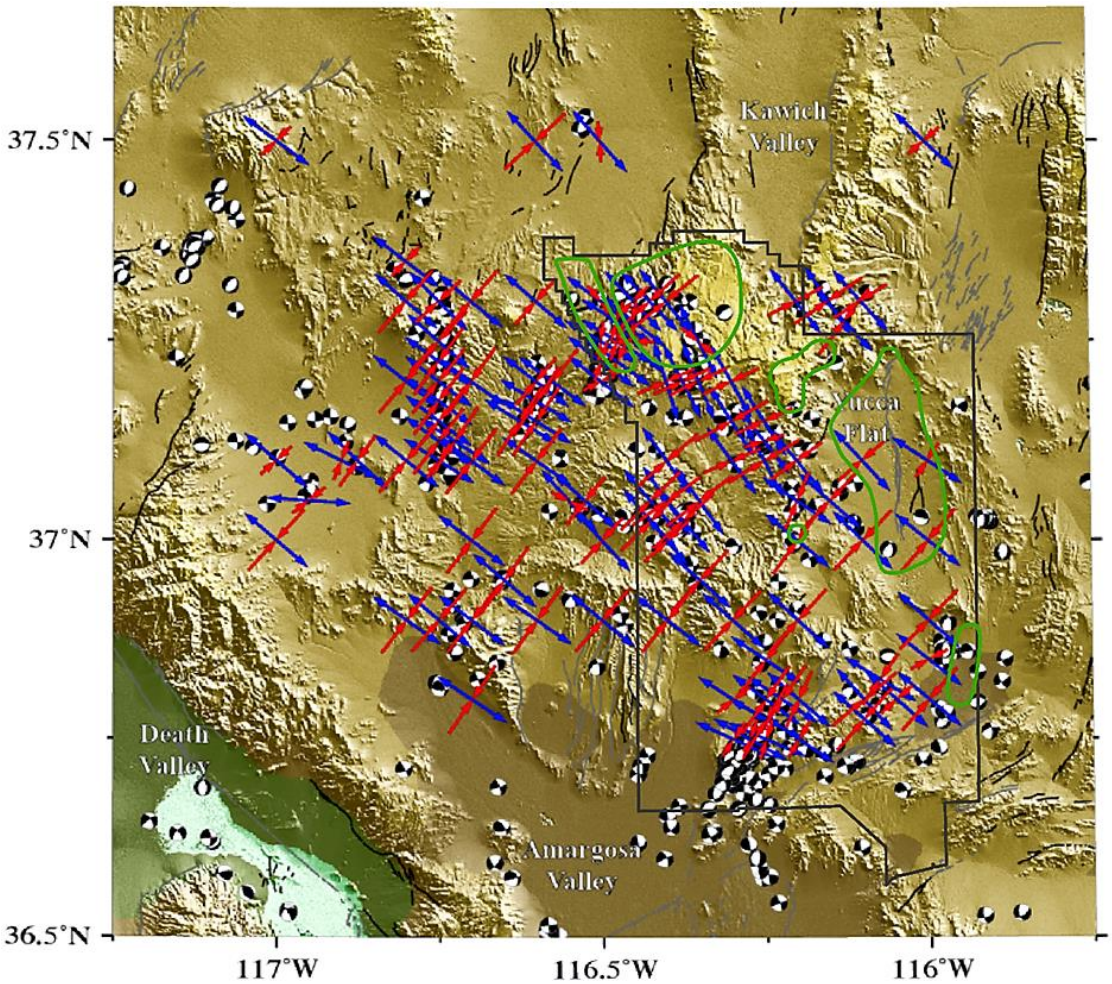

Figure 4. SATSI output T-axis (blue) and P-axis (red) orientations along with NNSS boundary (black line) and individual CAUs (green line). Western and Central Pahute Mesa CAUs are located in the northwest region of the NNSS.

Figure 4 shows the inversion results overlain on the focal mechanism data. Shown are the T-axes (minimum compressive stress axis) and P-axes (maximum compressive stress axis), where the length of the vector is proportional to the plunge angle of the principal stress axis (horizontal plunge, greatest length). The density of stress axes in various locations reflects the grid smoothing strategy that is applied. There is a larger variation in the P-axes orientation relative to the T-axes, whereas the T-axes orientation is generally horizontal, indicative of a transtensional stress regime. This is consistent with current deformation of the Walker Lane (Faulds and Henry, 2008). Numerous events and focal mechanisms just south of the study area are primarily aftershocks of the 1992 M 5.6 Little Skull Mountain earthquake (Smith *et al.*, 2001) and only moderately impacts stress results in the southern portion of the study area. The 1992 Little Skull Mountain earthquake was a normal faulting event on a southeast dipping structure. The structural fabric of the western Great Basin of Nevada and California has historically been recognized as being driven by a transtensional stress field (Faulds and Henry, 2008). Stress results are used as input to dilation and slip tendency analyses.

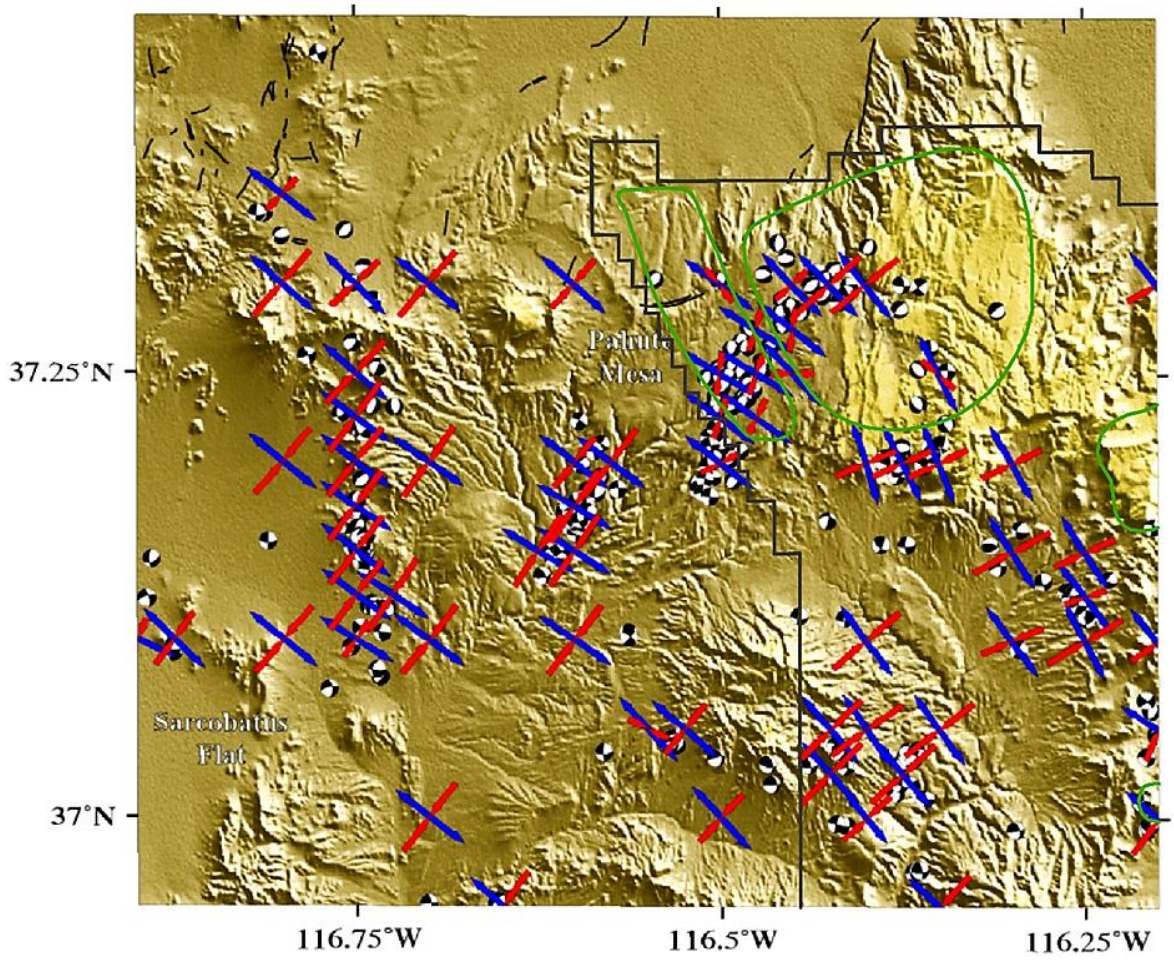

Figure 5. SATSI output T-axis (blue) and P-axis (red) orientations (from Figure 4) along with NNSS boundary (black line) and individual CAUs (green line). Western and Central Pahute Mesa CAUs are located in the northwest region of the NNSS.

Figure 5 is a close-up view of the results in the northern NNSS and Pahute Mesa area from Figure 4. The high density of focal mechanisms in the central area of Figure 5 includes estimated mechanisms from the Benham induced seismicity study (Hamilton *et al.*, 1971), as well as other focal mechanisms developed in the modern era. This area shows the highest variability in the stress field in the study region. Seismicity triggered (induced) by the Benham test are generally consistent with the regional stress field implying some component of tectonic stress release. Additionally, the local stress field appears to be modified by the Timber Mountain Caldera complex, north-northeast of Crater Flat and at the southern edge of Pahute Mesa (geographic reference, Figure 3). Focal mechanisms and SATSI results along the western edge of Pahute Mesa show strike slip focal mechanism solutions and with a well-constrained NW oriented T-axis along its strike. This could be interpreted as the presence of a N-S striking strike slip fault system, or fault zone, just bordering Pahute Mesa.

Approximately N-S striking normal fault systems that overprint Pahute Mesa tuffs, and Silent Canyon caldera structures can be correlated with the character and orientation of similar structures near Yucca Mountain in southwestern NNSS. These structures are therefore constrained to post-caldera Miocene deformation. Induced Behnam earthquake mechanisms are consistent with the orientation and expected sense of motion of these normal faulting structures, which implies a component of tectonic release considering these structures are not oriented in a geometry dissimilar to the prevailing stress field. It also suggests that little deformation has taken place in the NW NNSS since Miocene caldera forming events. This is consistent with the very low slip rates (i.e., on the order of 0.01 mm/yr) of NNSS fault systems (e.g., studies reported in Stuckless and Levich [2007]).

NNSS Stress Field Directions and Magnitudes

A computer code, described in detail in Section 3, is used to process the SASTI solutions by computing the eigenvectors of the SATSI deviatoric stress tensor. These eigenvectors represent the directions of maximum and minimum horizontal stress, denoted as S_{Hmax} and S_{hmin}, respectively. Maximum horizontal stress directions computed by the SATSI solutions range from N27°E to N68°E with an average of N36°E over the entire NNSS, and N29°E to N63°E with an average of N42°E for Pahute Mesa. These S_{Hmax} orientation estimates are in general agreement with average S_{Hmax} orientations estimated for sub-areas within the NNSS, and the NNSS as a whole (Table 1).

Table 1. NNSS compilation of average maximum horizontal stress directions.

Region	S_{Hmax}	**Method**	**Source**
NNSS (comprehensive)	N43°E	breakouts, fault kinematics, focal mechanisms, hydraulic fracturing, overcoring	Carr (1974), Haimsen (1981)
Climax Stock	N42°E	overcoring	Ellis and Magner (1982)
Pahute Mesa	N30°E	breakouts	Springer and Thorpe (1984), Gillson (1987, 1990*), Unpublished Memos
Rainier Mesa	N33°E	hydraulic fracturing, overcoring	Haimson (1981), Smith *et al.* (1981), Warpinski *et al.* (1991)
Yucca Flat	N42°E	breakouts, explosion fractures, focal mechanisms, fault kinetics, hydraulic fracturing	Carr (1974), Haimson (1981), Springer and Thorpe (1981)
Yucca Mountain	N28°E	breakouts, drilling induced hydraulic fractures	Stock *et al.* (1985)

* Gillson (1990) analysis provided by Navarro (2016).

Data from borehole breakouts, also known as borehole elongation or spalling, represent the only other data available to estimate directions of S_{Hmax} at PM. Borehole breakouts result from elongation and subsequent shear failure of the borehole wall along S_{hmin} where compressive stresses are most concentrated (Figure 6). The propensity of breakouts increases with borehole size and horizontal stress anisotropy. Data on borehole breakouts were collected from 34 large-diameter (1.8 to 2.4 m) emplacement holes: U19ac, U19af, U19ai, U19aj, U19an, U19ar, U19ax, U19ba, U19bg, U19t, U20ab, U20ac, U20ad, U20ae, U20ag, U20ah, U20ai, U20aj, U20ak, U20al, U20am, U20an, U20ao, U20ap, U20aq, U20ar, U20as, U20at, U20av, U20aw, U20ax, U20ay, U20az, U20bb, U20bc, U20bd (Table 2, Figures 7 and 8). Note that breakout data exists for smaller diameter boreholes (e.g., ER-EC series) but are excluded from the analysis because of the relatively small diameter as compared to the emplacement boreholes and sporadic occurrence of breakouts.

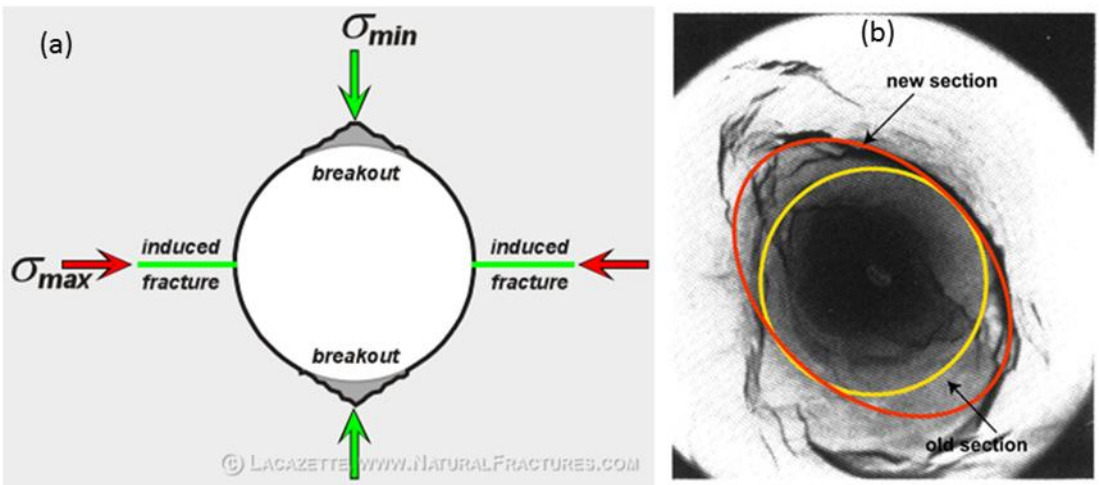

Figure 6. (a) Relationships of borehole breakouts to minimum and maximum horizontal stress (from http://www.naturalfractures.com/3.1.htm) and (b) downhole image of borehole elongation and breakout (red) from circular trend (yellow, from http://legacy.ingv.it/roma/profilo/fondazione/sezioni/romauno/webuf2/activestress/breakout-pozzo.html).

The borehole breakout data, which denotes the direction of S_{hmin} (S_{Hmax} is orthogonal to S_{hmin}), exhibits the most, and often erratic, variability of all the data used to estimate stress directions (Table 2). Inconsistency in average breakout orientations reflect the high degree of variability in the orientation of breakout clusters which sometimes exceed 100°, indicating transitions in S_{hmin} from NW-SE to NE-SW within the same borehole. Similar observations for USW G-1 were made at Yucca Mountain by Stock *et al.* (1985) where two sets of breakouts were observed: one in agreement with regional stress field directions characterized from drilling-induced hydraulic fractures, the other with a dramatically different, anomalous orientation.

Table 2. Average breakout orientation data (N = 0°) from large diameter boreholes.

Borehole	Bit Size (m)	Borehole Depth (m)	Avg Breakout (°)	Source 1	Avg Breakout (°)	Source 2	Avg All Breakouts (°)
U19ac	2.44	701	195.00	Gillson, 1990*, Mov			195.00
U19af	1.62	671	315.00	Gillson, 1990*, Mov			315.00
U19ai	2.44	632	281.00	Springer and Thorpe, 1984	271.00	Gillson, 1990*, Mov	276.00
U19aj	2.44	671	314.00	Springer and Thorpe, 1984	219.00	Gillson, 1990*, Mov	266.50
U19an	3.05	655	343.53	Gillson, 1987, DDS	324.13	Gillson, 1990*, Mov	333.83
U19ax	2.44	671	295.80	Gillson, 1987, DDS	305.40	Gillson, 1990*, Mov	300.60
U19t	2.44	589	315.00	Springer and Thorpe, 1984	268.00	Gillson, 1990*, Mov	291.50
U19ba			293.00	Drellack to Warren			293.00
U19bg			311.00	Springer and Thorpe, 1984	290.00	Prothro to Warren	300.50
U20ab	2.44	714	289.00	Springer and Thorpe, 1984	324.00	Gillson, 1990*, Mov	306.50
U20ac	2.44	677	368.00	Springer and Thorpe, 1984	295.00	Gillson, 1990*, Mov	331.50
U20ad	2.44	716	295.00	Springer and Thorpe, 1984	273.00	Gillson, 1990*, Mov	284.00
U20ae	2.44	716	220.00	Springer and Thorpe, 1984	285.00	Gillson, 1990*, Mov	252.50
U20ag	2.44	671	270.00	Gillson, 1990*, Mov			270.00
U20ah	2.44	701	335.44	Gillson, 1990*, Mov			335.44
U20ai	2.44	657	300.00	Gillson, 1990*, Mov			300.00
U20aj	2.44	564	308.74	Gillson, 1990*, Mov			308.74
U20ak	2.44	640	271.15	Gillson, 1990*, Mov			271.15
U20al	2.44	610	292.67	Gillson, 1990*, Mov			292.67
U20am	2.44	671	325.05	Gillson, 1990*, Mov			325.05
U20an	2.44	618	265.00	Gillson, 1990*, Mov			265.00
U20ao	3.05	655	322.52	Gillson, 1990*, Mov			322.52
U20ap	2.44	651	361.00	Gillson, 1990*, Mov			361.00
U20aq	2.44	579	251.51	Gillson, 1990*, Mov			251.51
U20ar	3.05	561	245.63	Gillson, 1990*, Mov			245.63
U20as	2.44	640	318.48	Gillson, 1987, DDS	251.74	Gillson, 1990*, Mov	285.11
U20at	3.05	579	317.89	Gillson, 1987, DDS	272.89	Gillson, 1990*, Mov	295.39
U20av	2.44	640	320.51	Gillson, 1987, DDS	293.46	Gillson, 1990*, Mov	306.98
U20aw	3.05	640	314.34	Gillson, 1987, DDS	227.14	Gillson, 1990*, Mov	270.74
U20ax	3.05	671	295.80	Gillson, 1987, DDS	281.83	Gillson, 1990*, Mov	288.82
U20ay	2.44	640	282.52	Gillson, 1987, DDS	276.31	Gillson, 1990*, Mov	279.41
U20az	2.44	686	287.60	Gillson, 1987, DDS	281.63	Gillson, 1990*, Mov	284.62
U20bb	3.05	675	289.41	Gillson, 1987, DDS	321.70	Gillson, 1990*, Mov	305.55
U20bc	2.44	610	283.91	Gillson, 1987, DDS	300.00	Gillson, 1990*, Mov	291.96
U20bd	2.44	617	291.15	Gillson, 1987, DDS	303.89	Gillson, 1990*, Mov	297.52

*Gillson (1990) analysis provided by Navarro (2016).

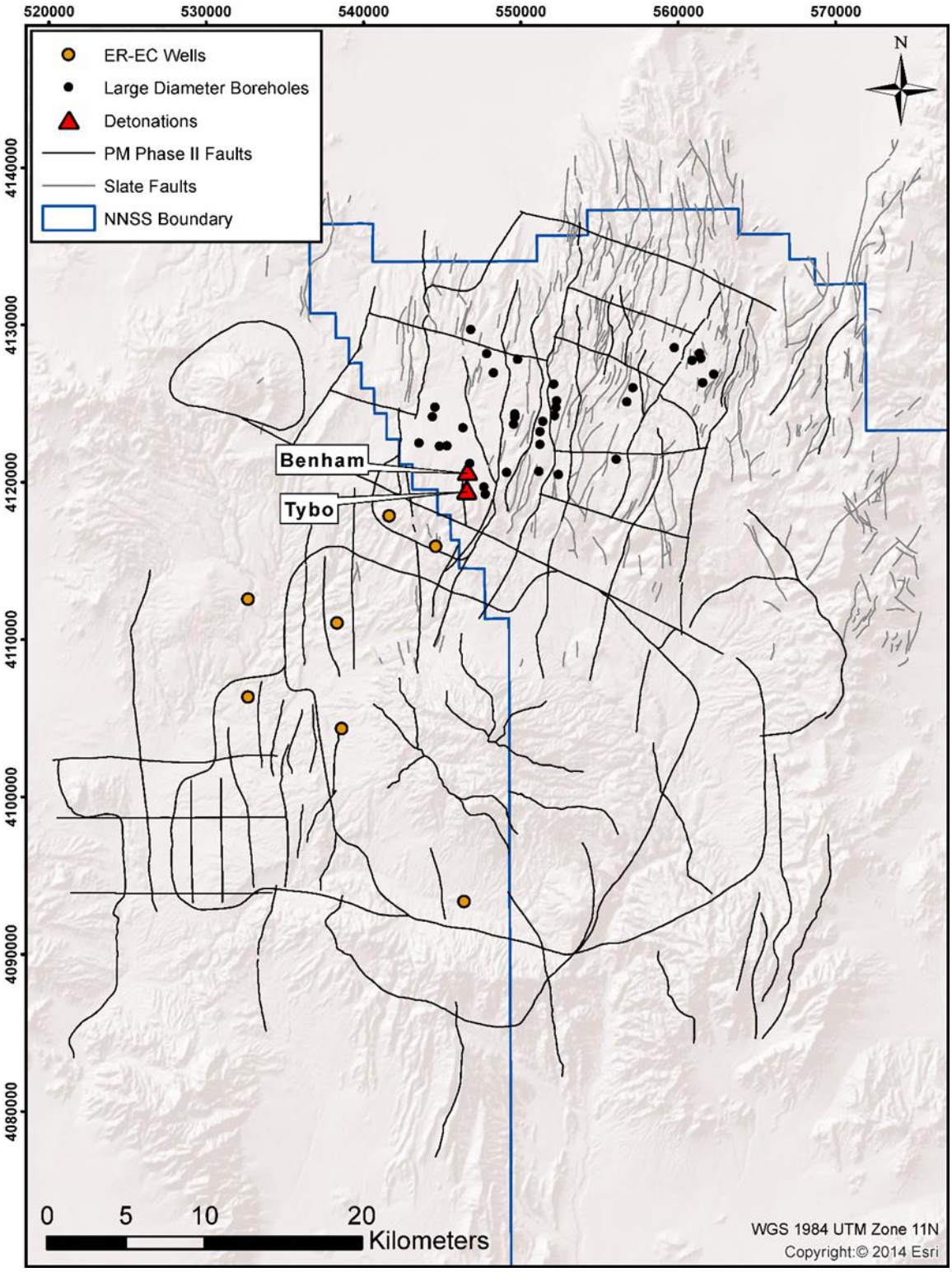

Figure 7. Location of large diameter boreholes and ER-EC wells used in this study. The NNSS boundary, PM Phase II and Slate *et al.* (1999) fault and structural features (refer to following section), and TYBO and BENHAM tests are shown for context.

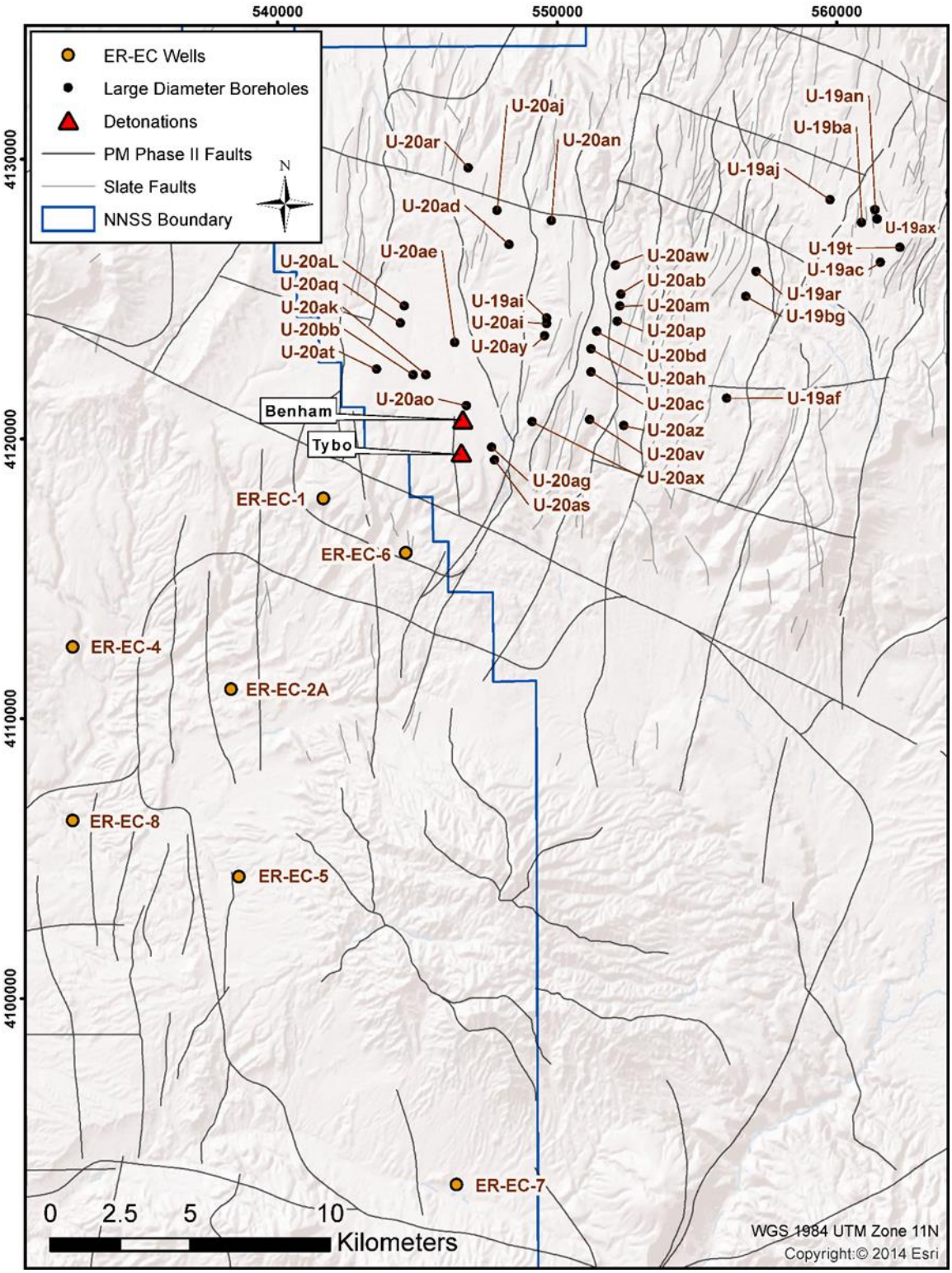

Figure 8. Zoomed in version of Figure 7 with individual labels given to large diameter boreholes and ER-EC wells. The NNSS boundary, PM Phase II and Slate *et al.* (1999) fault and structural features (refer to following section), and TYBO and BENHAM tests are shown for context.

Stress magnitudes on the NNSS have been computed from hydraulic fracturing and/or overcoring for the Climax Granite Stock north of Yucca Flat (Ellis and Magner, 1982), G- and N-tunnels at Rainier Mesa (Ellis and Ege, 1976; Haimson, 1981; Smith *et al.*, 1981), and two boreholes at Yucca Mountain (Stock *et al.* 1985) (Table 3). These measurements were taken at depths ranging from 260 to 1288 m below land surface (bls). Horizontal stresses generally increase with depth, as expected, although some inter-site variability is observed. Overall, horizontal stress anisotropy is higher for the overcoring methods, with the ratio of S_{Hmax} to S_{hmin} (denoted as S_{Hmax}/S_{hmin} in Table 3) ranging from 1.2 to 2.6 for hydraulic fracturing and 3.2 to 4.1 for overcoring. The bias toward higher horizontal stress anisotropy ratios for overcoring methods can be directly observed for G- and N-tunnels where overcoring and hydraulic fracturing were both used to estimate stress magnitudes (Table 3).

Table 3. Stress magnitudes (MPa) for the NNSS listed in order of depth below land surface.

Region	δ_{Hmax}	δ_{hmin}	δ_v	$\delta_{Hmax}/\delta_{min}$	**Depth (m)**	**Method**	**Source**
Climax SFT-C	11.6	2.8	7.1	4.1	260	Overcoring	Ellis and Magner (1982)
Climax Hard Hat	13.9	4.3	9.1	3.2	418	Overcoring	Ellis and Magner (1982)
U12g	7.5	3.0	7.3	2.5	426	Hydraulic Fracturing	Smith *et al.* (1981)
U12g	8.5	2.6	6.8	3.3	426	Overcoring	Ellis and Ege (1976)
U12n	9.0	3.5	7.0	2.6	380	Hydraulic Fracturing	Haimson (1981)
U12n	8.0	2.5	6.0	3.2	380	Overcoring	Haimson (1981)
USW G-2	16.8	11.1	20.8	1.5	1,026	Hydraulic Fracturing	Stock *et al.* (1985)
USW G-2	17.3	12.0	25.5	1.4	1,209	Hydraulic Fracturing	Stock *et al.* (1985)
USW G-1	17.9	14.8	27.2	1.2	1,288	Hydraulic Fracturing	Stock *et al.* (1985)

The Stock *et al.* (1985) hydraulic fracturing derived stress magnitudes, measured at approximately 1 km bls, are considered the most representative stress measurements computed within the NNSS. These data are used in this study to compute dilation and slip tendency for the following reasons:

- Hydraulic fracturing allows for accurate measurement of S_{hmin}, with an error range of ±5 percent reported by Ljunggren *et al.* (2003).
- Stock *et al.* (1985) methodology eliminates the scale dependence of rock tensile strength, which greatly reduces uncertainty in the estimation of S_{Hmax}.
- Hydraulic fracturing measures S_{hmin} over a larger borehole interval than overcoring methods, which are essentially point measurements subject to sharp changes in rock composition and presence of fractures and fault breccia.

- Stock *et al.* (1985) stress magnitudes were measured at an approximate depth of 1 km, unlike the other estimates from more shallow depths, which can be influenced by other factors, such as local topographic influences on the stress field.

In general, focal mechanisms and the presence of both normal and strike-slip faults infers that the NNSS experiences a north-south transition from normal to strike-slip faulting, giving rise to an approximate stress condition: $s_v \approx s_{H\max} > s_{h\min}$. Magnitudes from Stock *et al.* (1985) yields the condition: $s_v > s_{H\max} > s_{h\min}$, which is representative of a normal fault regime according to Anderson's (1953) classification scheme. A normal fault regime is more consistent with Pahute Mesa focal mechanisms, which show a transtensional regime with oblique slip along normal faults (Figures 3 through 5), than the other stress estimates listed in Table 3, which imply strike-slip regimes ($s_{H\max} > s_v > s_{h\min}$). Note that focal mechanisms and presence of shear zones in the Climax area (Yow, 1984) may support a strike-slip regime (Figures 4 and 5, Climax region not labeled). However, Rainier Mesa specific data from focal mechanisms (Figures 4 and 5) and faults and fractures (Reeves *et al.*, 2014) strongly support a normal fault regime.

Detailed cross-sectional geometry of borehole breakouts can be used to estimate stress field magnitudes at Pahute Mesa (e.g., Zoback *et al.* [1985]). However, estimates of stress magnitudes from borehole breakouts have a much higher degree of uncertainty than hydraulic fracturing and overcoring since breakout geometry can vary according to factors unrelated to the stress field. For example, borehole breakouts provided in Gillson (1987) exhibit a wide range cross-sectional geometries that cannot solely be attributed to the stress field. Analysis of breakouts for computation of stress magnitudes is beyond the scope of this project and would have necessitated reprocessing boreholes with televiewer logs and running additional computations. It is unlikely that stress magnitudes obtained from borehole breakouts would reduce uncertainty with respect to horizontal stress anisotropy for this project.

HYDRAULIC FUNCTION OF FAULT AND FRACTURES

Faults and fractures may function hydraulically as conduits and/or barriers to fluid flow. The permeability of faults and joints in low-permeability rock is proportional to the square of fracture aperture, defined as the physical distance normal to fracture walls (Snow, 1965). This nonlinear trend describes how small changes in aperture lead to significant changes in permeability. Aperture may be enhanced or dilated by either minimizing the amount of stress normal to the fracture or through shear displacement (National Research Council, 1996; Jaeger *et al.*, 2007; Zoback, 2010). Both normal and shear stresses acting on a fracture can be resolved on a fracture plane if the principal directions and magnitudes of the stress field are known. The hydraulic function of fractures can then be inferred from these stresses using dilation (Morris *et al.*, 1996) and slip tendency (Ferrill *et al.*, 1999) metrics.

Fault Dilation and Slip Tendency

Dilation tendency T_d of a fault is defined by (Ferrill *et al.*, 1999):

$$T_d = \frac{\sigma_1 - \sigma_N}{\sigma_1 - \sigma_3} \tag{1}$$

where T_d is a dimensionless ratio describing the amount of normal stress σ_N acting on the fault plane normalized by the differential stress, where $\sigma_1 > \sigma_2 > \sigma_3$ are the principal stresses listed in order of magnitude and $0 \le T_d \le 1$. As the stress component normal to the fault plane decreases, the dilation tendency of the fault increases. Note that the concept of dilation tendency is intended to serve as a qualitative metric on the propensity of a fault to be open within a regional stress field and conduct fluid (Ferrill *et al.*, 1999; Ferrill and Morris, 2003).

Slip tendency T_s is the ratio of shear stress σ_T relative to the normal stress on a fault plane, σ_N (Morris *et al.*, 1996):

$$T_s = \frac{\sigma_S}{\sigma_N} \ge \mu_s \ . \tag{2}$$

Fault reactivation and slip typically occurs when $T_s > 0.6$ as the coefficient of static friction μ_s is exceeded (Byerlee, 1978). Therefore, fractures and faults in the range of $0.6 \le T_s \le 1$ are considered "critically stressed" relative to the stress field and open to fluid flow. Hydraulic testing of critically versus noncritically stressed fractures detected in boreholes has shown good correlation between flowing fractures and critically stressed fractures at some locations (e.g., Barton *et al.* [1995] and Zoback *et al.* [2010]).

Computation of fault dilation and slip tendency involves the resolution of both normal and shear stresses acting on a fault plane with a stress field. The Cauchy stress tensor, σ_{ij}, is a symmetric, second rank tensor of the form:

$$\sigma_{ij} = \begin{bmatrix} \sigma_{11} & \sigma_{12} & \sigma_{13} \\ \sigma_{21} & \sigma_{22} & \sigma_{23} \\ \sigma_{31} & \sigma_{32} & \sigma_{33} \end{bmatrix} \tag{3}$$

which describes the full stress field relative to an arbitrary Cartesian coordinate system (Figure 9). Normal stresses are represented by the diagonal (i = j) components of the Cauchy stress tensor, whereas shear stresses are represented by off-diagonal ($i \neq j$) components. Principal directions and magnitudes of the stress field can be determined by taking the eigenvectors and eigenvalues of σ_{ij}, respectively.

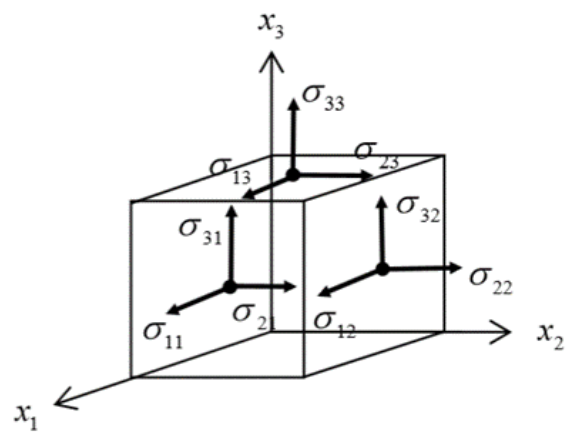

Figure 9. Representation of the Cauchy stress tensor on an arbitrary Cartesian coordinate system. From Kelley (2015).

If the coordinate system is aligned with the three principal stress directions of the stress field, the Cauchy stress tensor can be described by:

$$\sigma_{ij} = \begin{bmatrix} \sigma_{11} & 0 & 0 \\ 0 & \sigma_{22} & 0 \\ 0 & 0 & \sigma_{33} \end{bmatrix} = \begin{bmatrix} \sigma_1 & 0 & 0 \\ 0 & \sigma_2 & 0 \\ 0 & 0 & \sigma_3 \end{bmatrix} \tag{4}$$

where the stress field is represented exclusively in terms of three normal stress (also denoted by σ_1, σ_2, and σ_3) acting in the principal stress directions. The principal stress axes are orthogonal to one another, and in a geologic setting, two principal stresses are located in the horizontal plane, and the third is along the vertical plane. This allows the stress field to be represented in terms as minimum horizontal S_{hmin}, maximum horizontal S_{Hmax}, and vertical S_v stress components. This nomenclature can be helpful in describing regional stress fields because stress components are usually ranked such that $\sigma_{11} > \sigma_{22} > \sigma_{33}$ (and by extension: $\sigma_1 > \sigma_2 > \sigma_3$), and relationships between S_{hmin}, S_{Hmax}, and S_v can be used to easily classify between normal, reverse and strike-slip faulting regimes (Anderson, 1953). Note that in-situ normal stresses at depths greater than a few tens of meters below land surface are always compressive (Zoback, 2010), and hence, the sign convention applied to stress values in this report are compression positive unless otherwise noted.

The SATSI stress field inversions provide best-fit deviatoric stress ratios constrained by earthquake focal mechanism slip vectors and the relationship: $\sigma_{33} = -(\sigma_{11} + \sigma_{22})$ (Michael, 1984). Deviatoric stress, $d\sigma_{ij}$, is defined as:

$$d\sigma_{ij} = \sigma_{ij} - \delta_{ij}\sigma_{\mu} = \begin{bmatrix} \sigma_{11} - \sigma_{\mu} & \sigma_{12} & \sigma_{13} \\ \sigma_{21} & \sigma_{22} - \sigma_{\mu} & \sigma_{23} \\ \sigma_{31} & \sigma_{32} & \sigma_{33} - \sigma_{\mu} \end{bmatrix} \tag{5}$$

where δ_{ij} is the Kronecker delta function and isotopic stress is defined as: $\sigma_{\mu} = \frac{\sigma_{11} + \sigma_{22} + \sigma_{33}}{3}$.

The SATSI algorithm neglects isotropic stress by simply setting σ_{μ} to zero. This methodology allows for the determination of principal stress directions from deviatoric stress ratios, although the magnitudes of the ratios are not physically meaningful. Directions of minimum and maximum horizontal stress, S_{hmin} and S_{Hmax}, approximately correspond to the T-axis and P-axes, respectively, in Figures 4 and 5. Note that horizontal stress directions are spatially variable within the NNSS, whereas the remaining component of stress, $S_{v,}$ is vertical and is a function of overburden weight above a measurement point.

The abundance of normal faults, the distribution of focal mechanisms over the NNSS (Figures 3 through 5), and stress field magnitudes measured by Stock *et al.* (1985) at Yucca Mountain where S_{hmin} = 11 MPa, S_{Hmax} = 17 MPa, and S_v = 21 MPa (Table 3), indicate that most of the NNSS, including Pahute Mesa, is in a transtensional stress regime with predominately oblique slip occurring along normal faults.

Normal and shear components of stress acting on a plane can be determined from Cauchy's Law (Kelly, 2015):

$$\mathbf{t} = \boldsymbol{\sigma}\mathbf{n}, \quad t_i = \sigma_{ij} n_j \tag{6}$$

which states that a traction vector, **t**, acting on a plane is the product of the Cauchy stress tensor and unit vector **n** normal to the plane (Figure 10). It is inherent in Cauchy's Law that: $\mathbf{t} = \lim_{\Delta s \to 0} \frac{\Delta F}{\Delta S}$ where F is force and S is surface on which the force F acts.

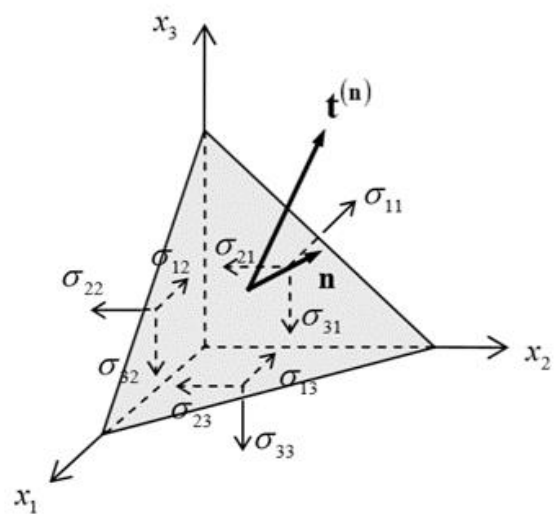

Figure 10. Free body diagram of a tetrahedral portion of a material showing traction vector in relation to the unit normal vector acting on the plane and the stress field. From Kelly (2015).

Once the traction vector is defined, the stress acting normal to a surface σ_N and shear stress acting on a surface σ_S are given by (Kelly, 2015):

$$\sigma_N = \mathbf{n} \cdot \mathbf{t} \tag{7}$$

and

$$\sigma_S = \sqrt{|\mathbf{t}|^2 - \sigma_N^2} \ . \tag{8}$$

RStress, a Fortran 95 code developed for this project, incorporates the traction vector method described in Equations (7) and (8) to compute dilation and shear tendency for a fault plane of any orientation given SATSI defined stress directions and Stock *et al.* (1985) stress magnitudes. The Stock *et al.* (1985) stress magnitudes are held constant within the study domain. The SATSI stress inversion solutions to the deviatoric stress tensor $d\sigma_{ij}$ (Equation [5]) are first read by the code. Principal stress directions are then determined for each stress field inversion solution (148 total over the entire NNSS, 91 within PM) using the Jacobi method to compute the eigenvectors of the deviatoric stress tensor (Press *et al.*, 1996). The resultant eigenvectors are automatically checked in the code to ensure that the necessary conditions of unit magnitude and S_{hmin} and S_{Hmax} orthogonality are satisfied. The code also checks to ensure that the SATSI stress ratio condition: $\sigma_{33} = -(\sigma_{11} + \sigma_{22})$ is achieved. Accuracy of eigenvectors and their directions computed from the Jacobi subroutine was validated using Mathematica® (Appendix C).

A total of 15,625 Pahute Mesa fault segments, denoted by easting and northing pairs UTM WGS84, are then read by the code. These segments were digitized from a GIS shapefile, comprised of 79 PM Phase II structural features (i.e., faults, caldera margins and associated structural zones) compiled by NSTec (2014) and 314 Slate *et al.* (1999) faults, into 100 m long intervals (Figures 11 and 12). Note that the NSTec (2014) PM faults were given precedence over the Slate *et al.* (1999) faults, and thus, only nonduplicate faults and fault segments from Slate *et al.* (1999) were incorporated into the combined fault map shown in Figure 12. Approximately 60 percent of the fault segments were digitized from the PM Phase II map, with the other 40 percent digitized from Slate *et al.* (1999). On the basis of analyzing the total number of fault segments for each source, the PM Phase II faults are approximately 6 times longer than the smaller-scale Slate faults. The 100 m segment length was arbitrarily selected to adequately capture both the azimuthal curvature of the faults and for sufficient resolution of the spatially variable directions of S_{hmin} and S_{Hmax}. Fault dip was undifferentiated for all of the faults and was set to a constant value of 80° consistent with NSTec (2014). Therefore, a 2-D representation of the faults is adequate for computation of dilation and slip tendency.

RStress computes dilation and shear tendency according to both: (1) spatially variable SATSI stress inversion (Figure 13), and (2) an average S_{Hmax} direction within PM. The inclusion of spatially variable stress inversion solutions was one of the primary motivators to develop the RStress code, as SATSI stress inversion solutions suggest that S_{Hmax} ranges from N27°E to N68°E with an average of N36°E over the entire NNSS, and N29°E to N63°E with an average of N42°E for PM. A radial, nearest-neighbor search algorithm is employed to identify the nearest SATSI stress field solution(s). Orientations of S_{Hmax} are averaged for the

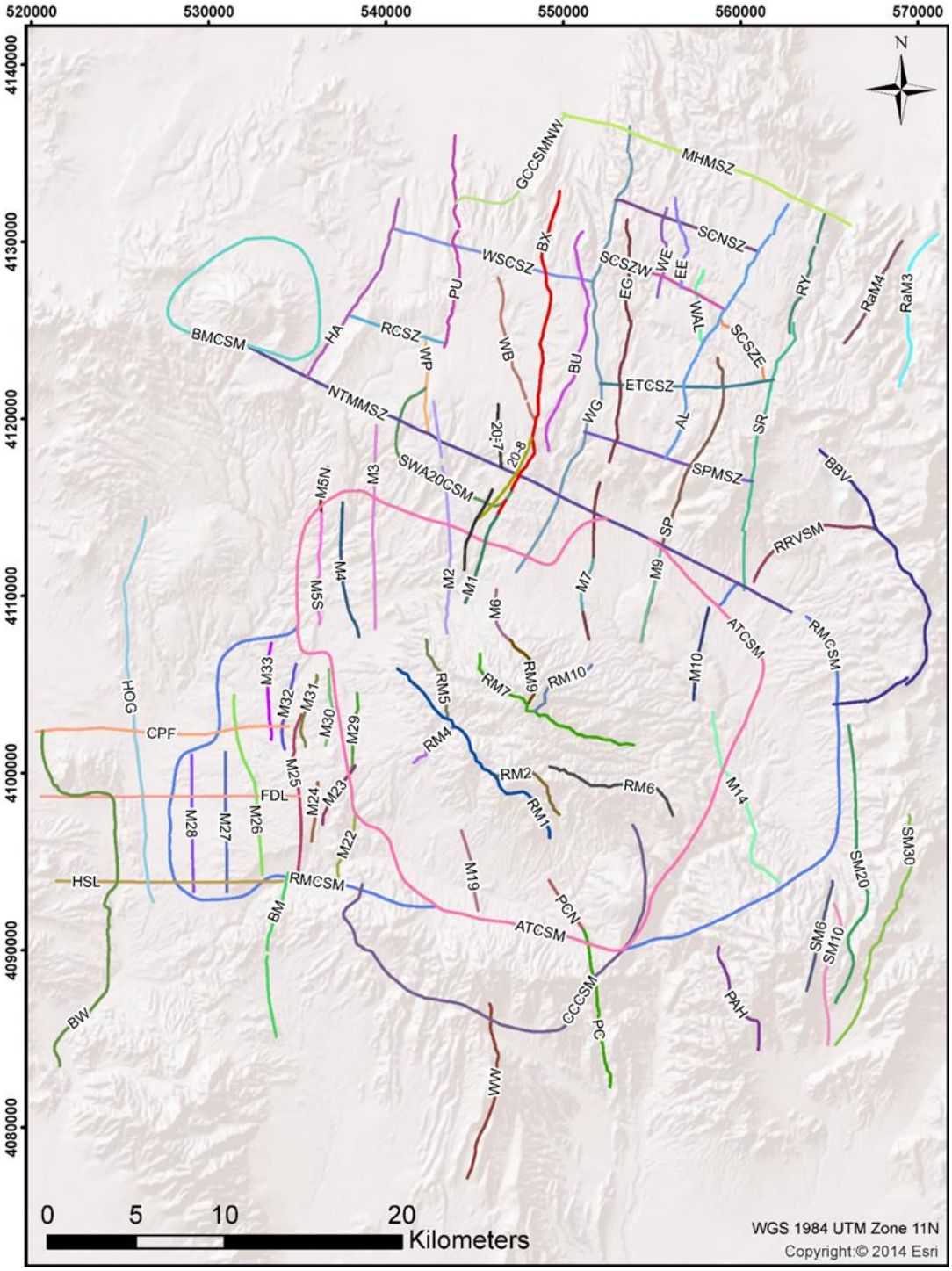

Figure 11. Pahute Mesa Phase II structure and fault map.

Figure 12. Final fault map combining NSTec (2014) PM Phase II faults in Figure 8 with Slate *et al.* (1999) faults.

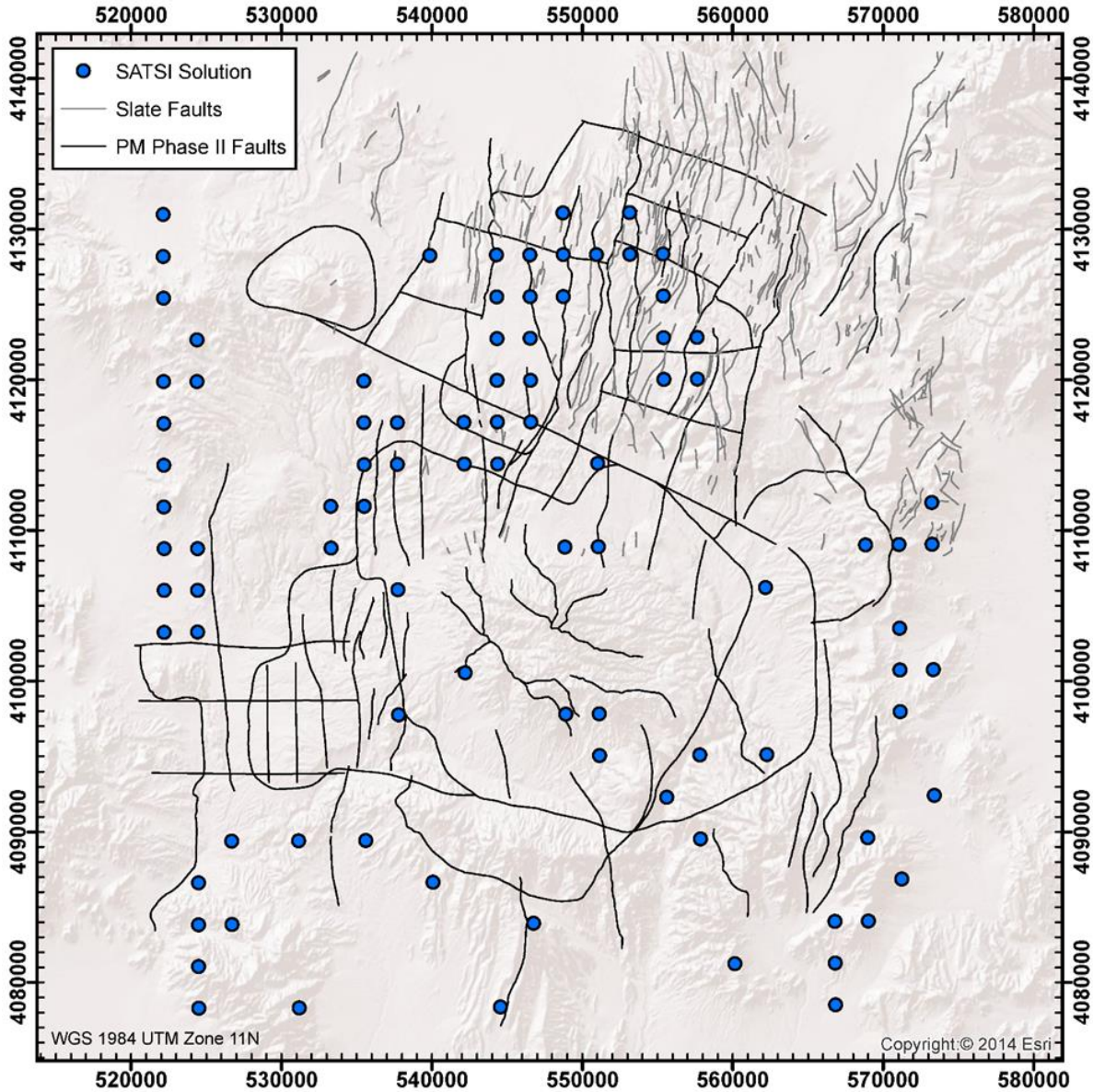

Figure 13. Spatial distribution of SATSI stress field inversion solutions to focal mechanisms within PM (n = 91). Approximate area is 3,560 km^2.

atypical case of two stress inversion solutions located approximately equidistant from the fault segment. Fault segment orientation is adjusted to account for an S_{Hmax} rotation of the in-situ stress field from a Cartesian coordinate system defined by cardinal directions.

Normal and shear stresses acting on each fault segment are first computed, followed by the computation of dilation and slip tendency. Values of dilation and slip tendency are output to a ASCII file containing each 100 m fault segment. Arithmetic averages for each of the 394 faults and structural features are also computed and output by the code. Note that either a geometric or harmonic averaging scheme could have been used to assign average values of dilation and slip tendency. However, dilation and slip tendency values vary be less

than a single order of magnitude for the fault segments at Pahute Mesa and final differences in dilation tendency between arithmetic and harmonic means are small (generally two to three percent) and do not significantly change study results. Code results were verified against known normal and shear stresses computed for a total of seven planar orientations within a synthetic stress field comprised of stress magnitudes 15 MPa, 12 MPa, and 5 MPa for normal, reverse, and strike-slip faulting regimes (Appendix C). This verification also occurred for the stress field defined by Stock *et al.* (1985) consisting of 17 MPa, 11 MPa and 21 MPa (Appendix C). Values and spatial trends of dilation and slip tendency assigned to faults in the vicinity of Yucca Mountain in Ferrill *et al.* (1999), which used the Stock *et al.* (1985) stress field, were used for code verification (Appendix C). Stereonet plots of dilation and slip tendency of any possible fault plane orientation and mapping of RStress segments with dilation and slip tendency values against the combined fault map in Figure 12 served as final verifications to the code in Appendix C.

Dilation and Slip Tendency

Data derived values for horizontal stress anisotropy, denoted by S_{Hmax}/S_{hmin}, range from 1.5 to approximately 4.0 (Table 3). Horizontal stress anisotropy is assigned in RStress by holding S_{Hmax} equal to 17 MPa (consistent with Stock *et al.* [1985]) and modifying S_{hmin} values to achieve the desired S_{Hmax}/S_{hmin} ratio. The degree of horizontal stress anisotropy greatly influences slip tendency, and moderately influences dilation tendency. Uncertainty in horizontal stress ratio is addressed by allowing S_{Hmax}/S_{hmin} to vary from 1.5 to 4.0, with intense study given to S_{Hmax}/S_{hmin} ratios of 1.5, 2.5, and 3.2, which represent low, moderate, and high horizontal stress anisotropy cases, respectively. These ratios are defined from stress magnitudes measured by hydraulic fracturing at Yucca Mountain, hydraulic fracturing at Rainier Mesa, and overcoring at Rainier Mesa and Climax (Table 3).

Trends in Dilated and Critically Stressed Faults

Dilation and slip tendency, as described in Equations (1) and (2), respectively, are continuous values that exist for any planar orientation within a given stress field. Stereonet plots illustrate how planar orientations govern dilation and slip tendency within the stress field defined by average horizontal stress directions computed from SATSI solutions, and Stock *et al.* (1985) stress magnitudes.

Fault dilation tendency serves as a metric for aperture enhancement attributed to the minimization of stress normal to a fault plane. The base case stereonet plot shows that dilation tendency is highly sensitive to fault strike and dip, with maximum dilation tendency values occurring for steeply dipping, NE-SW trending faults (Figure 14a). This implies high dilation tendency values for NE-SW faults in Figure 12 as fault dips are undifferentiated in the NSTec (2014) and Slate (1999) fault maps, and are universally set to dips of 80° consistent with the recommendation of NSTec (2014). A S_{Hmax}/S_{hmin} equal to 4.0 is used to better understand the effects of horizontal anisotropy on dilation tendency. Although this degree of horizontal stress anisotropy is considered unrealistically high at PM, it proves valuable in illustrating that increases in horizontal anisotropy decrease the range of orientations that produce the highest dilation tendency values where $T_d \geq 0.80$ (Figure 14b).

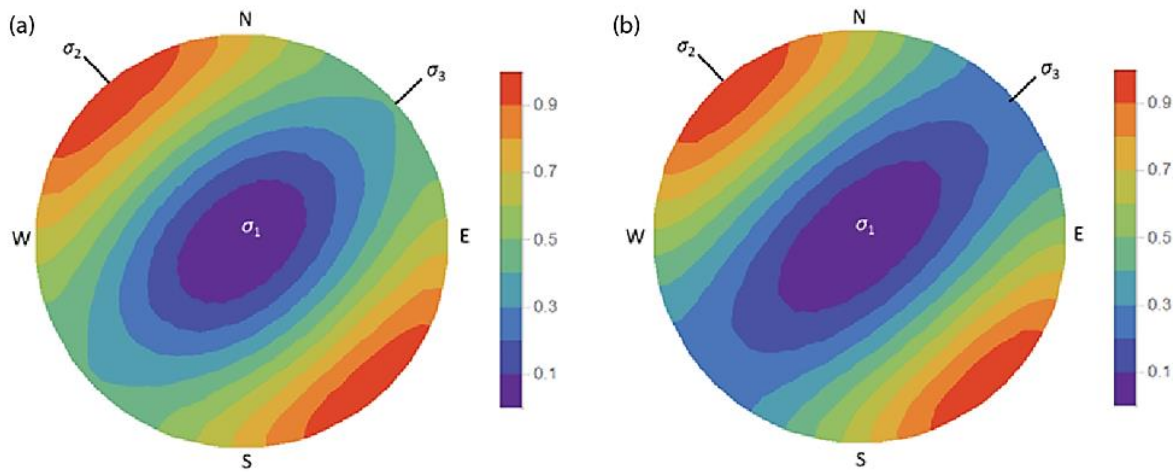

Figure 14. Southern-hemisphere, equal-area stereonet plot of poles to planes of fault dilation tendency given average horizontal stress directions computed from SATSI solutions with locations shown in Figure 9 with (a) S_{Hmax}/S_{hmin} = 1.5 and (b) S_{Hmax}/S_{hmin} = 4.0. Note that taking the pole of a plane results in 3π/2 (270°) clockwise rotation about the strike and that dips increase from 0° in the center to 90° along the outside edge.

Fault slip tendency serves as a metric for aperture enhancement attributed to shear stress. Similar to dilation tendency, the base case stereonet plot illustrates that slip tendency is highly sensitive to fault strike and dip. A maximum slip tendency of 0.33 is possible within the Stock *et al.* (1985) stress field for NE-SW trending faults with dips in a range of approximately 45 to 55° (Figure 15a). Again, recall that dips for all faults are set to 80° indicating that maximum slip tendency values within the base case stress field will be considerably less than the 0.33 maximum, and far below the Byerlee (1978) friction criterion of 0.60 required for slip. Therefore, none of the faults or fractures within PM will be critically stressed within the base case stress field. Application of a horizontal stress anisotropy ratio of 4.0 dramatically increases slip tendency values (maximum of 0.78) and the orientations of faults that exceed 0.60 (Figure 15b). Most importantly, high horizontal stress anisotropy leads to a condition where even steeply dipping faults may be critically stressed. Indeed, the influence of horizontal stress anisotropy exerts a much greater influence on slip tendency than dilation tendency.

The stereonet plots provide a good understanding of how fault orientation influences values of dilation and slip tendency, but are inadequate in conveying information on the total number of the 15,625 fault segments that may be enhanced for fluid flow through either dilation or slip mechanisms. RStress computed values of dilation and slip tendency are presented in Tables 4 and 5 to systematically study the influence of horizontal anisotropy ratios on these mechanisms, given constant stress directions and spatially variable SATSI stress directions. Fault segments with $T_d \geq 0.80$ will be considered dilated because of the reduction of stress normal to fault planes, and critically stressed when $Ts \geq 0.60$ because of the potential for slip.

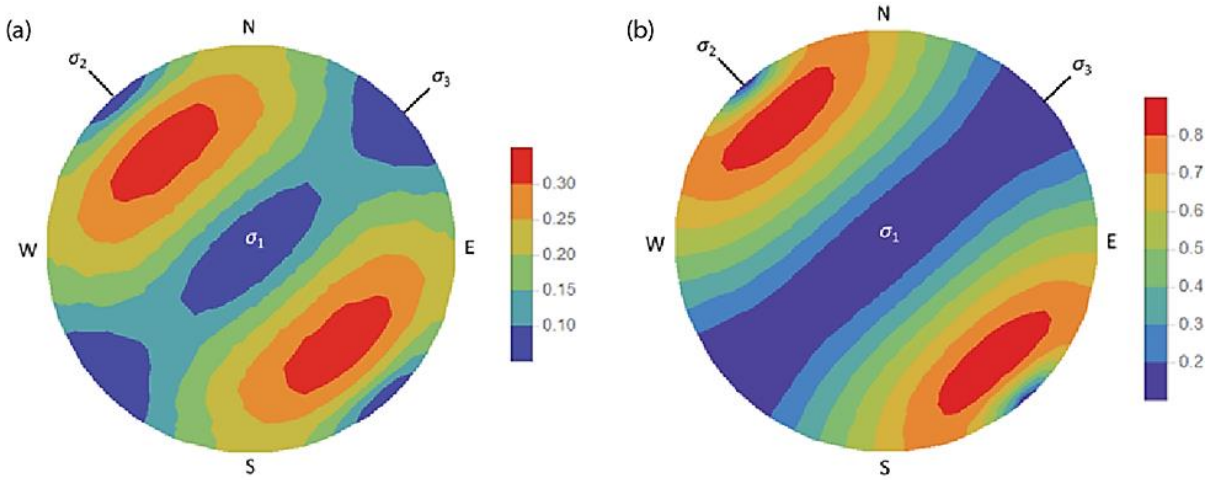

Figure 15. Southern-hemisphere, equal-area stereonet plot of poles to planes of fault slip tendency given average horizontal stress directions computed from SATSI solutions with locations shown in Figure 9 with (a) S_{Hmax}/S_{hmin} = 1.5 and (b) S_{Hmax}/S_{hmin} = 4.0. Note that taking the pole of a plane results in 3π/2 (270°) clockwise rotation about the strike and that dips increase from 0° in the center to 90° along the outside edge.

The number of dilated and critically stressed fault segments are consistently higher for the constant stress field (Table 4) then the spatially variable stress field by approximately eight percent for dilated segments, and between two and eight percent for critically stressed segments. This difference is suggests that the incorporation of a spatially variable stress field in RStress provides a more nuanced distribution of dilated and critically stressed fault segments for PM that is thought to better capture the complex distribution of fault orientations and stress perturbations attributed to calderas and associated structural zones.

Table 4. Dilation and slip tendencies for constant stress field.

S_{Hmax}/S_{hmin}	Dilation Tendency				Slip Tendency			
	min DT	**max DT**	**DT ≥ 0.80**	**% DT ≥ 0.80**	**min ST**	**max ST**	**ST ≥ 0.60**	**% ST ≥ 0.60**
1.5	0.39	0.97	6022	39	0.04	0.23	0	0
2.5	0.27	0.97	5279	34	0.04	0.49	0	0
3.0	0.25	0.97	5163	33	0.04	0.60	1517	10
3.2	0.25	0.97	5141	33	0.04	0.64	4562	29
4.0	0.23	0.97	5061	32	0.04	0.78	9598	61

Table 5. Dilation and slip tendencies for spatially variable stress field.

S_{Hmax}/S_{hmin}	Dilation Tendency				Slip Tendency			
	min DT	**max DT**	**DT ≥ 0.80**	**% DT ≥ 0.80**	**min ST**	**max ST**	**ST ≥ 0.60**	**% ST ≥ 0.60**
1.5	0.39	0.97	4750	30	0.04	0.23	0	0
2.5	0.31	0.97	4056	26	0.04	0.37	0	0
3.0	0.25	0.97	3987	26	0.04	0.60	1271	8
3.2	0.25	0.97	3968	25	0.04	0.64	4189	27
4.0	0.23	0.97	3919	25	0.04	0.78	8313	53

An estimated 32 percent to 40 percent of fault segments at PM within the base case stress field are enhanced for flow due to dilation within the stress field. From a discrete fracture network (DFN) perspective, this equates to a relatively high density of enhanced fault conduits that could preferentially promote flow across Western and Central PM CAUs through connection to smaller faults and fractures. Note that critically stressed fault segments are nonexistent under the base case stress field.

The presence of critically stressed faults does not occur until values of S_{Hmax}/S_{hmin} approach 3.0, and is not significant (i.e., > 20 percent of total fault segments) until S_{Hmax}/S_{hmin} ≥ 3.2. At these higher horizontal stress anisotropy ratios, the total number of fault segments either dilated or critically stressed may exceed 80 or 90 percent. These high horizontal stress anisotropy ratios are unlikely for a few reasons: (1) high S_{Hmax}/S_{hmin} ratios are only reported for overcoring methods at shallow depths, and appear to be biased high when compared to hydraulic fracturing derived measurements at the same sites (Table 3), (2) higher horizontal stress anisotropy ratios where S_{Hmax} □ S_{hmin} are more representative of a strike-slip system which is inconsistent with the PM focal mechanisms and predominance of normal faults, and (3) high percentages of critically stressed faults are inconsistent with USGS Quaternary fault studies.

Fault studies by the USGS indicate that only four faults in the vicinity of the NNSS have experienced displacement over the last 15,000 years (historic to early Pleistocene): Boundary fault, Belted Range fault, Rock Valley fault zone, and Yucca Mountain faults (Anderson, 1998a-d). There are only about a dozen faults or fault zones with Quaternary displacement on the NNSS, including undifferentiated faults on Pahute Mesa described by Anderson (1998e) as: "diversely oriented, variably facing, discontinuous, and mostly weakly expressed as lineaments or scarps…most show no clear association with Tertiary structures, and, together with their highly variable orientation, the lack of association may suggest a nontectonic origin. Nothing is known of their slip rate or occurrence."

Slip rates on all Quaternary structures on the NNSS are categorized as <0.2 mm/yr, which appears to be biased toward higher slip rates, as the Rock Valley fault zones and Yucca Mountain faults have estimated slip rates of 0.002 to 0.05 mm/yr and 0.001 to 0.03 mm/yr, respectively (Anderson, 1998c,d). The slip rates of 1 to 5 mm/yr for the nearby Death Valley fault zone (Machette and Klinger, 2002) and >5 mm/yr for the Fish Lake Valley fault zone (Reheis, 1994) are on the order of 100 to 1,000 times higher than slip rates

for the Yucca faults on the NNSS. These data suggest that the NNSS is undergoing significantly less strain than the surrounding area, particularly to the west, and supports lower horizontal stress anisotropy ratios through the inference of a low number of faults critically stressed for slip.

Spatial Trends in Dilation Tendency

Dilation tendency computed from all 15,625 digitized segments of the Phase II Pahute Mesa faults (Figure 12) are shown for the average stress field computed from the average (Figure 16) and spatially variable (Figure 17) SATSI stress field solutions. Faults with the highest dilation tendency trend NE-SW for both stress field solutions (max = 0.97), and are lowest for NW-SE structures (min = 0.39). Note that with fixed 80° dips for all of the geologic structures, contrast in dilation tendency in Figures 16 and 17 is solely attributed to fault strike. The steep dip of the faults also accounts for the relatively high dilation tendency minimum of 0.39.

In-depth analyses to quantify differences in dilation tendency values between average and spatially variable SATSI stress field inversion solutions are found in Section 3.2.4. Figure 18 spatially illustrates these differences expressed as percent difference in dilation tendency for these two stress conditions. Overall, differences are greatest for the north-central to north-east region of the figure, corresponding to Western and Central Pahute Mesa CAUs, with maximum values on the order of 40 percent. Note that Western and Central Pahute Mesa CAUs contain both the highest density of faults and SATSI stress field solutions (Figure 13).

Minimum, maximum and number of high dilation tendency values decrease with increasing horizontal stress anisotropy ratio (Tables 4 and 5, Figures 19 through 23). Most observable is the shift toward the 0.60 to 0.80 dilation tendency range in many fault structures in the region of Western and Central Pahute Mesa, particularly for the spatially variable stress cases (Figures 19, 21, and 23). The other impact of increasing horizontal stress anisotropy is that dilation tendency values for structures approximately orthogonal to S_{Hmax} tend to further decrease indicating that these structures may serve as barriers to fluid flow because of concentrated normal stress. The spatial distribution of differences in dilation tendency between constant and spatially variable stress fields for the intermediate and high horizontal stress anisotropy cases are similar to the base case and are not shown.

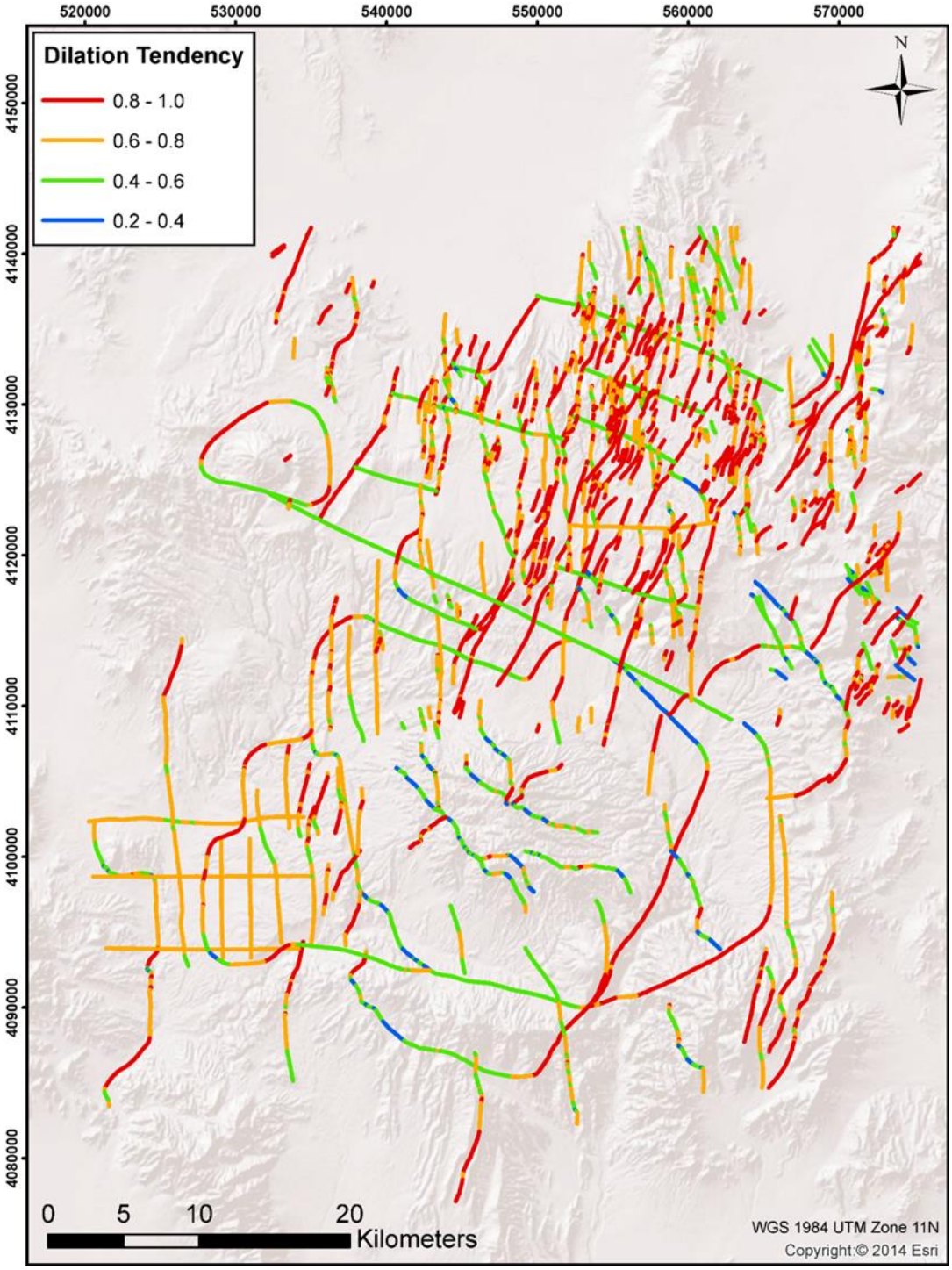

Figure 16. Fault dilation tendency given average horizontal stress directions computed from SATSI solutions for low horizontal stress anisotropy: $S_{Hmax}/S_{hmin} = 1.5$.

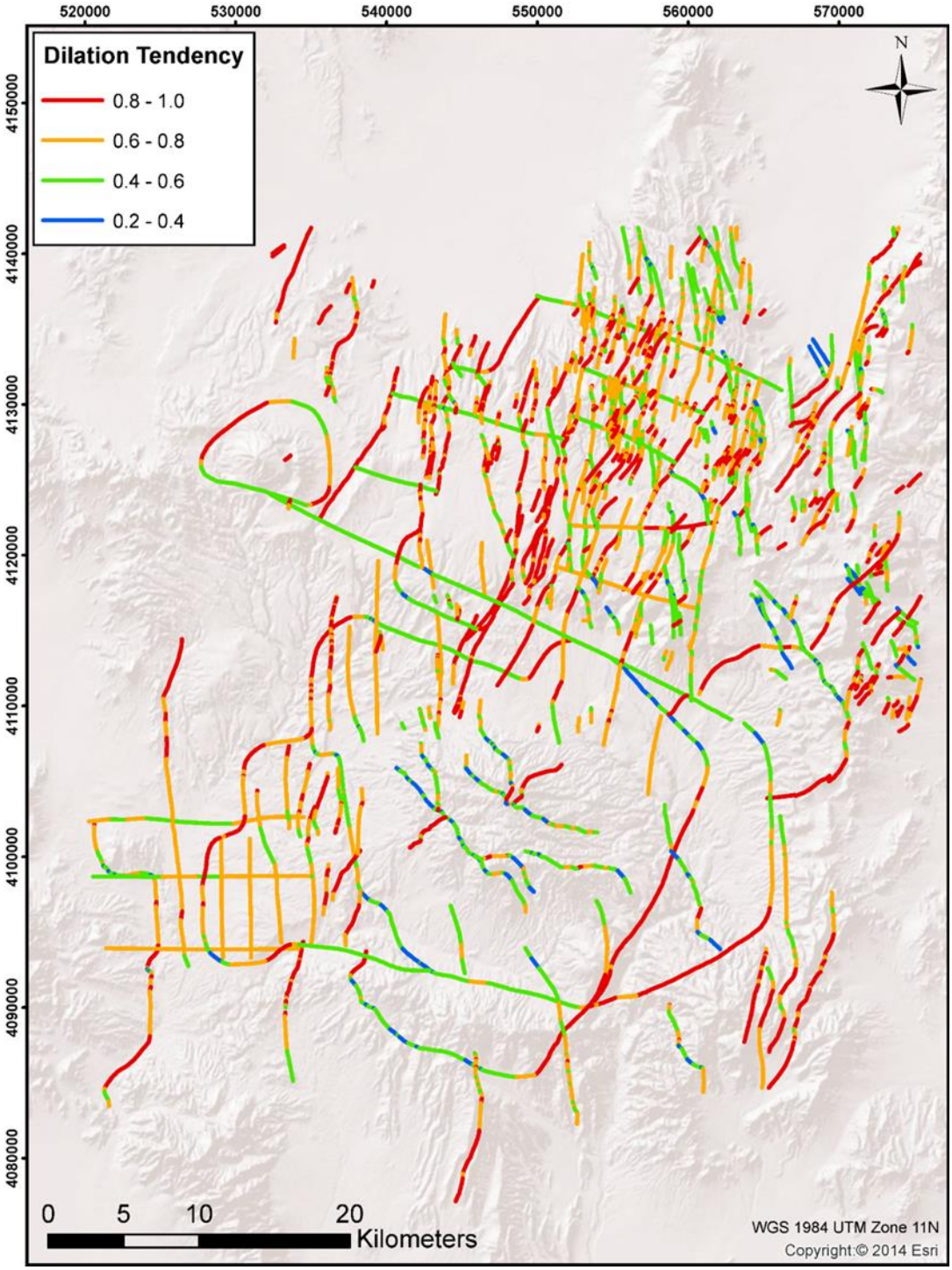

Figure 17. Fault dilation tendency given spatially variable horizontal stress directions from SATSI solutions for low horizontal stress anisotropy: S_{Hmax}/S_{hmin} = 1.5.

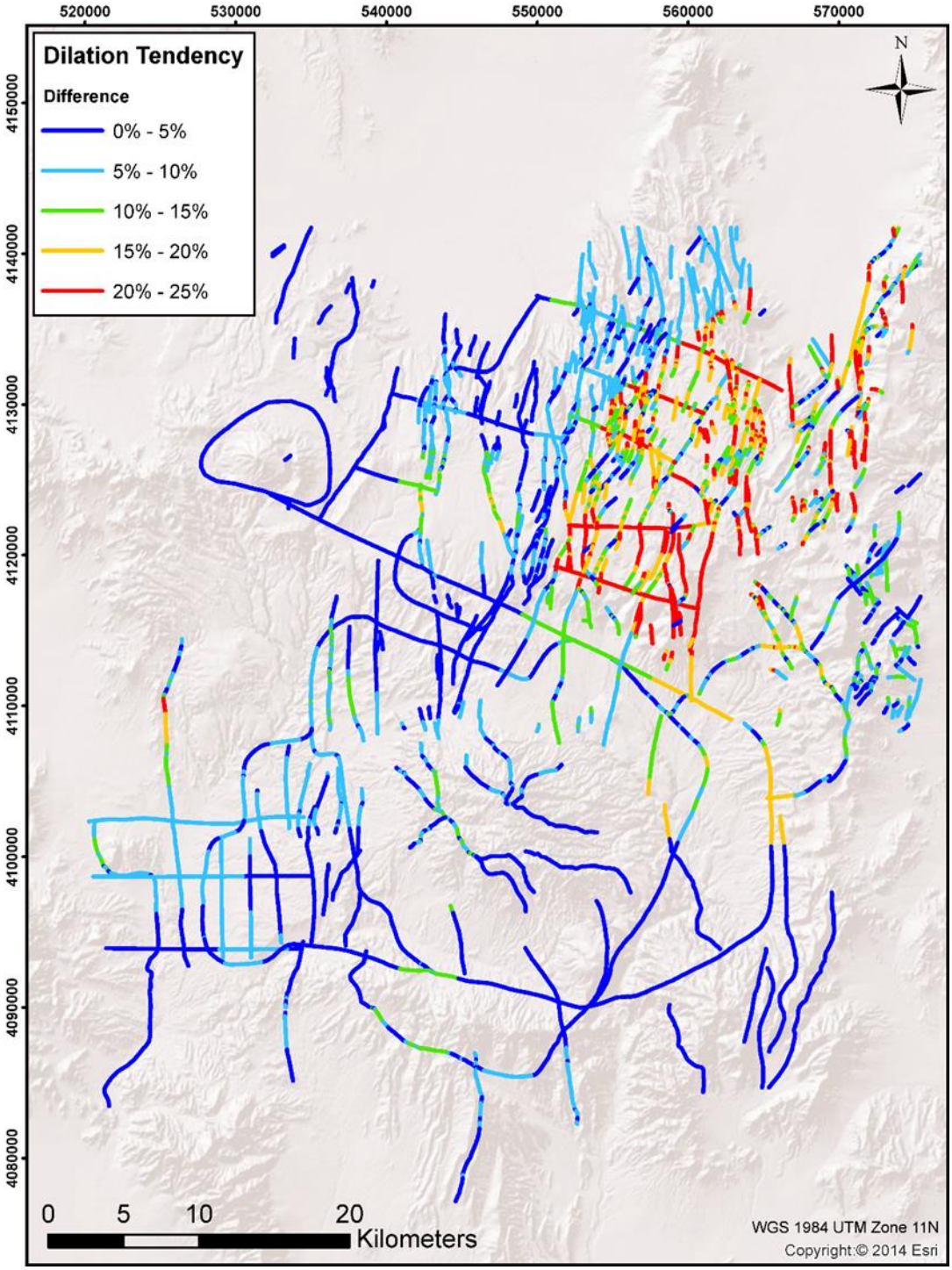

Figure 18. Difference in fault dilation tendency, expressed as percent error, between constant and spatially variable SATSI solutions for low horizontal stress anisotropy: S_{Hmax}/S_{hmin} = 1.5.

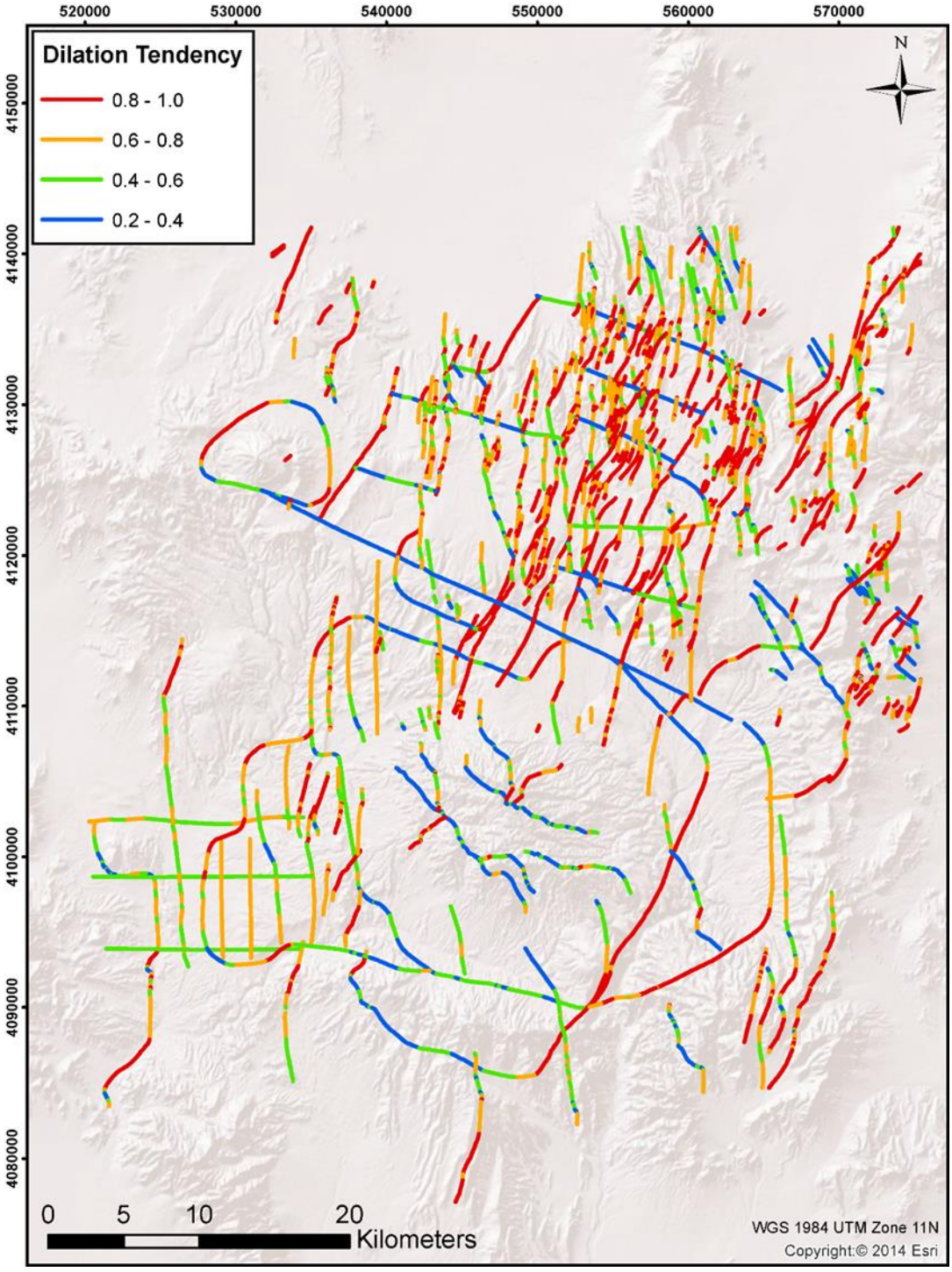

Figure 19. Fault dilation tendency given average horizontal stress directions computed from SATSI solutions for moderate horizontal stress anisotropy: $S_{Hmax}/S_{hmin} = 2.5$.

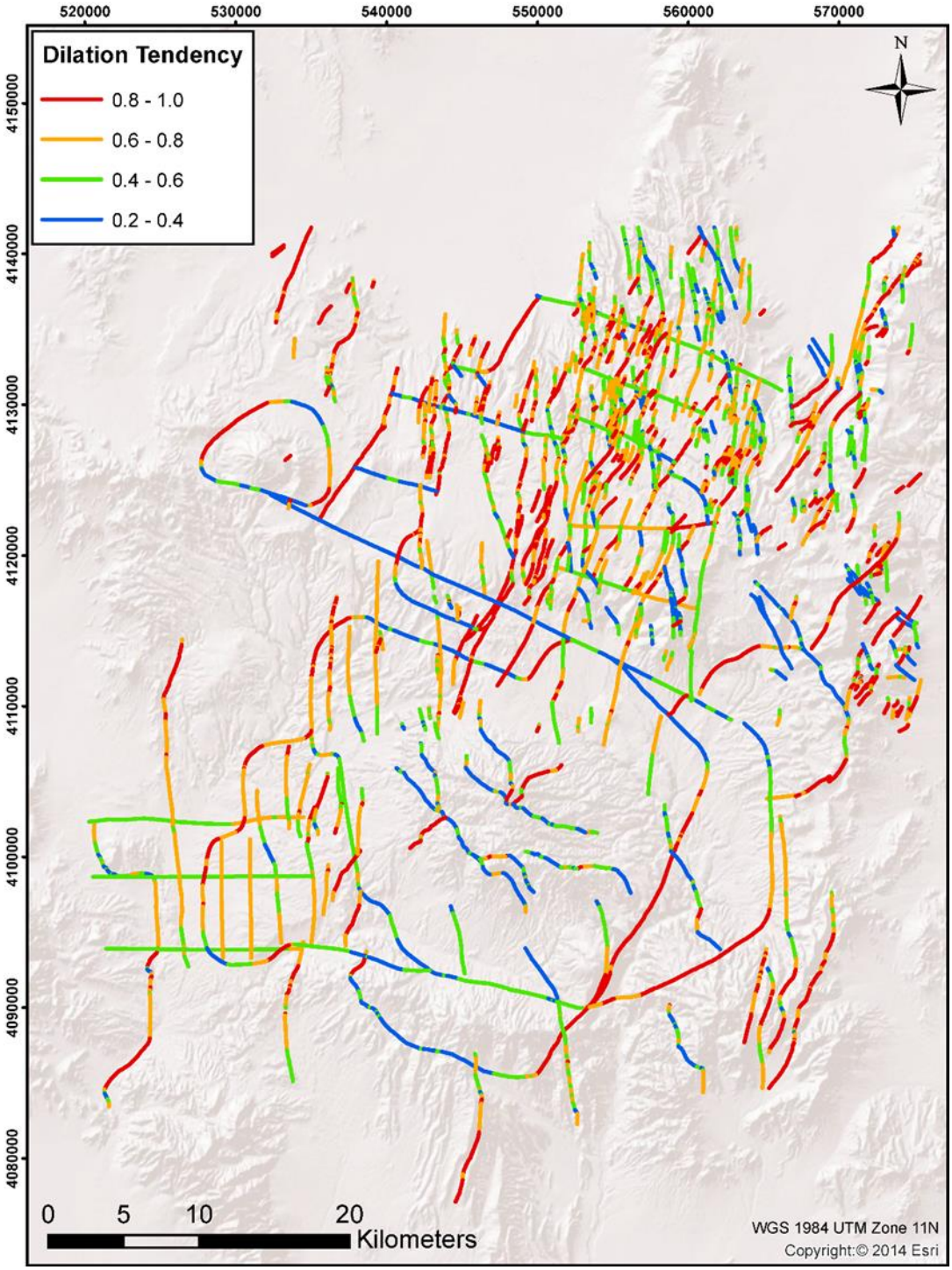

Figure 20. Fault dilation tendency given spatially variable horizontal stress directions from SATSI solutions for moderate horizontal stress anisotropy: S_{Hmax}/S_{hmin} = 2.5.

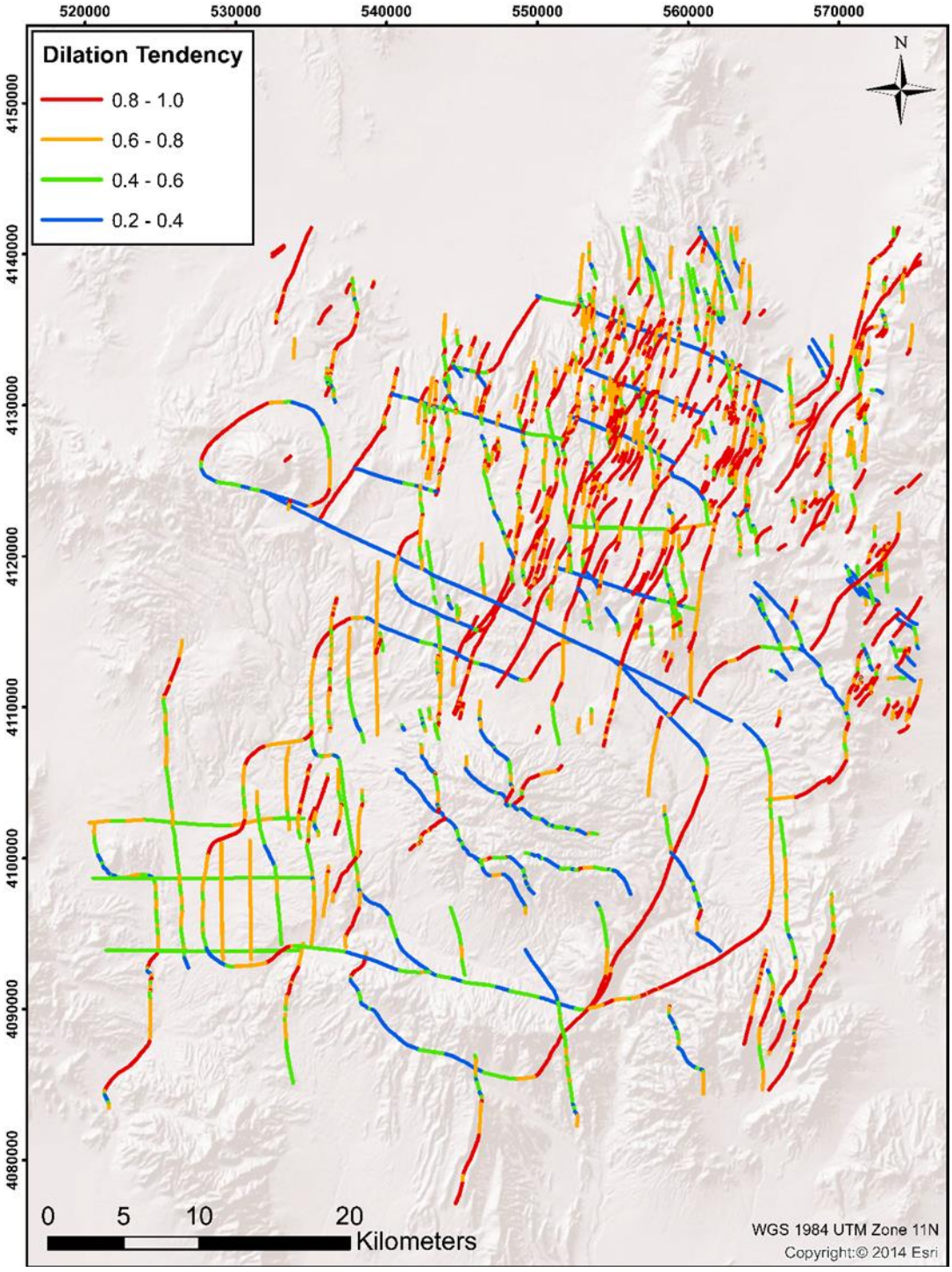

Figure 21. Fault dilation tendency given average horizontal stress directions computed from SATSI solutions for high horizontal stress anisotropy: S_{Hmax}/S_{hmin} = 3.2.

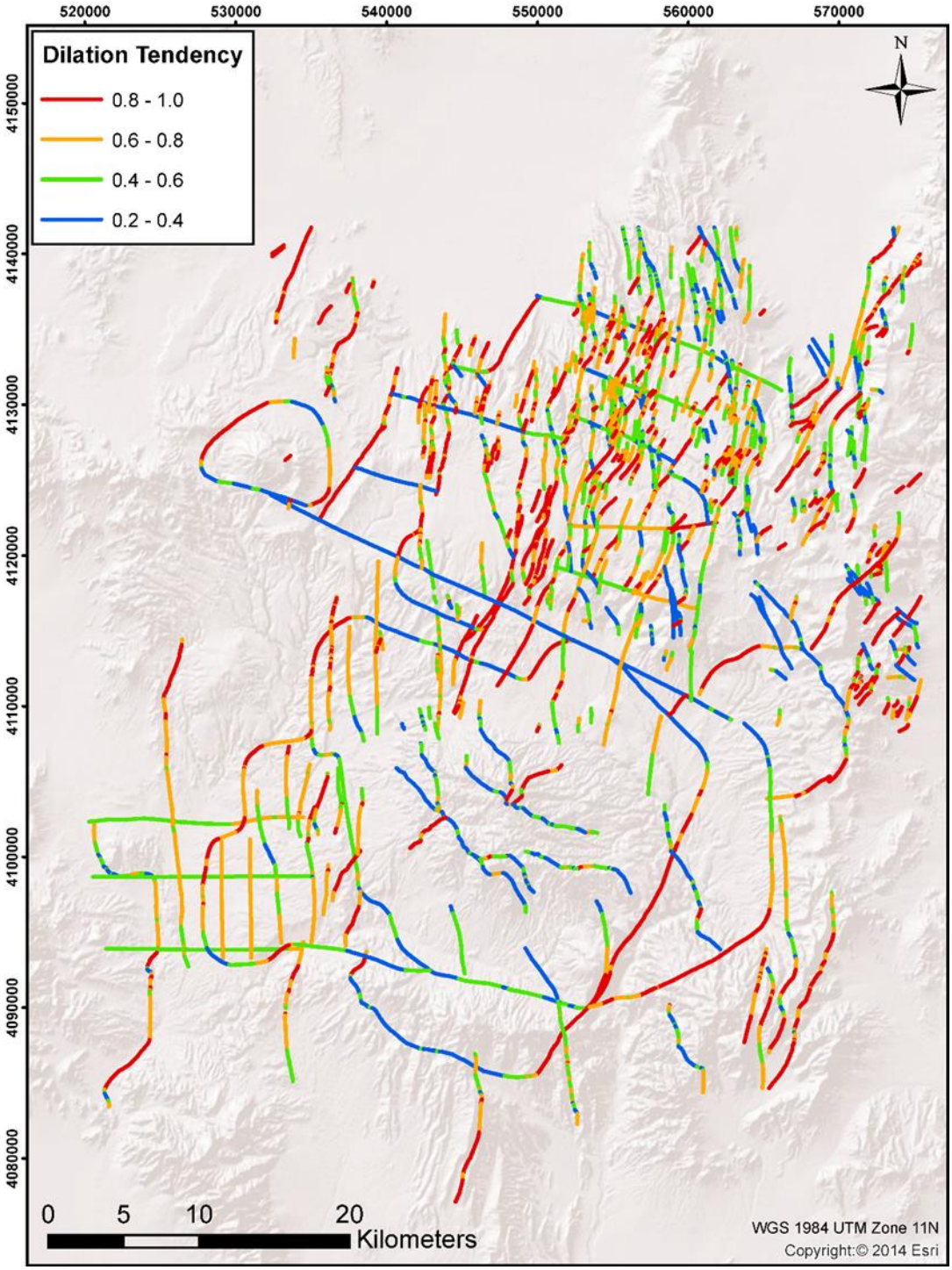

Figure 22. Fault dilation tendency given spatially variable horizontal stress directions from SATSI solutions for high horizontal stress anisotropy: S_{Hmax}/S_{hmin} = 3.2.

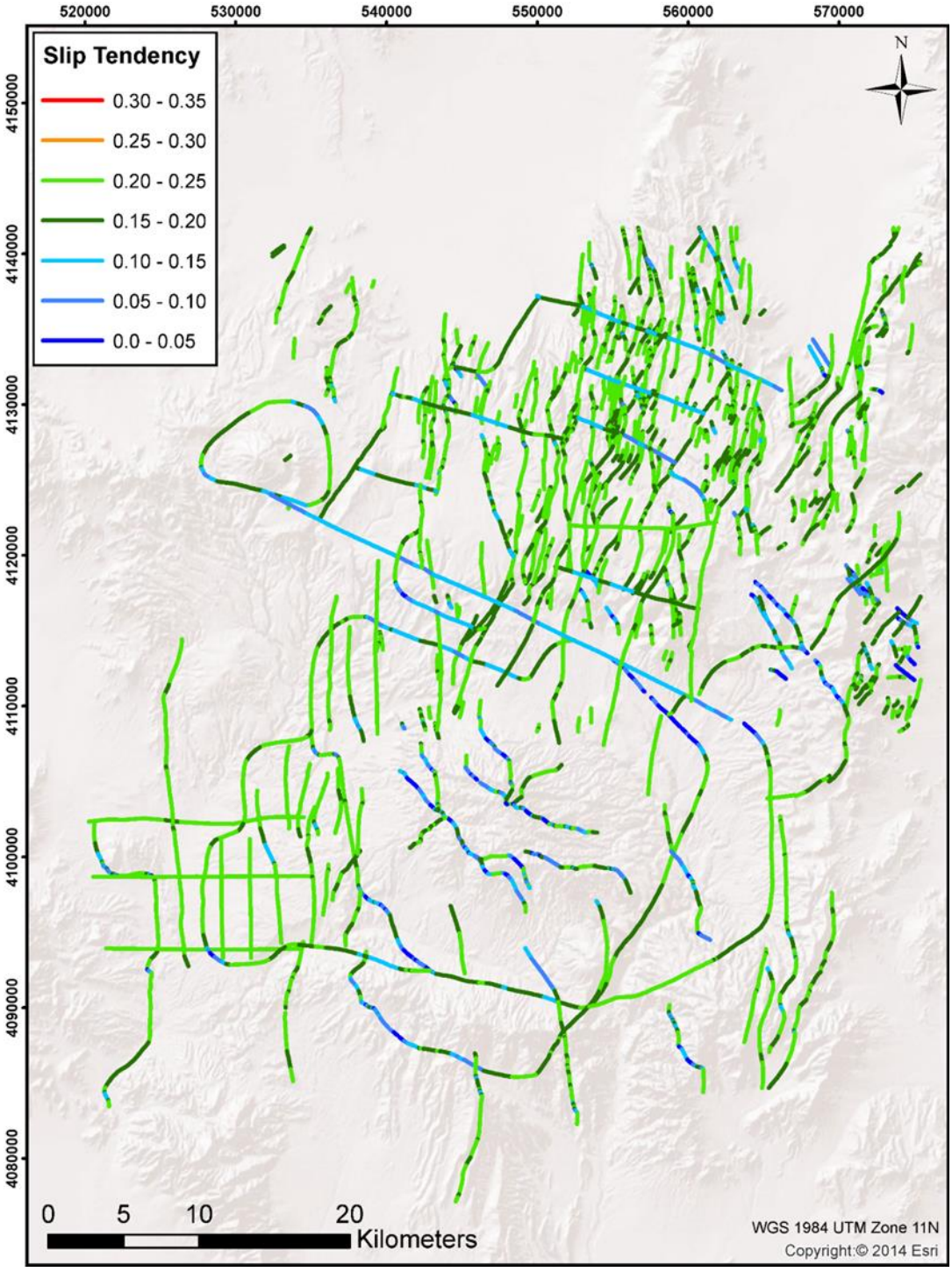

Figure 23. Slip tendency given average horizontal stress directions computed from SATSI solutions for low horizontal stress anisotropy: S_{Hmax}/S_{hmin} = 1.5.

Spatial Trends in Slip Tendency

Slip tendency computed from all 15,625 digitized segments of the Phase II Pahute Mesa faults (Figure 12) are shown for the constant (Figure 23) and spatially variable (Figure 24) SATSI stress field solutions. Faults with the highest slip tendency trend NE-SW in both stress fields (max = 0.23), with the lowest slip tendency values for NW-SE structures (min = 0.04). Note that all geologic structures are assigned a constant dip of 80°, which is considerably steeper than a more favorable 45 to 55° dip range for slip.

In-depth analyses to quantify differences in slip tendency values between constant and spatially variable SATSI stress field inversions are found in Section 3.2.4. Figure 25 spatially illustrates these differences through percent difference in slip tendency for these two stress conditions. Overall, the differences are greatest for the north-central to north-east region, corresponding to Western and Central Pahute Mesa CAUs, with maximum differences up to 200 percent. Note that the Western and Central Pahute Mesa CAUs contain both the highest density of faults and SATSI stress field solutions (Figure 13).

Maximum and number of high dilation tendency values significantly increase with increasing horizontal stress anisotropy ratio (Tables 4 and 5, Figures 26 through 29). The most significant observation is the complete lack of critically stressed faults until S_{Hmax}/S_{hmin} approaches 3.0. At S_{Hmax}/S_{hmin} equal to 3.2, the slip tendency maps look somewhat similar to dilation tendency with a similar number of dilated and critically stressed fault segments. The spatial distribution of differences in slip tendency between constant and spatially variable stress fields for the intermediate and high horizontal stress anisotropy cases are similar to the base case and are not shown.

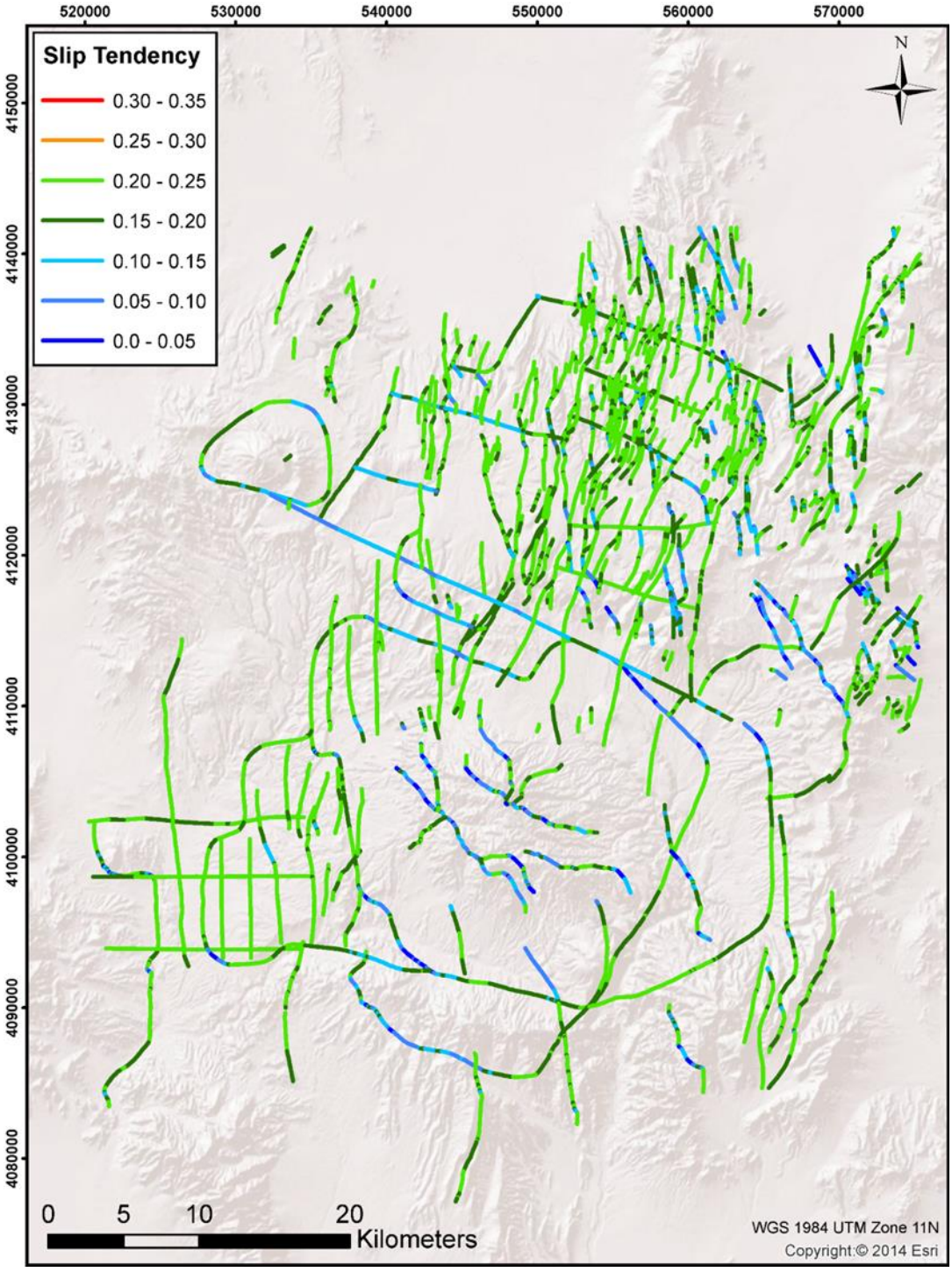

Figure 24. Slip tendency given spatially variable horizontal stress directions from SATSI solutions for low horizontal stress anisotropy: S_{Hmax}/S_{hmin} = 1.5.

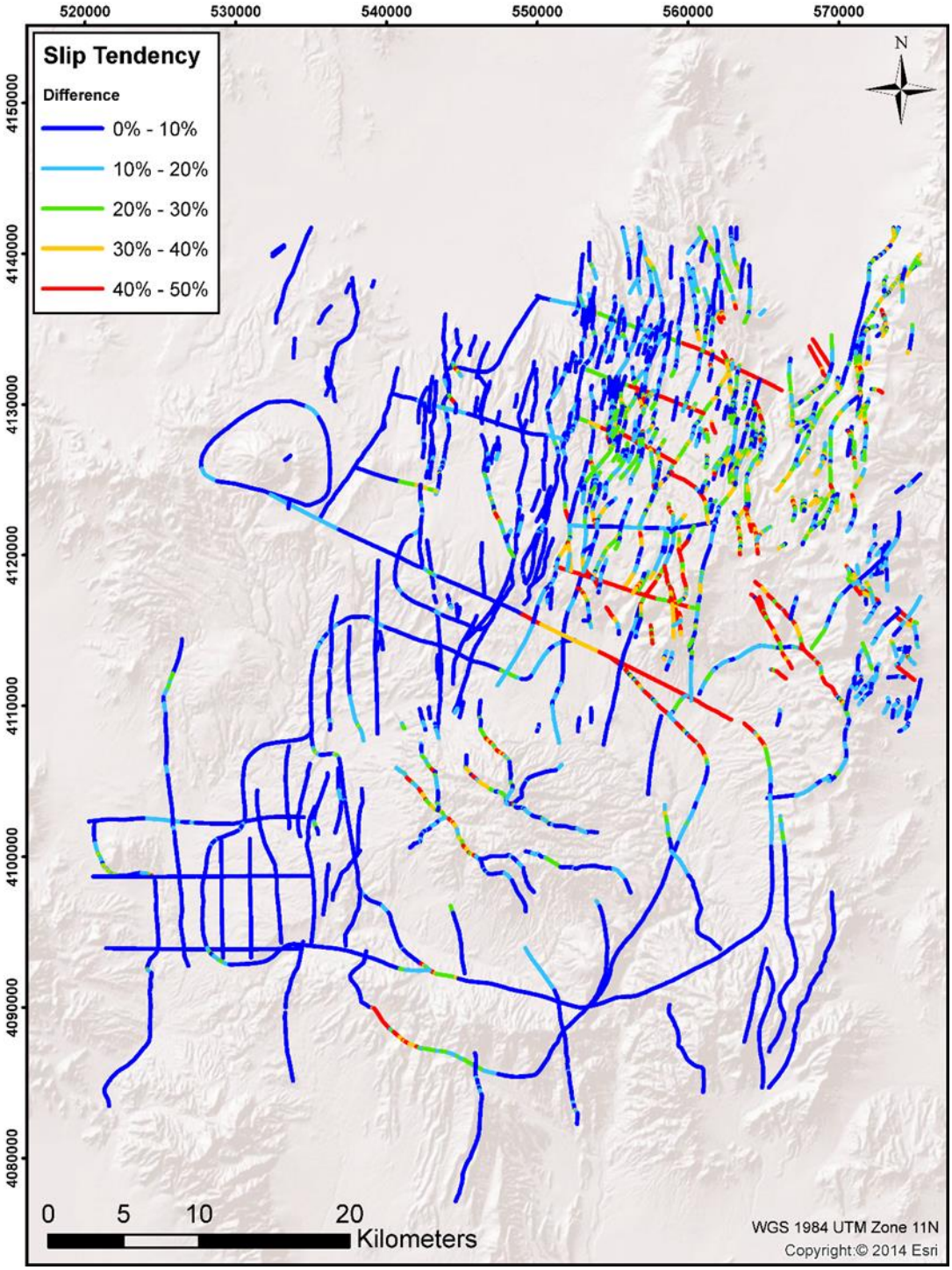

Figure 25. Difference in fault slip 3tendency, expressed as percent error, between constant and spatially variable SATSI solutions for low horizontal stress anisotropy: S_{Hmax}/S_{hmin} = 1.5.

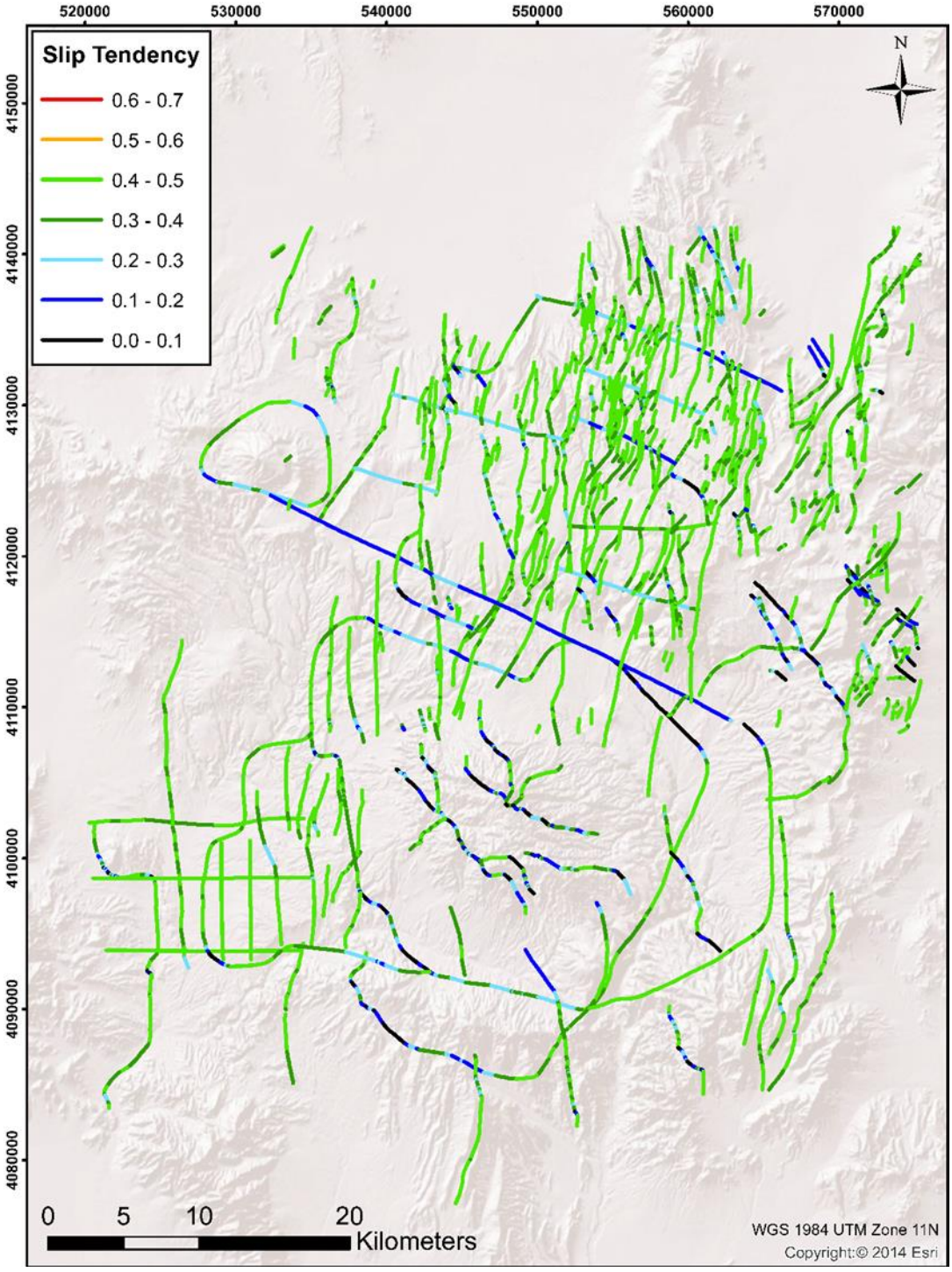

Figure 26. Slip tendency given average horizontal stress directions computed from SATSI solutions for moderate horizontal stress anisotropy: S_{Hmax}/S_{hmin} = 2.5.

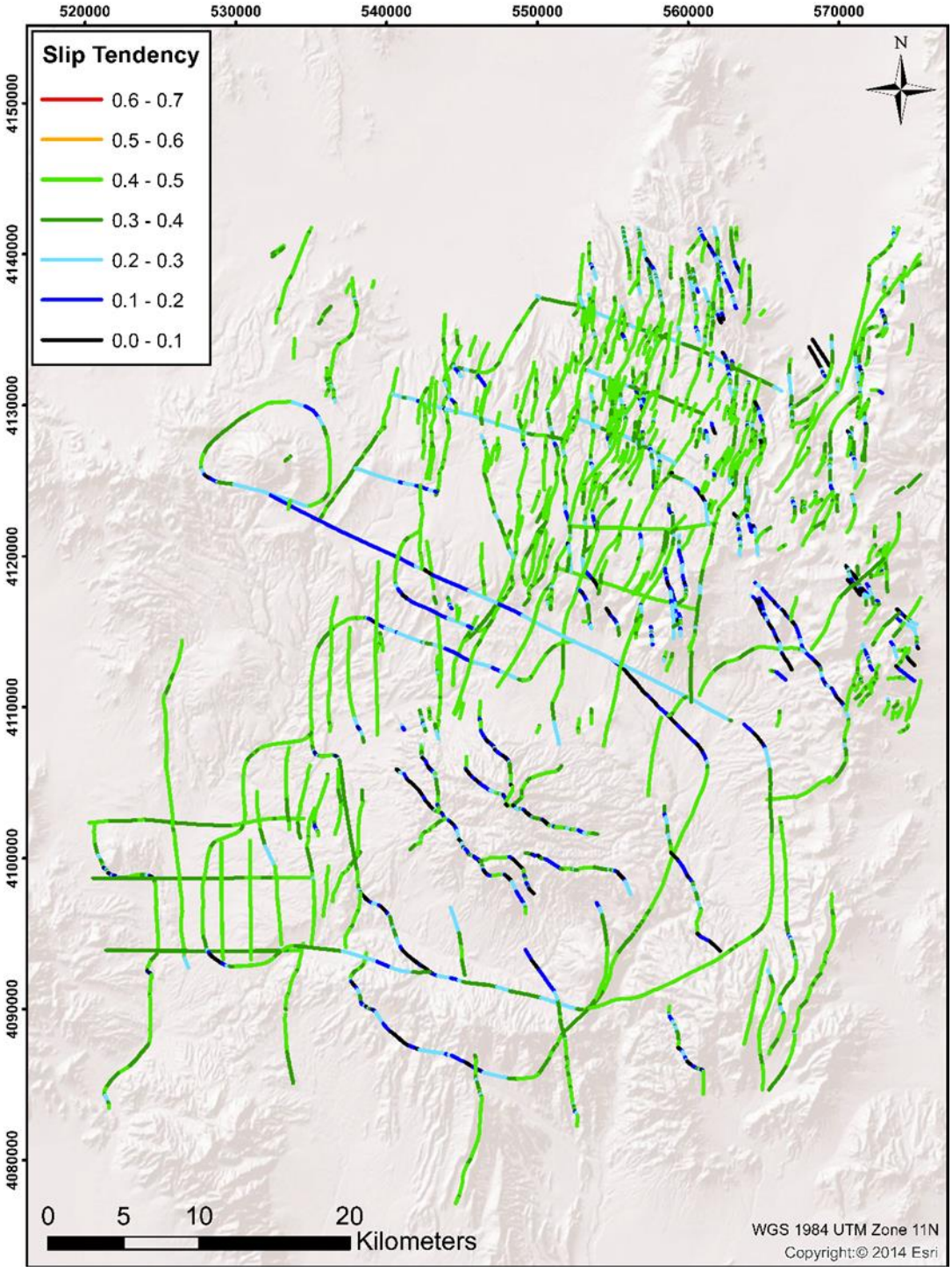

Figure 27. Slip tendency given spatially variable horizontal stress directions from SATSI solutions for moderate horizontal stress anisotropy: S_{Hmax}/S_{hmin} = 2.5.

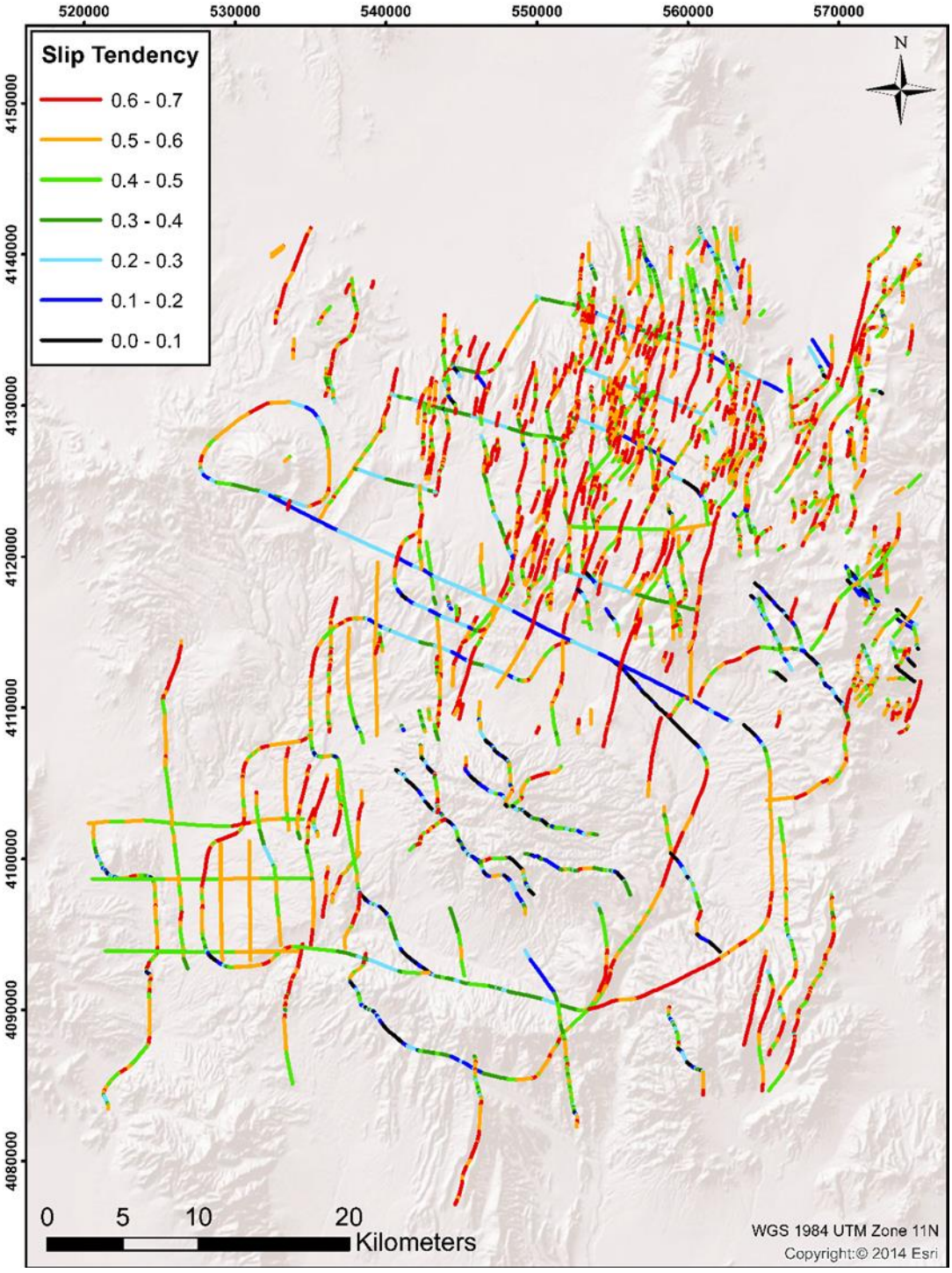

Figure 28. Slip tendency given average horizontal stress directions computed from SATSI solutions for high horizontal stress anisotropy: S_{Hmax}/S_{hmin} = 3.2.

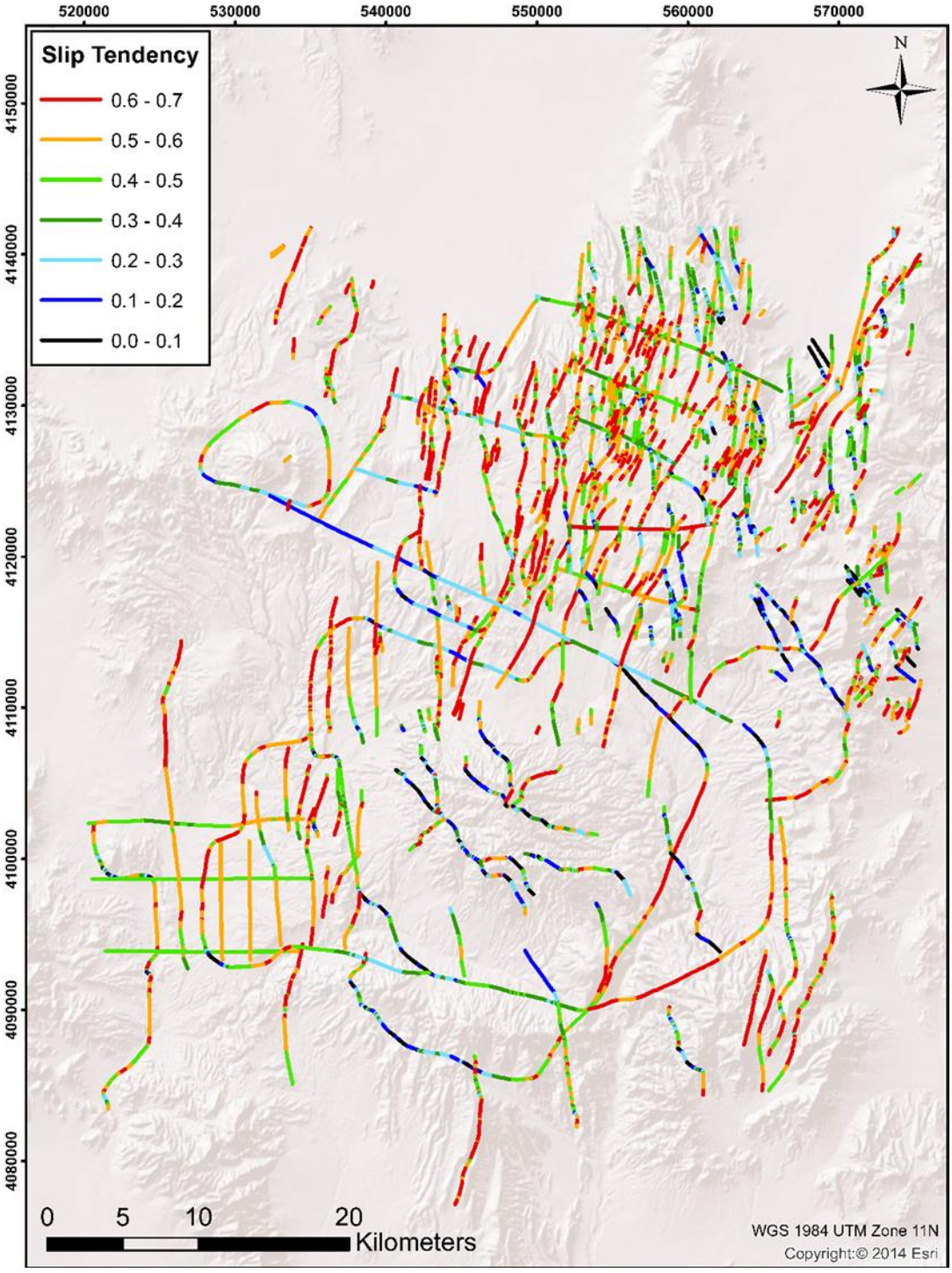

Figure 29. Slip tendency given spatially variable horizontal stress directions from SATSI solutions for high horizontal stress anisotropy: S_{Hmax}/S_{hmin} = 3.2.

Influence of Constant versus Variable Stress Field

The spatial distribution of the difference between dilation and slip tendency values computed using constant and spatially variable horizontal stress directions are presented in Figures 18 and 25. The dominant trend in both of these figures is that the greatest differences are concentrated in the north-central to north-east region of the domain, corresponding to Western and Central Pahute Mesa CAUs. This region contains the highest density of faults and SATSI stress field inversion solutions (Figure 13). A more thorough characterization of these differences is presented to precisely define how stress field directions influence resultant dilation and slip tendency values.

Root mean square deviation (RMSD):

$$RMSD_{i,i\in 1,2} = \sqrt{\frac{\sum_{j=1}^{n}\left(\overline{T}_{i,j} - T_{i,j}\right)^2}{n}} \tag{9}$$

where $\overline{T}_{i,j}$ represents fault segment j for T_d when i = 1 and T_s when i = 2, respectively, and n = total number of fault segments, is used to compute percent deviation for the three horizontal stress anisotropy cases. Values of RMSD range from 9 percent to 13 percent for dilation tendency and 17 percent to 26 percent for slip tendency, with values of RMSD increasing with S_{Hmax}/S_{hmin} (Table 6). The RMSD is approximately twice as high for slip tendency values as dilation tendency values (Table 6), which is in agreement with the color scales used in Figures 18 and 25.

Table 6. Root mean square deviation between dilation and slip tendency values for constant and variable stress directions expressed as a percent.

S_{Hmax}/S_{hmin}	T_d	T_s
1.5	9%	17%
2.5	12%	24%
3.2	13%	26%

Probability histograms of dilation and slip tendency values computed for each of the 15,625 fault segments are presented in Figures 30 and 31 for S_{Hmax}/S_{hmin} = 1.5 and S_{Hmax}/S_{hmin} = 3.2, respectively. Both figures show considerable overlap and consistency in the distribution of dilation and slip tendency values. The most notable differences are: (1) in general, dilation and slip tendency values are biased higher for the constant stress cases and (2) a considerable concentration in dilation tendency of 0.7 for S_{Hmax}/S_{hmin} = 1.5 and 0.65 and S_{Hmax}/S_{hmin} = 3.2 is observed for the constant stress case.

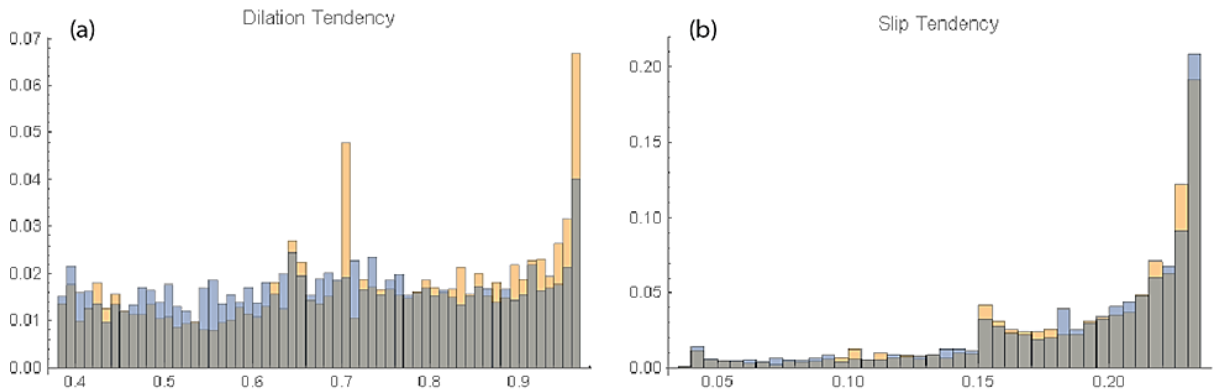

Figure 30. Probability histogram showing difference in distribution of (a) dilation tendency values (x-axis) and (b) slip tendency values (x-axis) computed using average stress field (tan) versus spatially variable stress field (blue) for S_{Hmax}/S_{hmin} = 1.5. Overlap is shown in gray.

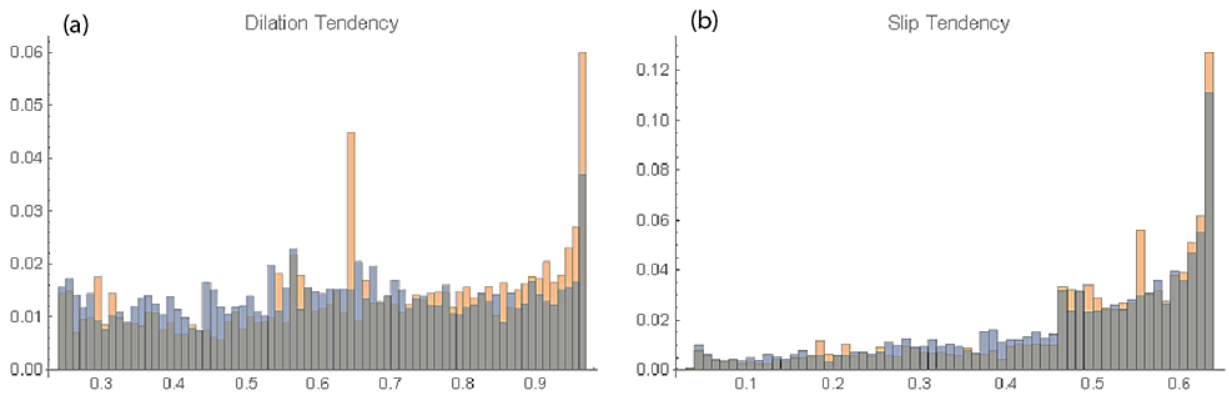

Figure 31. Probability histogram showing difference in distribution of (a) dilation tendency values (x-axis) and (b) slip tendency values (x-axis) computed using average stress field (tan) versus spatially variable stress field (blue) for S_{Hmax}/S_{hmin} = 3.2. Overlap is shown in gray.

The bias toward higher dilation and slip tendency values is further illustrated in Figures 32 and 33 where the average of these metrics assigned to each of the 394 faults and structures are plotted as variable versus constant stress orientations for S_{Hmax}/S_{hmin} = 1.5 and S_{Hmax}/S_{hmin} = 3.2. Visual inspection of the plots show that the central tendency of the data points is below the 1:1 line, signifying that values for individual structures are higher for the constant stress field cases. This conclusion is confirmed by a slope of less than one for all the data sets.

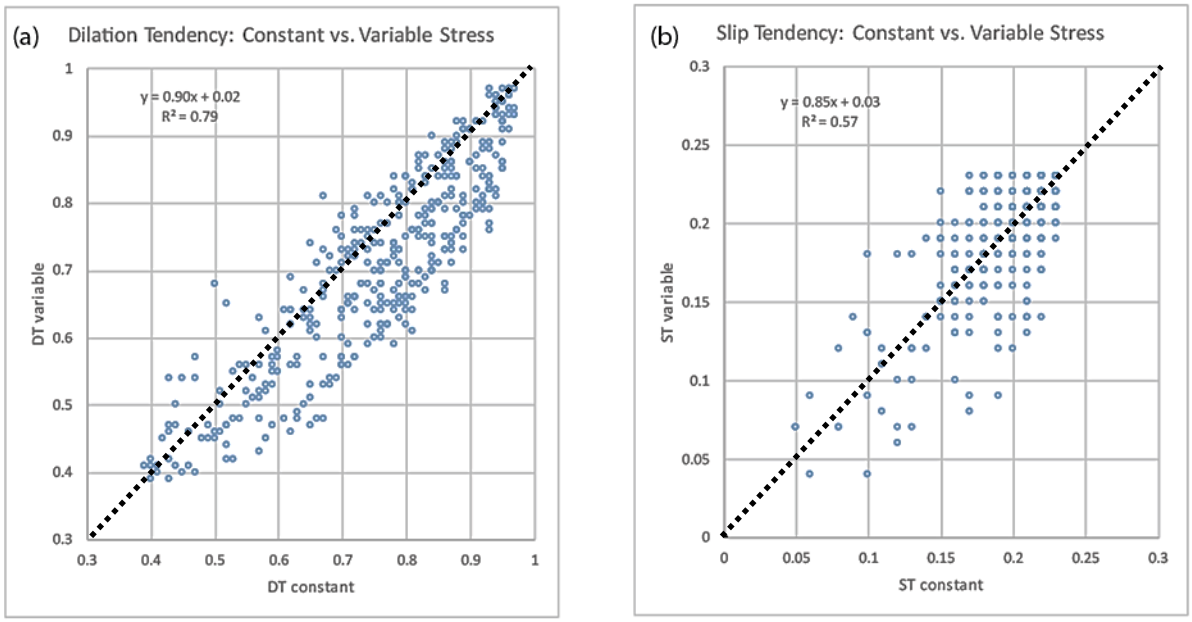

Figure 32. Plot of average dilation tendency values for all 394 faults for variable versus constant stress directions given S_{Hmax}/S_{hmin} = 1.5. Dashed black line denotes 1:1 trend.

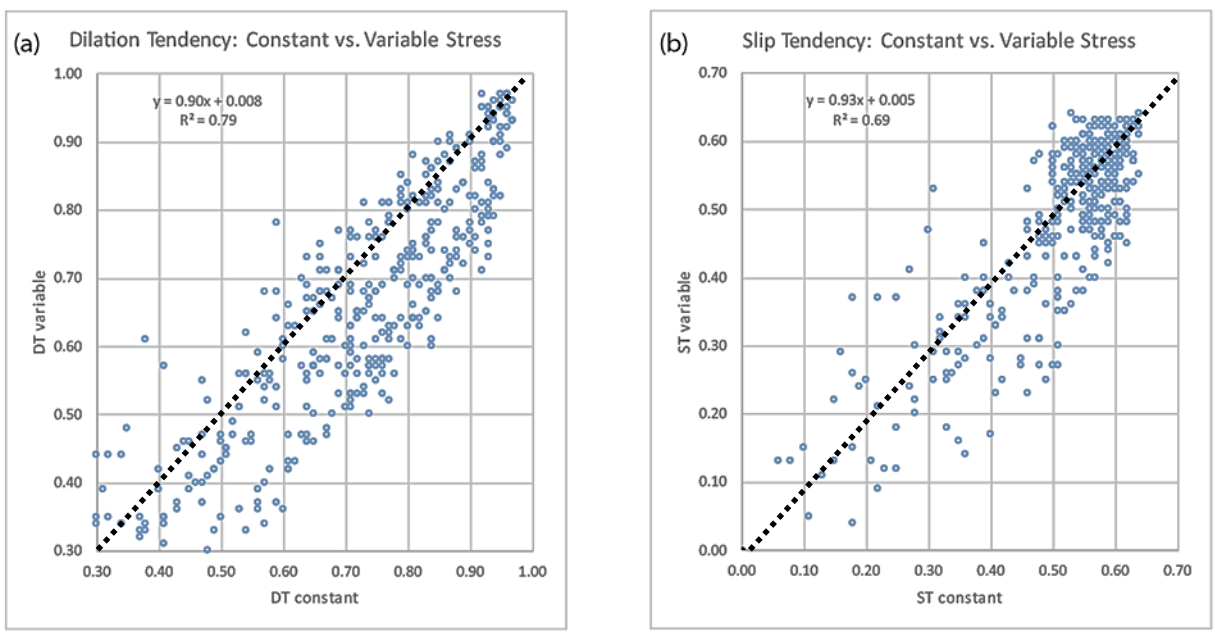

Figure 33. Plot of average dilation tendency values for all 394 faults for variable versus constant stress directions given S_{Hmax}/S_{hmin} = 3.2. Dashed black line denotes 1:1 trend.

PM Faults Dilated or Critically Stressed for Fluid Flow

Dilation and slip tendency values were averaged for all segments corresponding to each fault and structure zone shown in the combined NSTec (2014) and Slate *et al.* (1999) fault map (Figure 12) for each of the three horizontal stress anisotropy cases. A direct relationship between either dilation tendency or slip tendency and fault permeability does not exist, and therefore faults are arbitrarily considered enhanced for fluid flow in this study when either dilated: $T_d \geq 0.80$ or critically stressed: $T_s \geq 0.60$. Systematic trends in the deviation between these metrics given constant versus spatially variable stress directions are shown in detail in Section 3.2.4; and in general, constant stress field directions generate higher values than variable stress directions. For simplicity, dilation and slip tendency generated using constant and variable stress fields are averaged for each stress anisotropy ratio. These averages are then used to determine if the faults or structural zones are oriented within the stress field such that they are considered enhanced for fluid flow.

Dilation and slip tendency values are presented in Table 7 for the 79 Pahute Mesa Phase II faults and structural zones in Figure 11. Structures identified for enhanced flow for any of the three horizontal stress anisotropy cases are highlighted, with only 20 percent of the structures in Table 7 falling into this category, predominately attributed to high values of dilation tendency. The entire 394 set of structures shown in Figure 12 is provided in Appendix D. Of the entire set, 157 structures, corresponding to approximately 40 percent of the total, are identified for enhanced flow under any of the three stress fields. The enhanced flow designation was assigned to 151 structures on the basis of high values of dilation tendency, and 58 structures were assigned because of the high values of slip tendency. A total of 52 of the 58 (~90 percent) critically stressed structures also had dilation tendency values exceeding 0.8. The six structures identified solely on the basis of slip tendency have dilation tendency values just slightly under 0.80 threshold. As the base case horizontal stress anisotropy ratio is considered the most likely scenario, these results show that critically stressed structures exert relatively little influence on the enhanced flow designation. Moreover, increases in horizontal stress anisotropy were shown to only minimally affect dilation tendency values, and therefore the recommendation is to designate structures for enhanced flow on the basis of dilation tendency alone.

Table 7. Average values of dilation and slip tendency for the low, moderate and high stress anisotropy ratios, denoted as S_{Hmax}/S_{hmin} equal to 1.5, 2.5, and 3.2, respectively, for PM Phase II structures.

Faults	**Symbol**	**Dilation Tendency**			**Slip Tendency**		
		Low	**Mod**	**High**	**Low**	**Mod**	**High**
ER-20-7 Fault	20_7	**0.80**	0.76	0.76	0.21	0.45	0.57
ER-20-8 Fault	20_8	**0.94**	**0.94**	**0.93**	0.18	0.40	0.54
Almendro	AL	**0.84**	**0.81**	**0.81**	0.20	0.43	0.57
Ammonia Tanks caldera structural margin	ATCSM	0.64	0.58	0.57	0.16	0.32	0.40
Big Burn Valley fault	BBV	0.61	0.54	0.52	0.15	0.28	0.35
Bare Mountain fault	BM	0.75	0.70	0.69	0.22	0.44	0.55

Table 7. Average values of dilation and slip tendency for the low, moderate and high stress anisotropy ratios, denoted as S_{Hmax}/S_{hmin} equal to 1.5, 2.5, and 3.2, respectively, for PM Phase II structures (continued).

Faults	Symbol	Dilation Tendency			Slip Tendency		
		Low	Mod	High	Low	Mod	High
Black Mountain Caldera structural margin	BMCSM	0.67	0.61	0.60	0.17	0.34	0.43
Buteo	BU	0.77	0.73	0.73	0.20	0.41	0.52
Beatty Wash fault	BW	0.73	0.68	0.67	0.20	0.39	0.49
Boxcar fault	BX	**0.82**	0.79	0.78	0.21	0.45	0.58
Claim Canyon Caldera structural margin	CCCSM	0.67	0.61	0.59	0.16	0.31	0.39
Colson Pond Fault	CPF	0.64	0.58	0.57	0.22	0.40	0.48
East Estuary fault	EE	0.63	0.56	0.54	0.18	0.35	0.43
East Greeley fault	EG	0.70	0.64	0.63	0.21	0.42	0.52
East Thirsty Canyon structural zone	ETCSZ	0.74	0.69	0.69	0.23	0.46	0.56
Fleur-de-Lis fault	FDL	0.63	0.57	0.55	0.22	0.40	0.48
Grouse Canyon Caldera Margin	GCCSMNW	**0.85**	**0.82**	**0.82**	0.18	0.40	0.52
Handley fault	HA	**0.92**	**0.91**	**0.91**	0.19	0.42	0.56
Hogback fault	HOG	0.73	0.68	0.67	0.22	0.44	0.54
Hot Springs Lineament	HSL	0.64	0.57	0.56	0.22	0.40	0.48
Moat Fault #10	M10	0.75	0.70	0.69	0.23	0.47	0.58
Moat Fault #14	M14	0.54	0.45	0.43	0.15	0.27	0.31
Moat Fault #19	M19	0.58	0.51	0.49	0.20	0.35	0.42
Moat Fault #2	M2	0.68	0.63	0.61	0.22	0.43	0.52
Moat Fault #22	M22	**0.84**	**0.81**	**0.81**	0.21	0.45	0.58
Moat Fault #23	M23	**0.92**	**0.91**	**0.91**	0.19	0.41	0.56
Moat Fault #24	M24	0.77	0.73	0.72	0.23	0.47	**0.60**
Moat Fault #25	M25	0.72	0.67	0.66	0.22	0.44	0.55
Moat Fault #26	M26	0.63	0.57	0.55	0.21	0.39	0.47
Moat Fault #27	M27	0.72	0.67	0.66	0.23	0.46	0.56
Moat Fault #28	M28	0.73	0.68	0.67	0.23	0.46	0.56
Moat Fault #29	M29	0.73	0.68	0.67	0.23	0.46	0.56
M3 Fault	M3	0.72	0.67	0.65	0.23	0.45	0.56
Moat Fault #30	M30	0.71	0.66	0.64	0.22	0.43	0.53
Moat Fault #31	M31	0.76	0.73	0.72	0.21	0.44	0.56
Moat Fault #32	M32	0.76	0.72	0.71	0.22	0.46	0.58
Moat Fault #33	M33	0.71	0.66	0.65	0.23	0.44	0.55
Moat Fault #4	M4	0.66	0.60	0.58	0.21	0.40	0.49
M5N	M5N	**0.80**	0.77	0.76	0.23	0.48	**0.61**
M5S	M5S	0.75	0.71	0.70	0.23	0.46	0.57

Table 7. Average values of dilation and slip tendency for the low, moderate and high stress anisotropy ratios, denoted as S_{Hmax}/S_{hmin} equal to 1.5, 2.5, and 3.2, respectively, for PM Phase II structures (continued).

Faults	**Symbol**	**Dilation Tendency**			**Slip Tendency**		
		Low	**Mod**	**High**	**Low**	**Mod**	**High**
Moat Fault #6	M6	0.59	0.51	0.50	0.17	0.32	0.38
Moor Hen Meadow structural zone	MHMSZ	0.51	0.42	0.39	0.16	0.27	0.31
Northern Timber Moat structural zone	NTMMSZ	0.45	0.35	0.32	0.11	0.19	0.22
Pah Canyon fault	PAH	0.57	0.49	0.47	0.16	0.30	0.36
Paintbrush Canyon fault	PC	0.63	0.56	0.55	0.21	0.39	0.47
Paintbrush Canyon Fault North	PCN	0.43	0.32	0.29	0.10	0.15	0.17
Purse fault	PU	0.75	0.70	0.69	0.21	0.43	0.54
Rainier Mesa 3	RaM3	0.75	0.71	0.70	0.20	0.41	0.51
Rainier Mesa 4	RaM4	**0.89**	**0.87**	**0.87**	0.20	0.45	0.59
Ribbon Cliff structural zone	RCSZ	0.48	0.39	0.36	0.14	0.25	0.28
Resurgent Dome Fault #1	RM1	0.46	0.36	0.34	0.11	0.19	0.22
Resurgent Dome Fault #10	RM10	**0.87**	**0.85**	**0.85**	0.20	0.43	0.57
Resurgent Dome Fault #2	RM2	0.56	0.47	0.46	0.14	0.26	0.32
Resurgent Dome Fault #4	RM4	**0.91**	**0.89**	**0.89**	0.19	0.42	0.56
Resurgent Dome Fault #5	RM5	0.58	0.49	0.48	0.17	0.31	0.37
Resurgent Dome Fault #6	RM6	0.54	0.46	0.44	0.16	0.28	0.33
Resurgent Dome Fault #7	RM7	0.52	0.43	0.41	0.14	0.25	0.29
Resurgent Dome Fault #9	RM9	0.59	0.52	0.51	0.15	0.28	0.35
Rainier Mesa caldera structural margin	RMCSM	0.74	0.69	0.68	0.20	0.40	0.51
Redrock Valley Caldera structural margin	RRVSM	**0.82**	0.79	0.79	0.20	0.42	0.55
Rickey fault	RY	0.77	0.74	0.73	0.22	0.45	0.57
Silent Canyon Northern structural zone	SCNSZ	0.52	0.44	0.42	0.17	0.29	0.34
Silent Canyon structural zone - east	SCSZE	0.48	0.39	0.36	0.13	0.22	0.26
Silent Canyon structural zone - west	SCSZW	0.50	0.41	0.38	0.15	0.25	0.30
Shoshone Mountain 10	SM10	0.74	0.69	0.68	0.21	0.43	0.54
Shoshone Mountain 20	SM20	0.73	0.68	0.67	0.21	0.41	0.52
Shoshone Mountain 30	SM30	**0.85**	**0.83**	**0.82**	0.20	0.43	0.56
Shoshone Mountain 6	SM6	**0.83**	**0.80**	**0.80**	0.23	0.49	**0.62**
Scrugham Peak fault	SP	0.78	0.74	0.74	0.22	0.45	0.57
Southern Pahute Mesa structural zone	SPMSZ	0.59	0.52	0.50	0.19	0.35	0.42
Split Ridge fault	SR	0.72	0.67	0.66	0.21	0.42	0.52

Table 7. Average values of dilation and slip tendency for the low, moderate and high stress anisotropy ratios, denoted as S_{Hmax}/S_{hmin} equal to 1.5, 2.5, and 3.2, respectively, for PM Phase II structures (continued).

Faults	Symbol	Dilation Tendency			Slip Tendency		
		Low	Mod	High	Low	Mod	High
Southwest Area 20 caldera margin	SWA20CSM Southwest Area 20 caldera margin	0.64	0.57	0.56	0.15	0.30	0.38
West Almendro	WAL	0.66	0.59	0.58	0.20	0.37	0.46
West Boxcar fault	WB	0.60	0.53	0.51	0.19	0.35	0.42
West Estuary fault	WE	0.71	0.66	0.64	0.21	0.41	0.51
West Greeley fault	WG	0.79	0.76	0.75	0.21	0.43	0.55
West Purse fault	WP	0.74	0.70	0.69	0.23	0.46	0.57
West Silent Canyon structural zone	WSCSZ	0.51	0.42	0.40	0.16	0.28	0.32
Windy Wash fault	WW	0.79	0.75	0.74	0.21	0.44	0.57
S1	S1	0.54	0.45	0.43	0.17	0.30	0.35
S2	S2	**0.88**	**0.86**	**0.86**	0.20	0.45	0.59
S3	S3	0.57	0.50	0.48	0.18	0.33	0.40
S4	S4	**0.89**	**0.88**	**0.87**	0.21	0.46	**0.61**
S5	S5	0.67	0.61	0.60	0.20	0.38	0.47
S6	S6	0.68	0.62	0.61	0.23	0.43	0.52
S7	S7	**0.94**	**0.93**	**0.93**	0.19	0.42	0.58
S8	S8	**0.95**	**0.95**	**0.95**	0.17	0.39	0.54
S9	S9	**0.81**	0.78	0.77	0.21	0.44	0.57
S10	S10	0.68	0.62	0.61	0.22	0.42	0.52
S11	S11	**0.95**	**0.95**	**0.95**	0.17	0.39	0.53
S12	S12	0.60	0.53	0.51	0.20	0.37	0.44
S13	S13	0.67	0.61	0.60	0.22	0.43	0.52
S14	S14	0.54	0.46	0.44	0.17	0.29	0.34
S15	S15	0.79	0.76	0.75	0.23	0.48	**0.61**
S16	S16	**0.91**	**0.89**	**0.89**	0.20	0.44	0.59
S17	S17	**0.95**	**0.95**	**0.95**	0.18	0.39	0.53
S18	S18	**0.91**	**0.89**	**0.89**	0.20	0.44	0.59
S19	S19	0.56	0.48	0.46	0.18	0.31	0.37
S20	S20	0.70	0.65	0.63	0.22	0.43	0.53
S21	S21	**0.80**	0.76	0.76	0.20	0.41	0.52
S22	S22	0.69	0.64	0.62	0.23	0.44	0.53
S23	S23	0.50	0.40	0.38	0.15	0.26	0.30
S24	S24	0.76	0.71	0.70	0.21	0.42	0.54
S25	S25	**0.87**	**0.84**	**0.84**	0.22	0.48	**0.63**
S26	S26	0.75	0.71	0.70	0.23	0.47	0.59
S27	S27	**0.91**	**0.89**	**0.89**	0.21	0.47	**0.63**

Table 7. Average values of dilation and slip tendency for the low, moderate and high stress anisotropy ratios, denoted as S_{Hmax}/S_{hmin} equal to 1.5, 2.5, and 3.2, respectively, for PM Phase II structures (continued).

Faults	Symbol	Dilation Tendency			Slip Tendency		
		Low	Mod	High	Low	Mod	High
S28	S28	0.73	0.68	0.67	0.21	0.42	0.53
S29	S29	0.55	0.47	0.45	0.18	0.32	0.37
S30	S30	**0.94**	**0.93**	**0.92**	0.19	0.43	0.57
S31	S31	0.68	0.62	0.61	0.22	0.41	0.50
S32	S32	0.76	0.72	0.71	0.22	0.45	0.56
S33	S33	0.59	0.52	0.50	0.19	0.35	0.42
S34	S34	0.74	0.70	0.69	0.22	0.43	0.55
S35	S35	0.53	0.44	0.42	0.17	0.29	0.34
S36	S36	0.71	0.66	0.65	0.20	0.40	0.50
S37	S37	0.69	0.63	0.62	0.18	0.35	0.45
S38	S38	**0.96**	**0.95**	**0.95**	0.17	0.38	0.52
S39	S39	0.52	0.43	0.41	0.16	0.28	0.32
S40	S40	0.75	0.71	0.70	0.18	0.37	0.47
S41	S41	0.72	0.67	0.66	0.22	0.44	0.54
S42	S42	0.78	0.74	0.73	0.23	0.47	0.59
S43	S43	0.48	0.38	0.36	0.13	0.22	0.26
S44	S44	**0.95**	**0.94**	**0.94**	0.17	0.38	0.52
S45	S45	0.74	0.69	0.68	0.21	0.43	0.54
S46	S46	0.63	0.57	0.55	0.20	0.38	0.46
S47	S47	0.75	0.70	0.69	0.23	0.47	0.58
S48	S48	**0.83**	**0.80**	**0.80**	0.23	0.48	**0.62**
S49	S49	0.79	0.75	0.75	0.22	0.45	0.57
S50	S50	0.73	0.68	0.67	0.18	0.36	0.47
S51	S51	0.60	0.52	0.50	0.17	0.31	0.38
S52	S52	0.64	0.58	0.57	0.22	0.41	0.49
S53	S53	0.71	0.66	0.65	0.22	0.44	0.55
S54	S54	0.77	0.73	0.72	0.23	0.47	0.59
S55	S55	0.73	0.68	0.67	0.23	0.46	0.56
S56	S56	0.58	0.50	0.48	0.17	0.32	0.39
S57	S57	**0.83**	**0.80**	**0.80**	0.23	0.48	**0.62**
S58	S58	**0.82**	0.78	0.78	0.22	0.45	0.58
S59	S59	0.73	0.68	0.67	0.22	0.44	0.54
S60	S60	**0.89**	**0.88**	**0.87**	0.21	0.46	**0.60**
S61	S61	**0.85**	**0.83**	**0.82**	0.22	0.48	**0.62**
S62	S62	0.75	0.71	0.70	0.23	0.48	0.59
S63	S63	**0.80**	0.77	0.76	0.23	0.48	**0.60**
S64	S64	**0.87**	**0.85**	**0.85**	0.22	0.48	**0.63**

Table 7. Average values of dilation and slip tendency for the low, moderate and high stress anisotropy ratios, denoted as S_{Hmax}/S_{hmin} equal to 1.5, 2.5, and 3.2, respectively, for PM Phase II structures (continued).

Faults	Symbol	Dilation Tendency			Slip Tendency		
		Low	Mod	High	Low	Mod	High
S65	S65	**0.90**	**0.89**	**0.89**	0.20	0.46	**0.61**
S66	S66	**0.92**	**0.91**	**0.90**	0.19	0.44	0.59
S67	S67	0.73	0.69	0.67	0.22	0.43	0.53
S68	S68	0.41	0.30	0.28	0.07	0.10	0.11
S69	S69	**0.84**	**0.81**	**0.81**	0.22	0.47	**0.60**
S70	S70	0.64	0.57	0.55	0.20	0.38	0.46
S71	S71	0.43	0.32	0.30	0.09	0.14	0.16
S72	S72	0.72	0.67	0.66	0.21	0.42	0.52
S73	S73	0.68	0.62	0.61	0.22	0.43	0.52
S74	S74	0.54	0.45	0.43	0.16	0.28	0.34
S75	S75	0.62	0.55	0.53	0.20	0.37	0.45
S76	S76	0.46	0.36	0.34	0.12	0.20	0.23
S77	S77	0.69	0.64	0.62	0.21	0.41	0.51
S78	S78	**0.93**	0.93	0.93	0.19	0.41	0.56
S79	S79	0.73	0.69	0.67	0.22	0.43	0.54
S80	S80	0.41	0.30	0.28	0.08	0.12	0.14
S81	S81	0.69	0.63	0.62	0.22	0.43	0.52
S82	S82	0.61	0.54	0.52	0.19	0.36	0.43
S83	S83	0.76	0.72	0.71	0.22	0.46	0.57
S84	S84	**0.81**	0.78	0.78	0.20	0.41	0.53
S85	S85	0.59	0.51	0.49	0.18	0.32	0.39
S86	S86	0.73	0.69	0.67	0.23	0.46	0.57
S87	S87	0.71	0.66	0.65	0.21	0.41	0.52
S88	S88	0.73	0.68	0.66	0.21	0.42	0.52
S89	S89	0.78	0.74	0.73	0.23	0.47	0.59
S90	S90	**0.89**	**0.88**	**0.87**	0.20	0.44	0.58
S91	S91	**0.89**	**0.87**	**0.87**	0.19	0.42	0.55
S92	S92	0.74	0.69	0.68	0.23	0.47	0.57
S93	S93	**0.83**	**0.80**	**0.80**	0.21	0.45	0.58
S94	S94	0.79	0.75	0.75	0.20	0.42	0.54
S95	S95	**0.95**	**0.94**	**0.94**	0.18	0.39	0.54
S96	S96	0.79	0.75	0.74	0.23	0.47	**0.60**
S97	S97	0.79	0.75	0.74	0.23	0.49	**0.61**
S98	S98	0.76	0.72	0.71	0.22	0.46	0.57
S99	S99	**0.81**	0.78	0.77	0.22	0.46	0.59
S100	S100	0.71	0.66	0.65	0.22	0.44	0.54
S101	S101	**0.89**	**0.87**	**0.87**	0.20	0.43	0.57

Table 7. Average values of dilation and slip tendency for the low, moderate and high stress anisotropy ratios, denoted as S_{Hmax}/S_{hmin} equal to 1.5, 2.5, and 3.2, respectively, for PM Phase II structures (continued).

Faults	Symbol	Dilation Tendency			Slip Tendency		
		Low	Mod	High	Low	Mod	High
S102	S102	**0.86**	**0.84**	**0.84**	0.22	0.49	**0.64**
S103	S103	0.78	0.74	0.74	0.23	0.48	**0.60**
S104	S104	0.44	0.33	0.31	0.10	0.16	0.19
S105	S105	**0.80**	0.77	0.76	0.23	0.49	**0.62**
S106	S106	**0.92**	**0.92**	**0.92**	0.19	0.42	0.56
S107	S107	0.75	0.71	0.70	0.22	0.45	0.56
S108	S108	**0.80**	0.76	0.75	0.21	0.43	0.55
S109	S109	0.70	0.64	0.63	0.22	0.43	0.52
S110	S110	**0.86**	**0.84**	**0.83**	0.21	0.44	0.57
S111	S111	**0.81**	0.78	0.77	0.23	0.47	**0.60**
S112	S112	0.78	0.74	0.73	0.22	0.46	0.58
S113	S113	0.74	0.69	0.68	0.23	0.46	0.56
S114	S114	0.75	0.71	0.70	0.23	0.46	0.58
S115	S115	**0.85**	**0.83**	**0.82**	0.21	0.46	0.59
S116	S116	**0.88**	**0.87**	**0.86**	0.21	0.46	**0.61**
S117	S117	**0.80**	0.77	0.76	0.22	0.47	**0.60**
S118	S118	**0.86**	**0.84**	**0.83**	0.21	0.45	0.59
S119	S119	**0.82**	0.79	0.78	0.23	0.49	**0.62**
S120	S120	**0.81**	0.78	0.77	0.22	0.46	0.58
S121	S121	**0.89**	**0.87**	**0.87**	0.21	0.48	**0.63**
S122	S122	**0.81**	0.78	0.77	0.21	0.43	0.55
S123	S123	0.48	0.38	0.36	0.13	0.22	0.26
S124	S124	0.61	0.53	0.52	0.20	0.37	0.44
S125	S125	0.71	0.66	0.65	0.22	0.44	0.55
S126	S126	0.71	0.66	0.64	0.19	0.38	0.48
S127	S127	0.59	0.52	0.50	0.17	0.32	0.39
S128	S128	0.55	0.46	0.45	0.18	0.31	0.36
S129	S129	0.79	0.75	0.74	0.22	0.47	0.59
S130	S130	**0.87**	**0.85**	**0.84**	0.20	0.44	0.57
S131	S131	0.70	0.65	0.64	0.22	0.44	0.54
S132	S132	0.70	0.65	0.63	0.22	0.43	0.53
S133	S133	**0.82**	0.79	0.78	0.22	0.48	**0.61**
S134	S134	**0.84**	**0.81**	**0.80**	0.20	0.42	0.54
S135	S135	0.65	0.59	0.58	0.21	0.40	0.48
S136	S136	0.78	0.74	0.73	0.21	0.43	0.54
S137	S137	0.73	0.68	0.66	0.22	0.43	0.53
S138	S138	0.64	0.57	0.55	0.19	0.37	0.45

Table 7. Average values of dilation and slip tendency for the low, moderate and high stress anisotropy ratios, denoted as S_{Hmax}/S_{hmin} equal to 1.5, 2.5, and 3.2, respectively, for PM Phase II structures (continued).

Faults	Symbol	Dilation Tendency			Slip Tendency		
		Low	Mod	High	Low	Mod	High
S139	S139	0.74	0.70	0.69	0.22	0.45	0.57
S140	S140	**0.86**	**0.84**	**0.83**	0.21	0.46	**0.60**
S141	S141	**0.84**	**0.81**	**0.81**	0.22	0.47	**0.61**
S142	S142	**0.83**	0.79	0.79	0.22	0.47	**0.60**
S143	S143	0.76	0.71	0.70	0.22	0.45	0.56
S144	S144	0.67	0.61	0.59	0.21	0.39	0.48
S145	S145	0.64	0.57	0.56	0.20	0.38	0.47
S146	S146	0.73	0.68	0.67	0.23	0.46	0.56
S147	S147	**0.96**	**0.96**	**0.96**	0.17	0.38	0.52
S148	S148	**0.85**	**0.83**	**0.82**	0.21	0.45	0.59
S149	S149	**0.94**	**0.93**	**0.93**	0.18	0.41	0.56
S150	S150	**0.82**	0.79	0.79	0.22	0.47	**0.61**
S151	S151	**0.88**	**0.86**	**0.86**	0.21	0.46	**0.60**
S152	S152	**0.85**	**0.83**	**0.82**	0.23	0.48	**0.63**
S153	S153	0.77	0.74	0.73	0.22	0.45	0.56
S154	S154	**0.88**	**0.86**	**0.86**	0.19	0.41	0.55
S155	S155	0.61	0.53	0.52	0.20	0.37	0.44
S156	S156	**0.88**	**0.86**	**0.85**	0.21	0.46	**0.60**
S157	S157	**0.80**	0.77	0.76	0.23	0.48	**0.60**
S158	S158	0.76	0.72	0.71	0.22	0.45	0.56
S159	S159	**0.90**	**0.89**	**0.88**	0.20	0.44	0.59
S160	S160	0.77	0.74	0.73	0.22	0.45	0.57
S161	S161	**0.83**	**0.80**	0.79	0.19	0.40	0.52
S162	S162	0.78	0.74	0.73	0.23	0.47	0.59
S163	S163	0.76	0.72	0.72	0.21	0.44	0.55
S164	S164	0.68	0.63	0.61	0.22	0.42	0.52
S165	S165	**0.97**	**0.97**	**0.97**	0.16	0.35	0.48
S166	S166	**0.91**	**0.91**	**0.90**	0.20	0.44	**0.60**
S167	S167	**0.88**	**0.86**	**0.86**	0.19	0.41	0.54
S168	S168	0.58	0.51	0.49	0.18	0.33	0.40
S169	S169	0.75	0.70	0.69	0.21	0.43	0.54
S170	S170	**0.87**	**0.85**	**0.84**	0.21	0.44	0.58
S171	S171	**0.96**	**0.96**	**0.96**	0.16	0.37	0.50
S172	S172	**0.82**	0.79	0.79	0.22	0.47	**0.60**
S173	S173	0.72	0.67	0.66	0.22	0.44	0.55
S174	S174	**0.94**	**0.94**	**0.93**	0.18	0.40	0.55
S175	S175	**0.81**	0.78	0.77	0.20	0.41	0.53

Table 7. Average values of dilation and slip tendency for the low, moderate and high stress anisotropy ratios, denoted as S_{Hmax}/S_{hmin} equal to 1.5, 2.5, and 3.2, respectively, for PM Phase II structures (continued).

Faults	Symbol	Dilation Tendency			Slip Tendency		
		Low	Mod	High	Low	Mod	High
S176	S176	0.73	0.68	0.67	0.22	0.45	0.56
S177	S177	**0.84**	**0.81**	**0.80**	0.22	0.48	**0.62**
S178	S178	0.49	0.39	0.37	0.14	0.24	0.28
S179	S179	0.66	0.59	0.58	0.21	0.41	0.49
S180	S180	0.65	0.59	0.57	0.21	0.40	0.49
S181	S181	0.72	0.66	0.65	0.21	0.42	0.53
S182	S182	**0.82**	**0.80**	0.79	0.21	0.44	0.57
S183	S183	0.57	0.48	0.47	0.17	0.31	0.37
S184	S184	0.64	0.57	0.56	0.19	0.36	0.44
S185	S185	**0.88**	**0.86**	**0.86**	0.20	0.45	0.59
S186	S186	**0.95**	**0.94**	**0.94**	0.18	0.41	0.55
S187	S187	0.68	0.63	0.61	0.20	0.39	0.49
S188	S188	**0.95**	**0.95**	**0.95**	0.17	0.38	0.53
S189	S189	**0.96**	**0.96**	**0.96**	0.17	0.38	0.52
S190	S190	**0.95**	**0.94**	**0.94**	0.17	0.39	0.54
S191	S191	0.54	0.45	0.44	0.16	0.29	0.35
S192	S192	0.74	0.70	0.69	0.20	0.41	0.52
S193	S193	**0.80**	0.77	0.77	0.23	0.47	**0.60**
S194	S194	**0.87**	**0.85**	**0.85**	0.22	0.48	**0.63**
S195	S195	0.70	0.64	0.63	0.23	0.44	0.53
S196	S196	**0.90**	**0.89**	**0.89**	0.20	0.44	0.59
S197	S197	**0.91**	**0.89**	**0.89**	0.19	0.44	0.58
S198	S198	**0.91**	**0.90**	**0.89**	0.19	0.42	0.56
S199	S199	**0.95**	**0.95**	**0.95**	0.18	0.39	0.53
S200	S200	**0.88**	**0.87**	**0.86**	0.20	0.43	0.56
S201	S201	**0.95**	**0.94**	**0.94**	0.18	0.40	0.55
S202	S202	0.76	0.72	0.70	0.21	0.44	0.56
S203	S203	**0.88**	**0.86**	**0.85**	0.20	0.44	0.58
S204	S204	**0.95**	**0.95**	**0.95**	0.17	0.39	0.53
S205	S205	0.71	0.66	0.65	0.22	0.43	0.54
S206	S206	0.56	0.48	0.46	0.18	0.32	0.38
S207	S207	**0.95**	0.95	0.95	0.17	0.38	0.52
S208	S208	**0.88**	**0.87**	**0.87**	0.21	0.45	0.59
S209	S209	**0.88**	**0.86**	**0.86**	0.20	0.43	0.56
S210	S210	0.63	0.57	0.55	0.18	0.33	0.41
S211	S211	0.47	0.37	0.35	0.11	0.19	0.22
S212	S212	**0.82**	0.79	0.78	0.22	0.47	**0.60**

Table 7. Average values of dilation and slip tendency for the low, moderate and high stress anisotropy ratios, denoted as S_{Hmax}/S_{hmin} equal to 1.5, 2.5, and 3.2, respectively, for PM Phase II structures (continued).

Faults	Symbol	Dilation Tendency			Slip Tendency		
		Low	Mod	High	Low	Mod	High
S213	S213	0.43	0.32	0.29	0.10	0.16	0.17
S214	S214	0.71	0.66	0.65	0.22	0.43	0.54
S215	S215	0.51	0.41	0.40	0.15	0.27	0.31
S216	S216	**0.85**	**0.82**	**0.82**	0.22	0.48	**0.62**
S217	S217	0.60	0.52	0.51	0.20	0.36	0.43
S218	S218	**0.81**	0.78	0.77	0.23	0.49	**0.62**
S219	S219	**0.86**	**0.83**	**0.83**	0.21	0.46	0.59
S220	S220	0.41	0.30	0.28	0.08	0.11	0.12
S221	S221	0.77	0.73	0.73	0.22	0.44	0.56
S222	S222	0.51	0.41	0.39	0.14	0.25	0.29
S223	S223	**0.85**	**0.82**	**0.82**	0.21	0.46	0.59
S224	S224	0.73	0.69	0.67	0.22	0.44	0.55
S225	S225	**0.86**	**0.85**	**0.84**	0.21	0.44	0.58
S226	S226	0.40	0.29	0.27	0.06	0.09	0.11
S227	S227	0.58	0.50	0.48	0.18	0.33	0.39
S228	S228	0.44	0.33	0.31	0.10	0.16	0.18
S229	S229	0.45	0.35	0.33	0.12	0.20	0.22
S230	S230	0.51	0.42	0.40	0.16	0.28	0.32
S231	S231	0.71	0.66	0.65	0.22	0.44	0.54
S232	S232	0.68	0.62	0.61	0.22	0.43	0.52
S233	S233	0.41	0.31	0.28	0.08	0.11	0.13
S234	S234	**0.94**	**0.94**	**0.94**	0.18	0.40	0.54
S235	S235	**0.80**	0.77	0.76	0.23	0.49	**0.62**
S236	S236	**0.94**	**0.93**	**0.92**	0.19	0.42	0.57
S237	S237	0.53	0.44	0.42	0.15	0.28	0.32
S238	S238	0.48	0.38	0.36	0.13	0.22	0.25
S239	S239	**0.80**	0.77	0.76	0.23	0.48	**0.61**
S240	S240	0.48	0.38	0.36	0.12	0.21	0.24
S241	S241	0.69	0.63	0.62	0.22	0.44	0.53
S242	S242	0.70	0.64	0.63	0.23	0.44	0.54
S243	S243	0.58	0.50	0.48	0.18	0.32	0.39
S244	S244	0.43	0.33	0.30	0.10	0.17	0.19
S245	S245	0.69	0.64	0.62	0.21	0.41	0.51
S246	S246	**0.95**	**0.94**	**0.94**	0.18	0.40	0.55
S247	S247	**0.97**	**0.97**	**0.97**	0.16	0.35	0.48
S248	S248	**0.94**	**0.92**	**0.92**	0.19	0.42	0.57
S249	S249	**0.95**	**0.95**	**0.95**	0.17	0.38	0.53

Table 7. Average values of dilation and slip tendency for the low, moderate and high stress anisotropy ratios, denoted as S_{Hmax}/S_{hmin} equal to 1.5, 2.5, and 3.2, respectively, for PM Phase II structures (continued).

Faults	Symbol	Dilation Tendency			Slip Tendency		
		Low	Mod	High	Low	Mod	High
S250	S250	0.56	0.48	0.46	0.17	0.32	0.37
S251	S251	**0.86**	**0.84**	**0.83**	0.21	0.45	0.59
S252	S252	0.56	0.49	0.47	0.18	0.32	0.38
S253	S253	0.49	0.40	0.38	0.15	0.25	0.29
S254	S254	0.66	0.59	0.58	0.22	0.42	0.50
S255	S255	0.50	0.40	0.38	0.15	0.26	0.30
S256	S256	0.79	0.76	0.75	0.22	0.46	0.58
S257	S257	0.77	0.73	0.72	0.22	0.45	0.56
S258	S258	0.58	0.50	0.48	0.13	0.24	0.30
S259	S259	0.86	0.84	0.83	0.21	0.45	0.59
S260	S260	0.47	0.38	0.35	0.12	0.20	0.23
S261	S261	0.70	0.65	0.64	0.23	0.44	0.54
S262	S262	0.40	0.29	0.26	0.06	0.09	0.10
S263	S263	0.75	0.71	0.70	0.20	0.40	0.50
S264	S264	**0.94**	**0.94**	**0.93**	0.18	0.41	0.56
S265	S265	**0.88**	**0.87**	**0.87**	0.20	0.44	0.58
S266	S266	**0.94**	**0.94**	**0.94**	0.18	0.41	0.55
S267	S267	**0.86**	**0.84**	**0.83**	0.20	0.41	0.54
S268	S268	**0.86**	**0.84**	**0.83**	0.20	0.41	0.54
S269	S269	**0.81**	0.78	0.77	0.22	0.45	0.57
S270	S270	**0.91**	**0.90**	**0.90**	0.20	0.46	**0.61**
S271	S271	0.76	0.73	0.72	0.23	0.47	0.59
S272	S272	**0.90**	**0.89**	**0.88**	0.21	0.47	**0.63**
S273	S273	**0.80**	0.77	0.76	0.20	0.43	0.55
S274	S274	**0.87**	**0.85**	**0.84**	0.22	0.46	**0.61**
S275	S275	**0.84**	**0.82**	**0.81**	0.23	0.48	**0.62**
S276	S276	**0.82**	0.79	0.78	0.23	0.49	**0.63**
S277	S277	0.74	0.69	0.68	0.23	0.47	0.58
S278	S278	**0.84**	**0.81**	**0.80**	0.21	0.45	0.58
S279	S279	0.67	0.61	0.60	0.22	0.42	0.51
S280	S280	0.76	0.71	0.70	0.23	0.46	0.57
S281	S281	**0.91**	**0.89**	**0.89**	0.20	0.43	0.58
S282	S282	**0.83**	**0.80**	0.79	0.22	0.47	**0.61**
S283	S283	0.72	0.68	0.66	0.23	0.45	0.56
S284	S284	0.63	0.56	0.55	0.21	0.39	0.47
S285	S285	**0.87**	**0.85**	**0.85**	0.22	0.48	**0.63**
S286	S286	0.55	0.47	0.45	0.17	0.30	0.36

Table 7. Average values of dilation and slip tendency for the low, moderate and high stress anisotropy ratios, denoted as S_{Hmax}/S_{hmin} equal to 1.5, 2.5, and 3.2, respectively, for PM Phase II structures (continued).

Faults	**Symbol**	**Dilation Tendency**			**Slip Tendency**		
		Low	**Mod**	**High**	**Low**	**Mod**	**High**
S287	S287	0.70	0.65	0.63	0.22	0.43	0.53
S288	S288	0.65	0.58	0.57	0.22	0.41	0.49
S289	S289	0.47	0.37	0.35	0.13	0.22	0.25
S290	S290	0.58	0.50	0.48	0.19	0.35	0.41
S291	S291	0.56	0.48	0.46	0.18	0.33	0.38
S292	S292	0.79	0.75	0.74	0.23	0.48	**0.60**
S293	S293	0.55	0.48	0.46	0.18	0.32	0.38
S294	S294	0.70	0.64	0.63	0.22	0.43	0.52
S295	S295	0.40	0.28	0.26	0.06	0.08	0.08
S296	S296	**0.91**	**0.90**	**0.89**	0.19	0.41	0.55
S297	S297	**0.88**	**0.86**	**0.85**	0.21	0.46	**0.61**
S298	S298	**0.84**	**0.82**	**0.81**	0.22	0.48	**0.62**
S299	S299	**0.87**	**0.84**	**0.84**	0.21	0.46	**0.61**
S300	S300	**0.86**	**0.83**	**0.83**	0.21	0.45	0.58
S301	S301	**0.84**	**0.82**	**0.81**	0.23	0.48	**0.62**
S302	S302	0.70	0.65	0.64	0.23	0.44	0.55
S303	S303	**0.90**	**0.89**	**0.89**	0.21	0.46	**0.62**
S304	S304	**0.82**	0.78	0.78	0.22	0.46	0.59
S305	S305	**0.82**	0.78	0.77	0.22	0.46	0.58
S306	S306	0.73	0.68	0.66	0.20	0.41	0.51
S307	S307	**0.91**	**0.89**	**0.89**	0.19	0.42	0.57
S308	S308	0.69	0.63	0.62	0.22	0.43	0.52
S309	S309	**0.84**	**0.81**	**0.81**	0.21	0.45	0.58
S310	S310	**0.80**	0.77	0.76	0.22	0.46	0.58
S311	S311	0.69	0.64	0.62	0.22	0.44	0.53
S312	S312	**0.97**	**0.97**	**0.97**	0.16	0.36	0.49
S313	S313	0.79	0.76	0.75	0.23	0.48	**0.61**
S314	S314	0.76	0.73	0.72	0.22	0.45	0.57
S315	S315	**0.86**	**0.84**	**0.84**	0.21	0.46	**0.60**

ANALYSIS OF HYDRAULIC TESTS

Detailed borehole inflow analyses were conducted over screened intervals by Oberlander *et al.* (2002) for wells ER-EC-1, ER-EC-2a, ER-EC-4, ER-EC-5, ER-EC-6, ER-EC-7, and ER-EC-8. Borehole geophysical surveys were also conducted along selected intervals of these boreholes to identify the occurrence and orientation of fractures, and to discern if the fractures are open or closed. Analysis of discrete borehole inflows relative to values of dilation and slip tendency of adjacent fractures is intended to assess the influence of the stress field on local-scale fracture flow to these boreholes. Unlike the major faults studied in Section 3, fractures intersecting these wells are considerably smaller and may consist of faults with unknown, but assumed small displacement, and joints of either tectonic or cooling (i.e., volumetric contraction) origin. Significant flow through these smaller background fractures is reliant on a network comprised of other conductive fractures (e.g., Reeves *et al.* [2013, 2014]), with network connectively serving as much or possibly more of a role on fractures transmitting significant quantities of fluid to a borehole than the orientation the fracture within the stress field.

Borehole Fracture Orientation

A total of 294 fractures were logged in boreholes ER-EC-1 (n = 93, 32 percent), ER-EC-2a (n = 25, 8 percent), ER-EC-4 (n = 46, 16 percent), ER-EC-5 (n = 35, 12 percent), ER-EC-6 (n = 36, 12 percent), ER-EC-7 (n = 15, 5 percent), and ER-EC-8 (n = 44, 15 percent). The borehole fracture logging did not span the entire borehole and appeared to target specific hydrostratigraphic-stratigraphic units. Apparent fracture intensity estimates for ER-EC-1, ER-EC-2a, ER-EC-4, ER-EC-5, ER-EC-6, ER-EC-7, and ER-EC-8 range from 0.02 to 0.12 fractures per meter, corresponding to an average apparent vertical fracture spacing of 8 m to 42 m. These apparent intensity and vertical spacing values are generally informative in that only 294 fractures were encountered in a 4.4 km of combined borehole surveys. However, some of the stratigraphic units are more prone to fracturing than others (e.g., welded tuff units on average tend to be more fractured than nonwelded tuff) and these bulk averages do not take lithology into account. In addition, steeply dipping fractures will always be under-represented in vertical boreholes because of the low probability of intersection (Terzaghi, 1965).

The small number of logged fractures precludes cluster analysis to identify dominant fracture set orientations for each of the boreholes. Instead, a combined dataset is used to understand how representative these smaller background fractures are relative to the large-scale faults included in dilation and slip tendency analyses in Section 3. The lower-hemisphere equal-area plots shown in Figure 34 show a broad N-S distribution in fracture strike with two fracture set orientations trending approximately NW-SE and NE-SW (denoted by the two clusters in Figure 34b). Recall that a southern hemisphere projection of planes to poles results in a $3\pi/2$ clockwise rotation. Both clusters have an average dip of approximately 70°, which is approximately 13 percent less steep than the universally applied 80° to all large-scale faults in Figure 12.

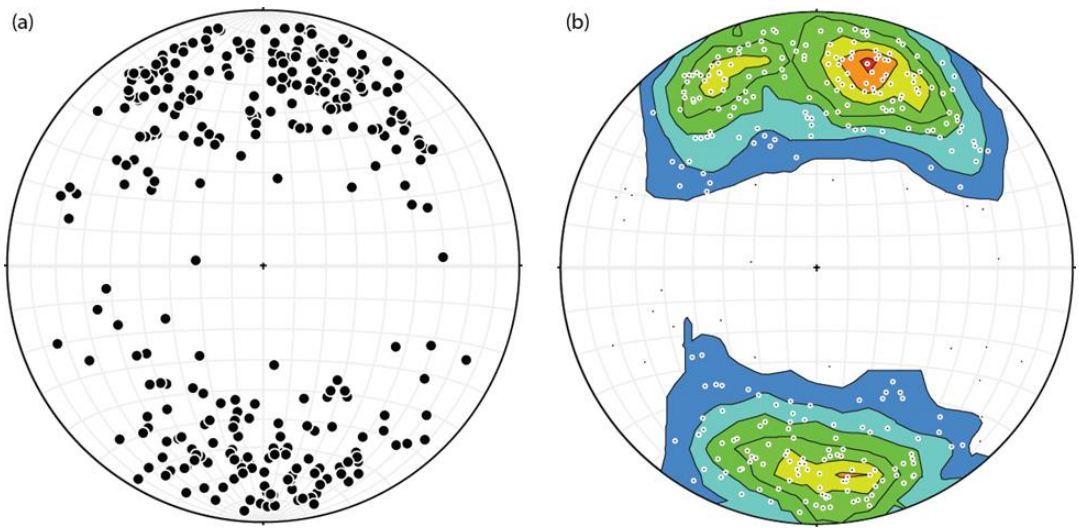

Figure 34. (a) Southern-hemisphere, equal-area projection of all fracture planes logged in boreholes ER-EC-1, ER-EC-2A, ER-EC4, ER-EC-5, ER-EC-6, ER-EC-7 and ER-EC-8 wells to poles and (b) contours of poles to planes.

The lack of distinction in dip, and often dip direction, for faults and structures in Figure 12 combined from NSTec (2014) and Slate *et al.* (1999) does not allow for stereonet projection of the 15,625 fault segments for direct comparison to background fracture orientations. Visual inspection of the combined fault map in Figure 12 does suggest that the background fractures detected in the ER-EC wells appear to have a larger NW-SE component of fracture strike than the large-scale faults. However, this is difficult to discern without a direct comparison.

Dilation and slip tendency calculations were conducted on all of the 294 fracture planes for the three horizontal stress anisotropy ratios used in Section 3, given both average and nearest focal mechanism stress fields (Figures 35 through 37). The nearest SATSI stress inversion solutions for the seven ER-EC boreholes indicate a S_{Hmax} direction of N34°E to N47°E with an average of N40°E. This is consistent with the S_{Hmax} direction of N42°E averaged over all of Pahute Mesa. The small deviation in horizontal stress directions in the vicinity of the ER-EC wells yields RMSD values that are, in general, less than five percent for both dilation and slip tendency. Similar to the strategy employed in Section 3, final dilation and slip tendency values represent the average of the two horizontal stress approaches. Values for dilation and slip tendency for all 294 background fractures for each of the ER-EC wells are located in Tables D-2 through D-8 in Appendix D. Fractures identified for enhanced flow, based solely on dilation tendency, are bolded in Tables D-2 through D-8. Note that background fractures are only critically stressed ($T_s \geq 0.6$) in the highly unlikely scenario where the horizontal stress anisotropy ratio of S_{Hmax}/S_{hmin} is equal to 3.2.

Dilation tendency values for the background fractures are highly variable and range from 0.09 to 0.98, with the lowest values assigned to gently dipping fractures oriented along S_{hmin} and the highest values assigned to steeply dipping fractures oriented along S_{Hmax} (Figures 35 through 37). This is consistent with major fault dilation tendency trends for the major faults, except for the greater variation in fault dips for the background fractures

changes the distribution of dilation and slip tendency values (Figures 38 and 39), where more gently dipping fractures produce lower dilation tendency values and, in general, greater slip tendency values when dips are closer to the ideal range of 45-55° (Figures 35 through 37). Similar to the results of the major faults, none of the background fractures are critically stressed when S_{Hmax}/S_{hmin} = 2.5. Therefore, identification of background fractures that may be enhanced for flow is solely based on values of dilation tendency.

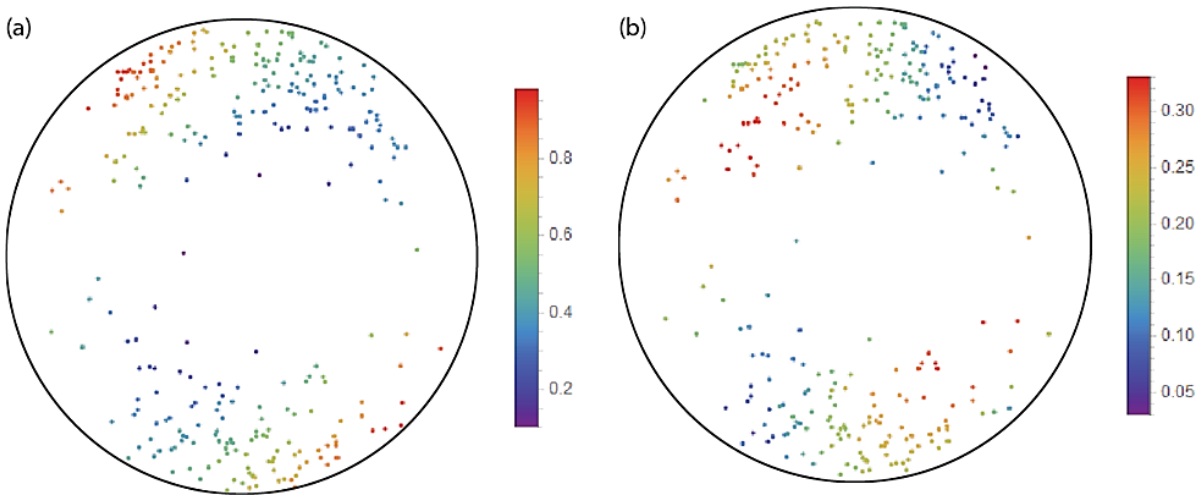

Figure 35. Southern-hemisphere, equal-area projection of all fracture planes logged in boreholes ER-EC-1, ER-EC-2A, ER-EC4, ER-EC-5, ER-EC-6, ER-EC-7 and ER-EC-8 wells to poles with (a) dilation and (b) slip tendency values for S_{Hmax}/S_{hmin} = 1.5. Horizontal stress directions determined from SATSI stress inversion solution nearest to each borehole.

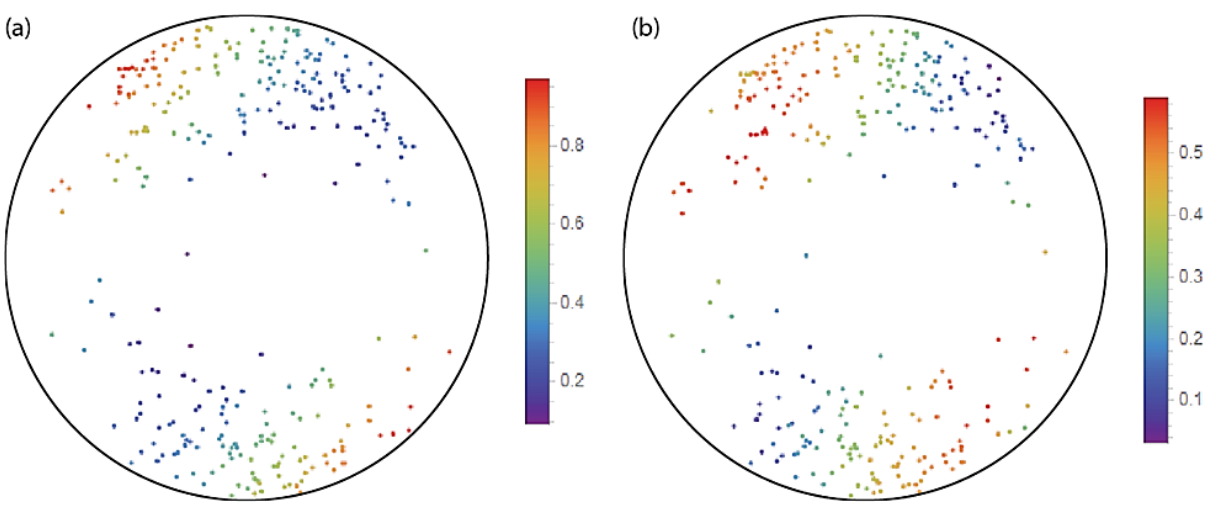

Figure 36. Southern-hemisphere, equal-area projection of all fracture planes logged in boreholes ER-EC-1, ER-EC-2A, ER-EC4, ER-EC-5, ER-EC-6, ER-EC-7 and ER-EC-8 wells to poles with (a) dilation and (b) slip tendency values for S_{Hmax}/S_{hmin} = 2.5. Horizontal stress directions determined from SATSI stress inversion solution nearest to each borehole.

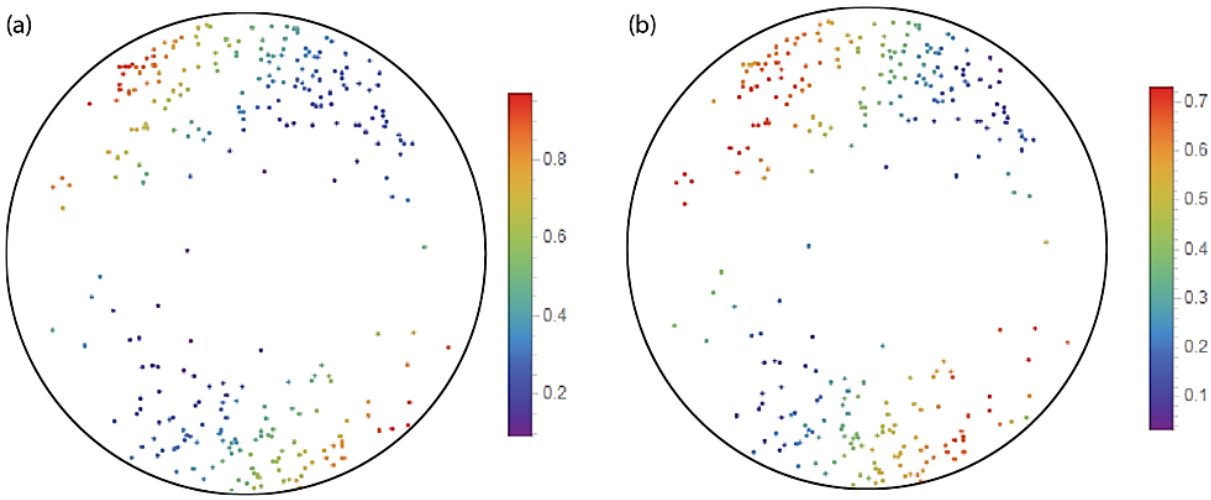

Figure 37. Southern-hemisphere, equal-area projection of all fracture planes logged in boreholes ER-EC-1, ER-EC-2A, ER-EC4, ER-EC-5, ER-EC-6, ER-EC-7 and ER-EC-8 wells to poles with (a) dilation and (b) slip tendency values for S_{Hmax}/S_{hmin} = 3.2. Horizontal stress directions determined from SATSI stress inversion solution nearest to each borehole.

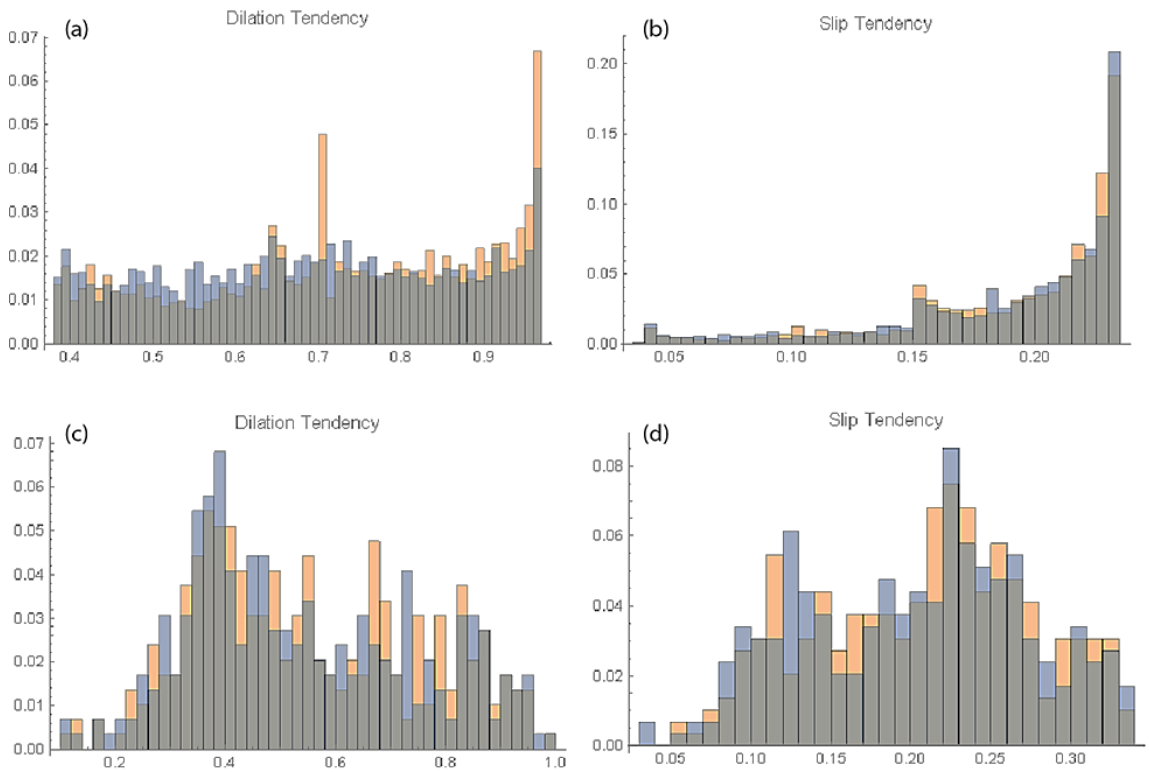

Figure 38. Histogram of (a) dilation tendency values and (b) slip tendency values, respectively, for all large-scale faults and structures shown in Figure 12, and (c) dilation and (d) slip tendency values for all borehole fractures, respectively for S_{Hmax}/S_{hmin} = 1.5. Values computed using constant and spatially variable (nearest borehole in c and d) are denoted using tan and blue colors, respectively. Overlap is shown in gray.

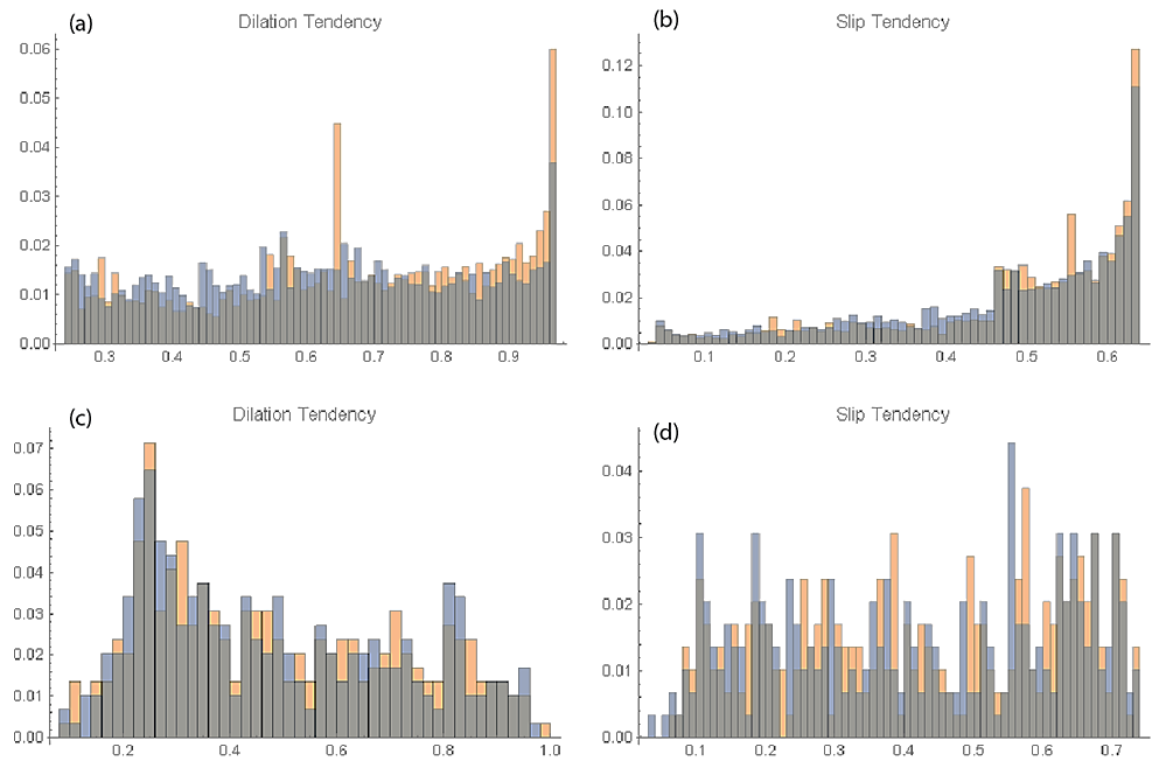

Figure 39. Histogram of (a) dilation tendency values and (b) slip tendency values, respectively, for all large-scale faults and structures shown in Figure 12, and (c) dilation and (d) slip tendency values for all borehole fractures, respectively for S_{Hmax}/S_{hmin} = 3.2. Values computed using constant and spatially variable (nearest borehole in c and d) are denoted using tan and blue colors, respectively. Overlap is shown in gray.

The number of dilated fractures computed for each borehole is presented in Table 8 and is highly variable, ranging from 7 percent to 40 percent of the total fracture population. An average of 20 percent dilated fractures detected over all of the boreholes is approximately half of the 40 percent average computed for the large-scale faults in Section 3.3. This is consistent with the trends shown in Figures 35 through 39 and indicates a significantly higher occurrence of background fractures with less optimal strike and dip than the regional structures. Therefore, the background fractures are only marginally representative of the larger faults and geologic structures in Figure 12.

Table 8. Number of dilated fractures computed for each borehole.

Well	Dilated Fractures	Total Fractures	Dilated (%)
ER-EC-1	13	93	14
ER-EC-2A	6	25	24
ER-EC-4	3	46	7
ER-EC-5	12	35	34
ER-EC-6	7	36	19
ER-EC-7	6	15	40
ER-EC-8	8	44	18
Summary	55	294	19

Borehole Inflow Responses

Oberlander *et al.* (2002) conducted detailed borehole inflow logging for wells ER-EC-1A, ER-EC-2A, ER-EC4, ER-EC-5, ER-EC-6, ER-EC-7 and ER-EC-8 using small diameter flowmeters. Hydraulic conductivity for discrete inflow locations along screened well intervals was estimated using the methodology of Rehfeldt *et al.* (1989):

$$K_i = \frac{\hat{q}_i - q_i}{2B_i\left(\hat{h}_i - h_i\right)} \ln \frac{R_a}{r_o} \tag{10}$$

where K_i is hydraulic conductivity of interval i, $\hat{q}_i$ is flux for interval i under ambient, nonpumping conditions, q_i is flux for interval i during pumping, B_i is interval thickness, $\hat{h}_i$ is pressure head at interval i under ambient conditions, h_i is pressure head at interval i under pumping conditions, R_a is effective hydraulic radius during pumping, and r_o is filter pack radius. The apparent radius of influence is computed using Rehfeldt *et al.* (1989):

$$R_a = \sqrt{\frac{Kbt}{S}} \tag{11}$$

where K is depth-averaged hydraulic conductivity, b is saturated thickness contributing to flow, t elapsed time since pumping began and S is formation storativity (estimated at 0.001).

Flow rates $\hat{q}_i$ and q_i across each interval were measured by trolling a flowmeter up and down the borehole during ambient and pumping conditions while taking flow measurements in increments of 6.1 cm (0.2 ft). A low rate flowmeter was used for ambient conditions. The pumping surveys consisted of three different pumping rates representing the maximum, minimum and intermediate pump capacity. Ambient formation pressures are estimated at each flow measurement point according to the height of the fluid column above the measurement point and temperature-dependent variations in fluid density and compressibility. Estimation of formation pressures during pumping conditions accounted for the factors listed above for ambient conditions as well as the additional influences of drawdown, frictional loss along the well casing, the vertical velocity head component of the Bernoulli equation, and pressure loss through the gravel pack and well screen. Additional detail on the estimation of formation pressures is provided in Oberlander *et al.* (2002).

One of the primary assumptions of this method is that flow is perfectly horizontal across the screened interval. Differences in the flow rates for each survey correspond to either inflow to or outflow from the well. The calculation of hydraulic conductivity with depth in the wells according to Equation (10) necessitated spatial averaging of the flow measurements over an interval of 61 cm (2 ft) over the screened sections to reduce the effects of small-scale variations caused by instrument noise, flow turbulence and/or irregular alignment of the borehole flowmeter in the well. Flow measurements were averaged over an interval of 6.1 m (20 ft) along cased sections of the well. Final hydraulic conductivity values assigned to each interval represent the average values of K_i computed for each of the three pumping rates.

A systematic pattern of inflows, with respect to either depth or geology, was not observed for the ER-EC wells analyzed, with each well exhibiting a unique response to pumping. The inflow responses for each of the three screened intervals, denoted as upper, middle and lower, are variable and were placed into three groups by Oberlander *et al.* (2002): (1) no inflow, (2) diffusive inflows characteristic of a densely fractured media with many conductive fractures, and (3) sharp inflows characteristic of a few, high-capacity fractures. The most systematic observation is that the lower screened interval contributed insignificant inflows for all wells, except for ER-EC-6 where the lower screened interval contributed a minor amount of inflow.

A brief synopsis of the pumping flow rate trends along with estimated hydraulic conductivity are provided below for ER-EC-1, ER-EC-2a, ER-EC-4, ER-EC-5, ER-EC-6 and ER-EC-8 (Figures 40 through 45). ER-EC-7 is not included because of an observed flow diversion within the well that contributed to anomalous flow responses. The following synopses for each well were extracted from the major observations given by Oberlander *et al.* (2002) and interpretation of borehole lithologic logs.

ER-EC-1

Nearly all the groundwater inflow occurs in screen joints 1 through 4 (700 to 768 m bls) of the upper screened section with sharp increases in flow suggestive of a few, highly conductive fractures (Figure 40). The middle (1,020 to 1,150 m bls) and lower screened (1,350 to 1,430 m bls) intervals do not significantly contribute to borehole inflow. Lithology of the top screened interval is a rhyolitic lava. The middle and lower intervals contain predominately bedded tuffs with thin moderately welded units, and vitric and pumiceous lava with flow breccia, respectively.

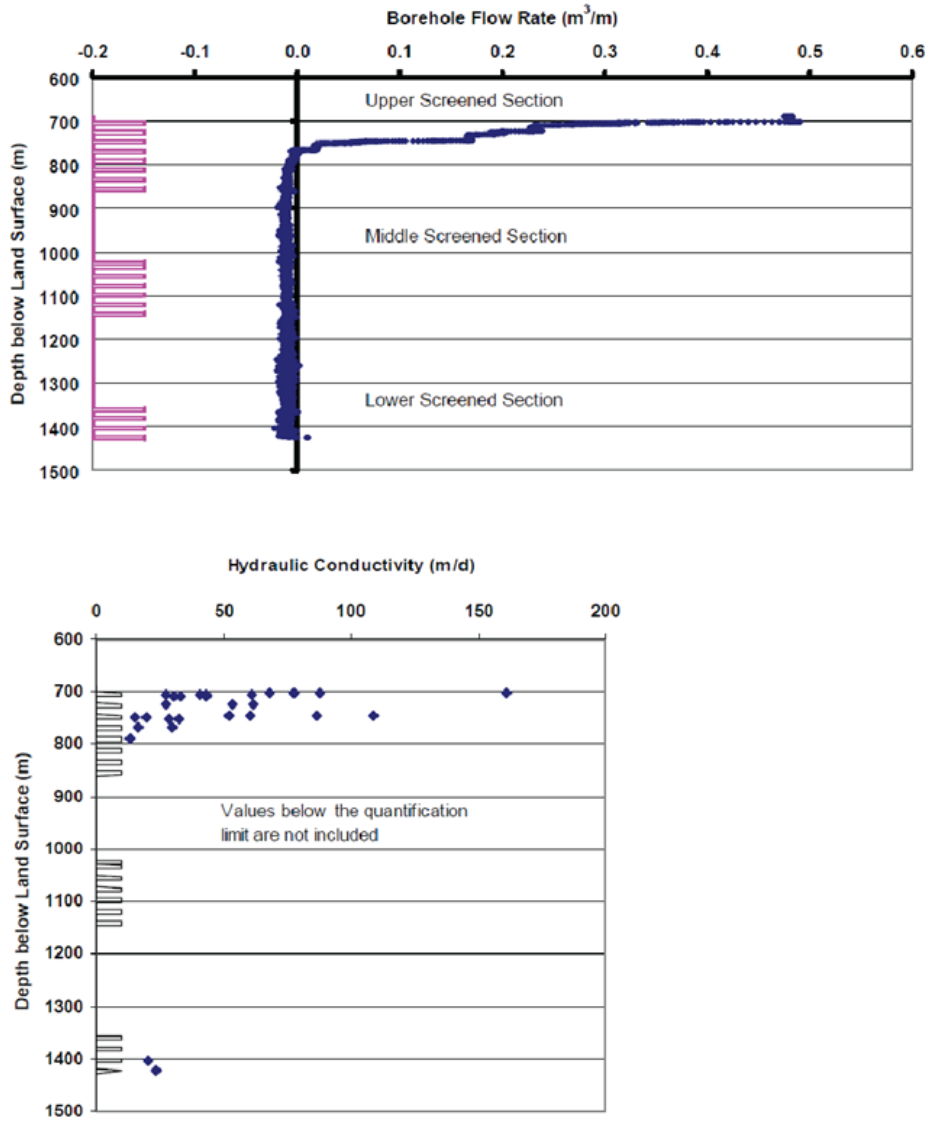

Figure 40. ER-EC-1 borehole inflow rates during pumping at 0.48 m^3/min (top), and resultant distribution of hydraulic conductivity along borehole derived from Rehfeldt *et al.* (1989) approach (bottom). From Oberlander *et al.* (2002).

ER-EC-2A

Nearly all groundwater inflow occurs over the upper (510 to 660 m bls) and middle screened sections (940 to 1,060 m bls), with the upper screened section exhibiting characteristics of a densely fractured media and the middle section at approximately at 960 m bls response indicative of a few, high-capacity fractures (Figure 41). The lower section (1,370 to 1,480 m bls) does not significantly contribute to flow. The upper section is comprised of nonwelded tuff, the middle section contains nonwelded tuff with the sharp inflow corresponding to reworked tuff (tuffaceous sediments that have been disturbed and redeposited through surface water processes), and the lower section is predominately nonwelded tuff with a minor component of moderately welded units.

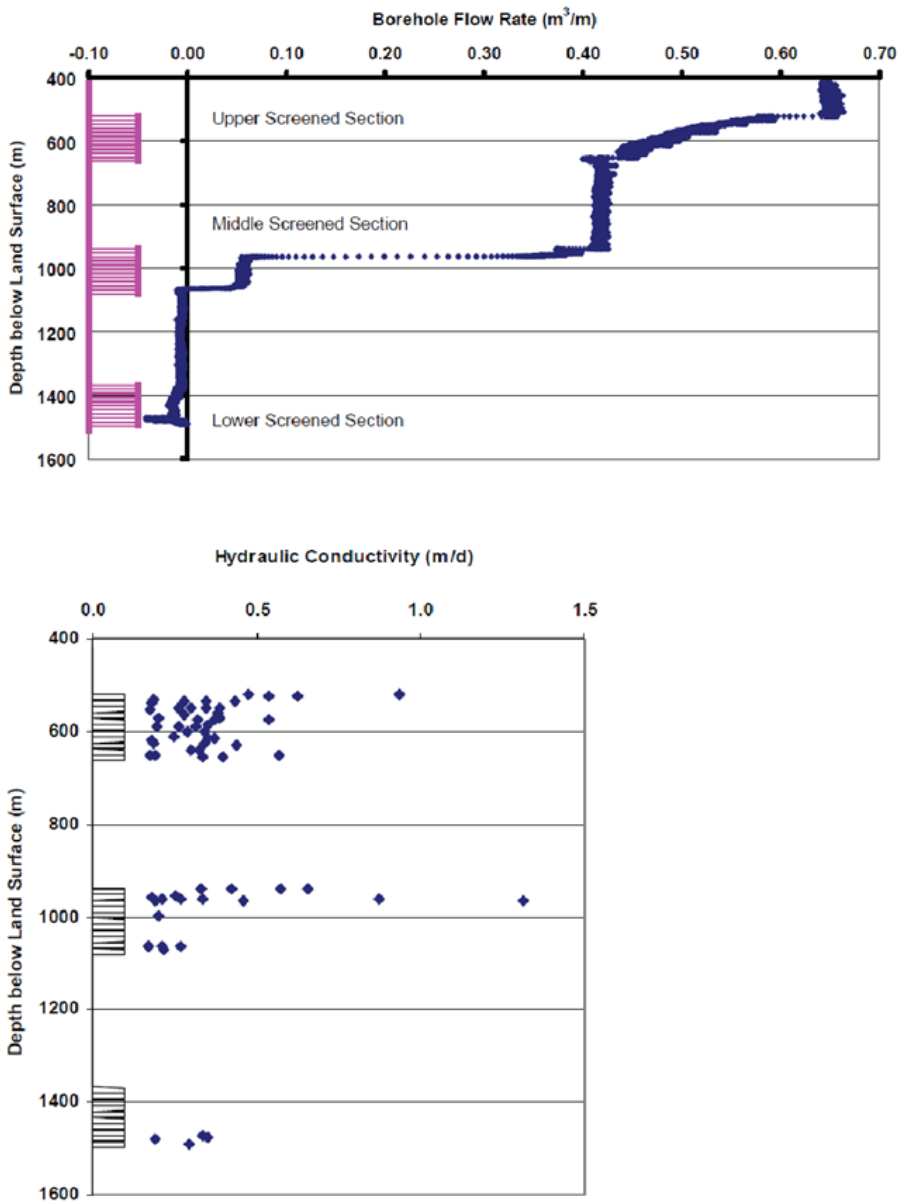

Figure 41. ER-EC-2A borehole inflow rates during pumping at 0.65 m^3/min (top), and resultant distribution of hydraulic conductivity along borehole derived from Rehfeldt *et al.* (1989) approach (bottom). From Oberlander *et al.* (2002).

ER-EC-4

Borehole inflows are entirely from the upper three screen joints (300 to 375 m bls) of the upper screened section, with no flow contributions for the middle (580 to 690 m bls) and lower (945 to 1,035 m bls) screened sections (Figure 42). The upper zone is comprised of lava with minor colluvium, and the middle and lower sections are comprised of various assemblages of nonwelded and partially and moderately welded tuff units.

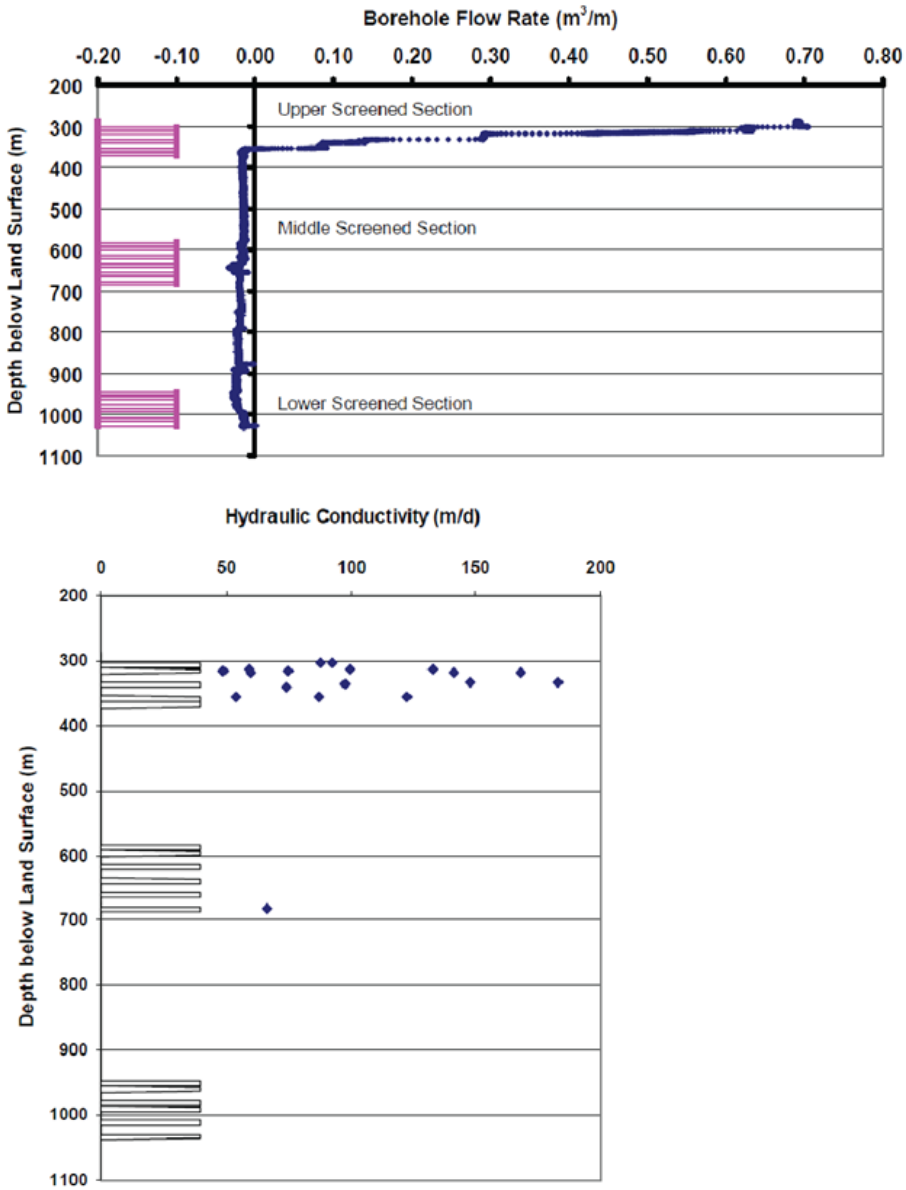

Figure 42. ER-EC-4 borehole inflow rates during pumping at 0.70 m^3/min (top), and resultant distribution of hydraulic conductivity along borehole derived from Rehfeldt *et al.* (1989) approach (bottom). From Oberlander *et al.* (2002).

ER-EC-5

The upper (365 to 425 m bls) and middle (575 to 640 m bls) screened sections contribute nearly all inflow to well, with the lower screened section (685 to 735 m bls) contributing minor inflows (Figure 43). The middle section response is indicative of a few, high-capacity fractures, with more diffusive inflow gains in the upper section characteristic of a densely fractured medium. The upper and middle sections are comprised entirely of moderately welded tuff, and the bottom section is a combination of moderately welded and densely welded tuff units.

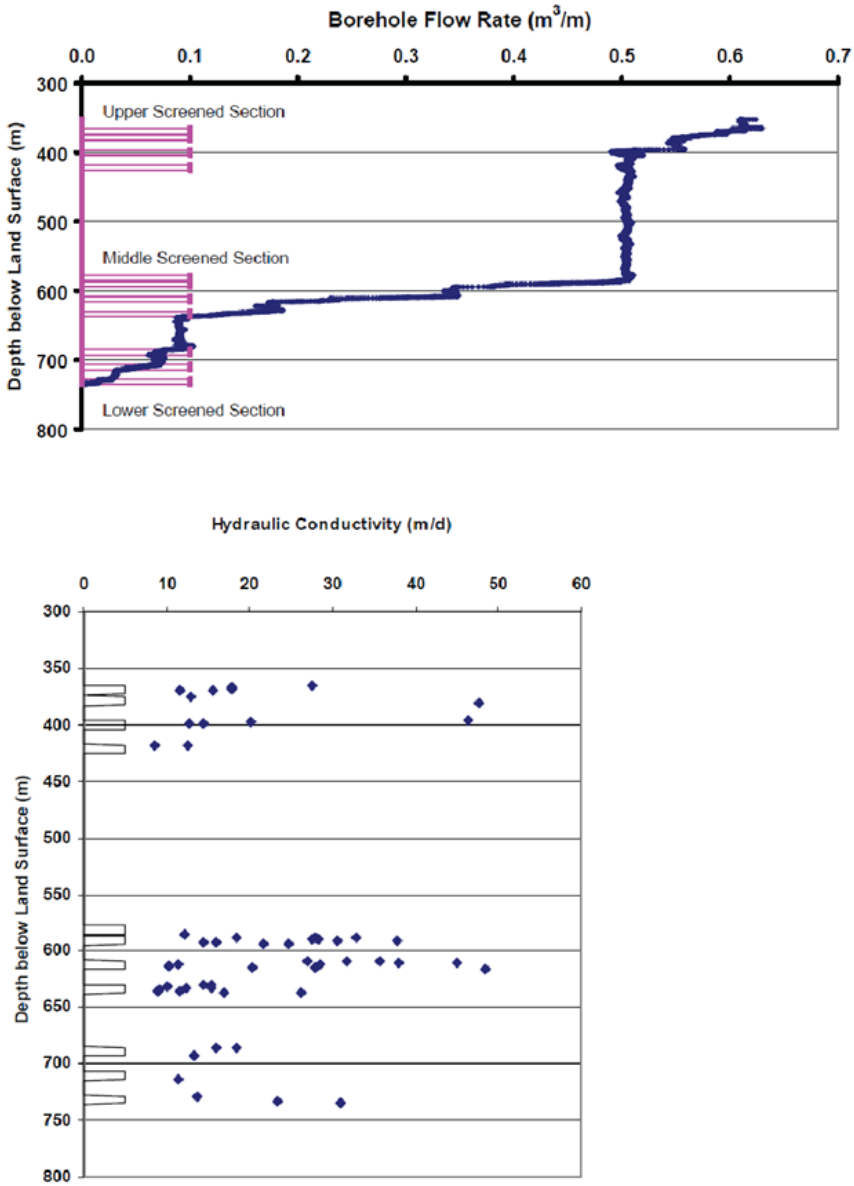

Figure 43. ER-EC-5 borehole inflow rates during pumping at 0.61 m^3/min (top), and resultant distribution of hydraulic conductivity along borehole derived from Rehfeldt *et al.* (1989) approach (bottom). From Oberlander *et al.* (2002).

ER-EC-6

Nearly all inflow occurs in the first three screen joints in the upper screened section (495 to 570 m bls), with the upper screen joint (495 to 505 m bls) exhibiting an inflow responses characteristic of a few, high-capacity fractures (Figure 44). Insignificant inflows are observed for the middle (670 to 760 m bls) and lower (1,045 to 1,160 m bls) screened intervals. The upper section is comprised entirely of rhyolitic lava, middle and lower sections are primarily nonwelded tuff with some partially and moderately welded units.

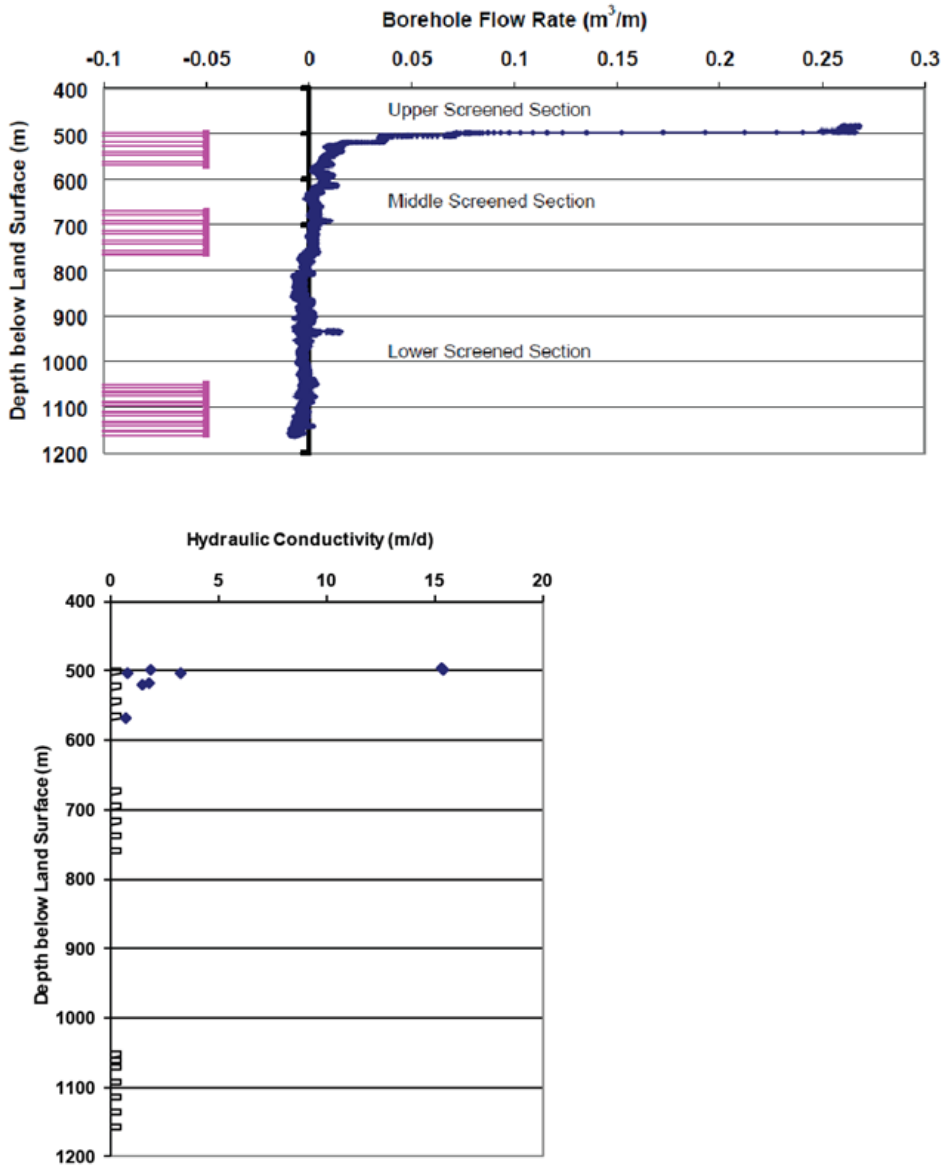

Figure 44. ER-EC-6 borehole inflow rates during pumping at 0.48 m^3/min (top), and resultant distribution of hydraulic conductivity along borehole derived from Rehfeldt *et al.* (1989) approach (bottom). From Oberlander *et al.* (2002).

ER-EC-8

Nearly all ground water inflow occurs through screen joints 1 and 3 (205 to 245 m bls) in the upper (205 to 300 m bls) screened section, with insignificant inflow through the middle (440 to 460 m bls) and lower (510 to 540 m bls) screened sections (Figure 45). The upper and lower screened sections are comprised of nonwelded tuffs, and the middle section is partially and moderately welded tuff.

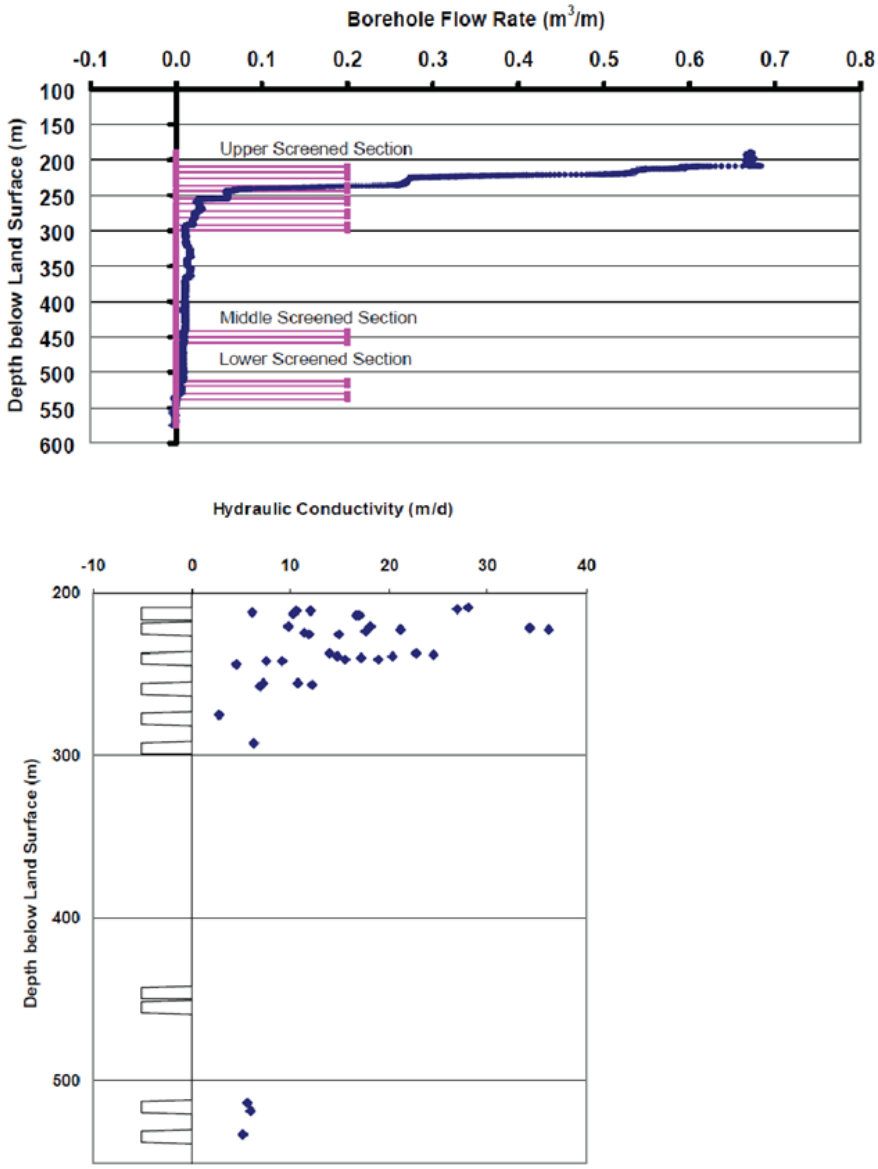

Figure 45. ER-EC-8 borehole inflow rates during pumping at 0.67 m^3/min (top), and resultant distribution of hydraulic conductivity along borehole derived from Rehfeldt *et al.* (1989) approach (bottom). From Oberlander *et al.* (2002).

Correspondence between Borehole Inflow Tends and Fractures

The borehole inflow trends in Section 4.2 are analyzed for the presence or absence of fractures, presences or absence of fractures oriented optimally within the stress field for fluid flow, and lithology. Fractures oriented optimally within the stress field for enhanced fluid flow are categorized as dilated, whereas faults not optimally oriented for fluid are categorized as nondilated. The steeply dipping nature of borehole fractures and ER-EC 0.31 m (12.25 in) borehole diameter leads to instances where fractures originally intersecting one side of a

borehole slightly outside of a screened interval may actually contribute to inflow within a screened interval. The vertical distance or height H along the well bore at which a fracture may intersect a screened interval is given by:

$$H = \tan\left(\frac{\phi}{2r_b}\right) \tag{12}$$

where ϕ is fracture dip and r_b is borehole radius. Values of H in the fracture data range from 0.1 m for fractures with 20° dip to approximately 4 m for fractures with 85° dip. Given that steeply dipping fractures aligned in the direction of S_{Hmax} have the highest values of dilation tendency, values of H are used to determine if dilated fractures located slightly away from either screened intervals or locations of sharp inflow should be included in the inflow trend analysis.

Inflow responses for all screened intervals are divided into three groups to discern the correspondence between inflow trends and fractures: sharp inflow, diffuse inflow and no inflow (Table 9). This differs slightly from the Oberlander *et al.* (2002) categories: few, highly conductive fractures, densely fractured medium and insignificant flow; and is more applicable for this analysis which seeks to correlate sharp increases in inflow with fractures. A total of 6 screened intervals, ER-EC-1 upper, ER-EC-2A middle, ER-EC-4 upper, ER-EC-5 middle, ER-EC-6 upper and ER-EC-8 upper, exhibited responses with sharp inflows (Table 9). Fractures are present for all cases of sharp inflow, and thus, sharp inflows are assumed to be correlated with conductive fractures and the filter pack surrounding the well screen does not significantly dampen the inflow response from discrete fractures. In several cases, more than one fracture is located within the approximate location of the sharp inflow zone, and these fractures are included on the basis of values of H defined in Equation (12). The inclusion of adjacent fractures that may or may not be responsible for sharp inflow responses may slightly over-estimate the number of conductive fractures. A total of 25 conductive fractures contributing to sharp inflows were identified: lithology, orientation, dilation tendency (S_{Hmax}/S_{hmin} = 1.5), and slip tendency (S_{Hmax}/S_{hmin} = 3.2) of these fractures are listed for these fractures in Table 10.

In general, lithology is not a strong indicator of the presence of sharp inflows, although lava and welded tuff have a higher occurrence of sharp inflows than nonwelded tuff, which is the most common lithology for screened intervals with no inflow. The causes of the diffusive inflow responses listed in Table 9 are uncertain, although the evenly increasing flow in ER-EC-2A may be attributed to matrix flow through a nonwelded tuff. The other two diffusive inflow responses for ER-EC-5 upper and ER-EC-5 lower have insufficient fracture densities to explain increases in flow, yet these diffusive responses occur within moderately-to-densely welded tuffs, which typically have low primary porosity and permeability.

Table 9. Sharp, diffuse and no inflow categories for screened intervals.

Sharp Inflow						
Well	**Section**	**Interval (m)**	**Stratigraphy**	**Fractures**	**Dilated**	**Notes**
ER-EC-1	upper	~713	lava	3	0	non-dilated fractures located at 713, 714, and 715 m
ER-EC-1	upper	~755	lava	3	0	non-dilated fractures located at 755, 756 and 757 m
ER-EC-2A	middle	~963	reworked tuff	1	0	single, non-dilated fracture located at 963 m
ER-EC-4	upper	302-355	lava	5	0	sharp inflow increases at 327, 335, 342, and 355 m appear to be correlated to non-dilated fractures, no fractures listed above 327 m where sharp inflow increases are observed
ER-EC-5	middle	584-636	moderately welded tuff	11	1	sharp increases at 600, 612, 620 m appear to be correlated to non-dilated fractures, sharp increase at 637 m appears to be correlated to dilated fracture
ER-EC-6	upper	~497	lava	1	0	single, non-dilated fracture located at 497 m
ER-EC-8	upper	205-255	nonwelded tuff	10	0	sharp inflow increases at 209, 214, 220-225, 234, and 255 m appear to be correlated to non-dilated fractures, 1 dilated fracture at 252 m does not appear to contribute to flow
Diffuse Inflow						
Well	**Section**	**Interval**	**Stratigraphy**	**Fractures**	**Dilated**	**Notes**
ER-EC-2A	upper	510-660	nonwelded tuff	2	0	evenly increasing diffuse flow may be indicative of matrix flow contributions
ER-EC-5	upper	365-400	moderately welded tuff	N/A	N/A	no fractures listed above 580 m
ER-EC-5	lower	683-735	moderate-dense welded tuff	1	0	slight flow increase at 683 m may be correlated to non-dilated fracture
No Inflow						
Well	**Section**	**Interval**	**Stratigraphy**	**Fractures**	**Dilated**	**Notes**
ER-EC-1	middle	1,020-1,150	nonwelded tuff	0	0	
ER-EC-1	lower	1,350-1,430	nonwelded tuff	0	0	
ER-EC-2A	lower	1,370-1,480	nonwelded tuff	0	0	
ER-EC-4	middle	580-690	nonwelded tuff	10	0	
ER-EC-4	lower	945-1035	nonwelded tuff	9	0	no fractures detected below 1017 m
ER-EC-6	middle	670-760	nonwelded tuff	6	5	
ER-EC-6	lower	1,045-1,160	nonwelded tuff	4	0	
ER-EC-8	middle	440-460	partial-moderate welded tuff	0	0	
ER-EC-8	lower	510-540	nonwelded tuff	3	1	

Table 10. Conductive fractures identified in the ER-EC wells.

Fracture	Well	Lithology	Strike	Dip	Td	Ts
1	ER-EC-1	lava	31	52	0.62	0.67
2	ER-EC-1	lava	80	68	0.65	0.57
3	ER-EC-1	lava	97	71	0.53	0.40
4	ER-EC-1	lava	108	61	0.38	0.27
5	ER-EC-1	lava	106	74	0.47	0.30
6	ER-EC-1	lava	106	68	0.44	0.30
7	ER-EC-2A	reworked tuff	134	69	0.36	0.10
8	ER-EC-4	lava	87	71	0.59	0.48
9	ER-EC-4	lava	279	48	0.30	0.29
10	ER-EC-4	lava	254	55	0.53	0.54
11	ER-EC-4	lava	263	32	0.20	0.30
12	ER-EC-5	welded tuff	146	64	0.35	0.17
13	ER-EC-5	welded tuff	133	59	0.30	0.10
14	ER-EC-5	welded tuff	116	58	0.33	0.22
15	ER-EC-5	welded tuff	85	74	0.69	0.57
16	ER-EC-5	welded tuff	300	85	0.44	0.17
17	ER-EC-5	welded tuff	64	78	0.89	0.64
18	ER-EC-6	lava	280	77	0.53	0.37
19	ER-EC-8	nonwelded tuff	313	53	0.26	0.12
20	ER-EC-8	nonwelded tuff	289	67	0.40	0.25
21	ER-EC-8	nonwelded tuff	305	69	0.35	0.09
22	ER-EC-8	nonwelded tuff	291	73	0.43	0.23
23	ER-EC-8	nonwelded tuff	288	82	0.47	0.26
24	ER-EC-8	nonwelded tuff	106	76	0.47	0.28
25	ER-EC-8	nonwelded tuff	84	77	0.67	0.53

Fractures correlated to sharp inflows in Table 10 exhibit orientations that are sub-optimal for high dilation tendency values, with the exception of one fracture in ER-EC-5 (Figure 46). This is the only dilated fracture present within the areas of sharp inflows, which occurs over a discrete subset of the screened portions of the wells identified above. The pattern in orientation for conductive fractures lacks a clear pattern and appears to be a random subsampling of all borehole fractures shown in Figure 34. Excluding the one dilated fracture, dilation tendency values for fractures with sharp inflow range between 0.20 and 0.67, with an average of 0.45. These low dilation tendency values for conductive fractures certainly indicates that the stress field plays a minimal role in reducing apertures of fractures orthogonal to S_{Hmax}, at least within the zones of sharp inflow. Slip tendency values of the 25 conductive fractures are below the critically stressed threshold for horizontal stress anisotropy ratios of 1.5 and 2.5, and only two fractures have a slip tendency value greater than 0.60 for the unlikely case of a horizontal stress anisotropy ratio of 3.2. One of the two critically stressed fractures is the same fracture in ER-EC-5 with a high dilation tendency, and consistent with Section 3, dilation tendency is emphasized in this analysis.

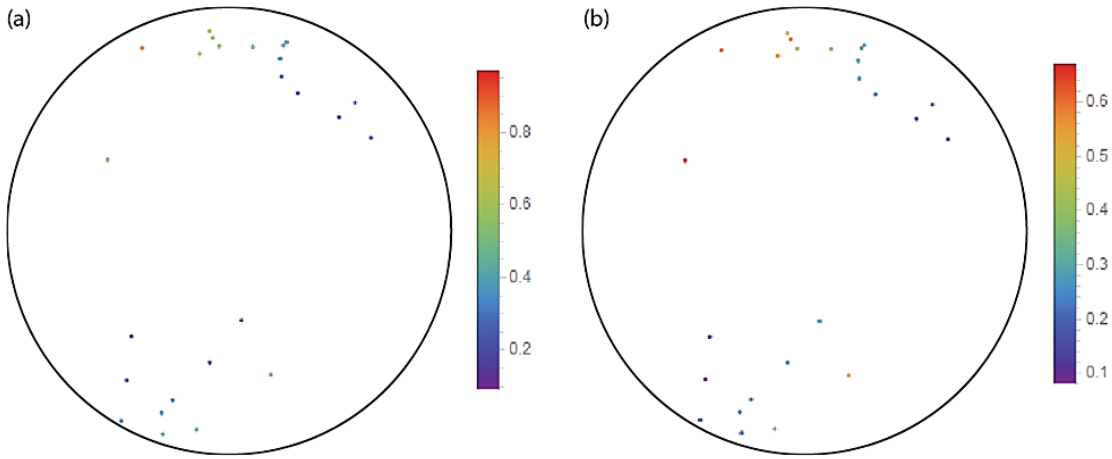

Figure 46. Southern-hemisphere, equal-area projection of 25 conducive fracture planes to poles with (a) dilation tendency for S_{Hmax}/S_{hmin} = 1.5 and (b) slip tendency for S_{Hmax}/S_{hmin} = 3.2. Horizontal stress directions determined from SATSI stress inversion solution nearest to each borehole.

The data on conductive fractures suggests that dilated background fractures exert little to no influence on flow to the ER-EC boreholes. However, it is unknown whether this conclusion can be explained by: (1) the stress field does not influence fluid flow through aperture dilation and/or compression for these smaller, background fractures, (2) fracture connectivity exerts a greater role on fluid flow to wells than the stress field, or (3) the frequency of dilated fractures is so low that dilated fractures are severely undersampled in the screened intervals of the ER-EC wells.

Undersampling of fracture networks is possible since only 294 fractures were detected over seven boreholes and a smaller subset of approximately 40 percent (n = 129) of these fractures are located within the screened well intervals. Fracture statistics for the entire screened intervals exhibiting sharp inflows is compiled in Table 11. The screened intervals with sharp inflow responses were selected because it is known that at least a subset of these fractures are open and conduct flow, as compared to fractures in the diffusive flow and no flow regimes. For screened sections with sharp inflow responses, conductive fractures are 11 percent to 39 percent of the total fracture population, with dilated fractures comprising 6 to 41 percent of the population. Only ER-EC-1 and ER-EC-5 contain more than two dilated fractures, with ER-EC-5 having the only dilated fracture correlated with a sharp inflow response. The other wells have an equal or higher number of fractures contributing to inflow than dilated fractures.

Table 11. Detailed fracture statistics over the entire screened intervals with discrete inflows.

Well	Section	Interval (m)	Total Fractures	Fracture Spacing	Dilated Fractures	Conductive Fractures	% Dilated	% Conductive
ER-EC-1	upper	700-860	57	3	7	6	12	11
ER-EC-2A	middle	940-1,080	6	27	1	1	17	17
ER-EC-4	upper	300-750	22	7	2	4	9	18
ER-EC-5	middle	577-637	17	9	7	5	41	29
ER-EC-6	upper	497-670	10	16	1	1	10	10
ER-EC-8	upper	210-300	18	9	1	7	6	39

The role of connectivity cannot be fully understood without a DFN analysis. However, borehole fracture logging cannot be used to characterize the physical dimension of the fractures it encounters, and the physical dimensions of these fractures are key to understanding network connectivity (e.g., Reeves *et al.* [2013]). It is likely that many of the fractures encountered in the boreholes are not of tectonic origin and formed from volumetric contraction during cooling (i.e., cooling joints), particularly for conductive fractures located in lava and welded tuff units. Cooling joints typically exhibit a more random orientation than tectonically influenced fractures (assuming cases in which the stress field has not significantly rotated over time) and the formation of interconnected pathways within these units would naturally exert a greater influence on fluid flow toward the well than the stress field. Moreover, cooling joints are generally small-scale structures that accommodate little of the surrounding stress, unlike large-scale faults, which are more intrinsically linked to the regional stress field.

SUMMARY AND CONCLUSIONS

The regional stress field in the vicinity of Central and Western Pahute Mesa is characterized using SATSI stress field inversion solutions to earthquake focal mechanism and other stress measurements from the NNSS. Pahute Mesa lies within a transtensional faulting regime represented by oblique slip on normal faults. The SATSI stress inversions from 699 short-period earthquake focal mechanisms provide estimates of S_{Hmax} directions ranging from N29°E to N63°E with an average of N42°E for Pahute Mesa. Although the focal mechanisms are poorly resolved, there is most certainly some degree of spatial heterogeneity within the stress field at PM caused by the structural complexity of the system, such as the presence of multiple calderas and structural zones within a relatively small region. The average maximum horizontal stress direction of N42°E is in agreement with stress directions obtained from large-diameter boreholes at Pahute Mesa and other stress measurements on the NNSS. Stress magnitudes compiled from overcoring and hydraulic fracturing methods indicate a range of ratios describing horizontal stress anisotropy.

The code RStress was developed in this study to compute dilation and slip tendencies for 15,625, 100-m long geologic structure segments digitized from a map combining PM Phase II geologic structures (NSTec, 2014) and faults from Slate *et al.* (1999). Both dilation and slip tendencies are highest for structures trending NE-SW, and lowest for structures trending NW-SE. RStress uses both spatially variable and average horizontal stress directions to compute dilation and slip tendency values. Differences in dilation and slip tendency values are greatest for the Central and Western Pahute Mesa CAUs, which have the highest density of faults and SATSI stress field solutions. In general, dilation and slip tendency values are lower for spatially variable stress fields.

Application of horizontal stress anisotropy tended to only moderately affect values of dilation tendency, while slip tendency values were significantly affected. Using all three horizontal stress anisotropy ratios, approximately 40 percent of the faults and geologic structures are identified for enhanced fluid flow. These faults are listed in Appendix D for inclusion of these structures in sub-CAU and CAU models of fluid flow and radionuclide transport. The enhanced flow designation is assigned to 151 structures on the basis of high

values of dilation tendency, and 58 structures on the basis of high values of slip tendency. A total of 52 of the 58 (~90 percent) critically stressed structures also had dilation tendency values exceeding 0.60. These results imply that the resolution of normal stress acting on fault planes exerts a greater influence on fault permeability than shear stress at Pahute Mesa.

Analysis of inflow responses to 7 ER-EC wells suggests that the stress field does not significantly influence fracture inflows at the borehole scale, although uncertainty exists with respect to undersampling of fractures, the influence of network connectivity on conductive and nonconductive fractures, and if conductive fractures encountered in the boreholes are predominately of nontectonic origin and less responsive to the surrounding stress field. It needs to be emphasized that the hydraulic tests conducted in the ER-EC wells are relatively small in scale, and cannot be used to estimate large-scale hydraulic conductivity and transmissivity of the geologic units encountered.

The influence of the regional stress field on large-scale permeability remains unknown. A total of 16 large-scale multi-well pumping tests of longer duration have been conducted for Pahute Mesa. Garcia *et al.* (2017) analyzed these tests and estimated transmissivity and storativity for hydrostratigraphic units (HSUs) affected by these tests using a series of 11 independent numerical ground water flow models and a modified Pahute Mesa hydrogeologic framework to reduce the number of HSUs in the drawdown impacted area from 55 to 22. Although the bulk hydraulic properties and their uncertainty bounds estimated by Garcia *et al.* (2017) are likely reliable, the numerical models precluded large-scale anisotropy effects of the stress field in fractured rock units by holding all HSUs isotropic.

Drawdown responses were recorded in observation wells at large distances from the pumping well in many of the tests, indicating that none of the faults or structural features in the area function as flow barriers (Garcia *et al.*, 2017). These drawdown observations support the dilation tendency results in this report as the only structures likely oriented transverse to the maximum horizontal stress and would be subjected to enough normal stress to serve as flow barriers (e.g., low dilation tendency values) are caldera margins, which do not mechanically function like tectonically derived normal faults. A more definitive assessment of the influence of the stress field on large-scale anisotropy would reanalyze each of the 16 multi-well tests separately to identify pumping-monitoring well pairs presumed in the Pahute Mesa hydrogeologic framework model to have a continuous fractured rock aquifer connection. This would eliminate dampened drawdown responses attributed to high-porosity, high-permeability HSUs. If a sufficient number of pumping-monitoring well pairs with continuous fractured rock aquifer connections are present for the same HSUs, a hydraulic diffusivity ellipse can be fit to the data (Ferrill *et al.*, 1999). This analysis is best left to a future study.

REFERENCES

Anderson, E.M., 1953. *The Dynamics of Faulting and Dyke Formation with Applications to Britain.* Edinburgh, Oliver and Boyd.

Anderson, R.E., compiler, 1998a. Fault number 1084, Belted Range fault, in Quaternary fault and fold database of the United States. U.S. Geological Survey website, http://earthquakes.usgs.gov/hazards/qfaults, accessed 09/17/2016 03:38 PM.

Anderson, R.E., compiler, 1998b. Fault number 1041, Boundary fault, in Quaternary fault and fold database of the United States. U.S. Geological Survey website, http://earthquakes.usgs.gov/hazards/qfaults, accessed 09/17/2016 03:39 PM.

Anderson, R.E., compiler, 1998c. Fault number 1065, Rock Valley fault zone, in Quaternary fault and fold database of the United States. U.S. Geological Survey website, http://earthquakes.usgs.gov/hazards/qfaults, accessed 09/17/2016 03:33 PM.

Anderson, R.E., compiler, 1998d. Fault number 1081, Yucca Mountain faults, western group, in Quaternary fault and fold database of the United States. U.S. Geological Survey website, http://earthquakes.usgs.gov/hazards/qfaults, accessed 09/17/2016 03:28 PM.

Anderson, R.E., compiler, 1998e. Fault number 1092, Unnamed faults of Pahute Mesa, in Quaternary fault and fold database of the United States. U.S. Geological Survey website, http://earthquakes.usgs.gov/hazards/qfaults, accessed 09/17/2016 03:50 PM.

Barton, C.A., and M.D. Zoback, 1995. Fluid flow along potentially active faults in crystalline rock. *Geology*, 23(8), pp. 683-686.

Bechtel Nevada, 2002. A Hydrostratigraphic Model and Alternatives for the Groundwater Flow and Contaminant Transport Model of Corrective Action Units 101 and 102; Central and Western Pahute Mesa, Nye County, Nevada. DOE/NV/11718-706.

Byerlee, J.D., 1978. Friction of rocks. *Pure Applied Geophysics*, 116, 615-626.

Carr, W.J., 1974. Summary of Tectonic and Structural Evidence for Stress Orientation at the Nevada Test Site. U.S. Geological Survey Open-file Report 74-176.

Ellis, W.L., and J.R. Ege, 1976. Determination of in-situ stress in U12g Tunnel, Rainier Mesa, Nevada Test Site, Nevada. U.S. Geological Survey Open-File Report 474-219.

Ellis, W.L., and J.E. Magner, 1982. Determination of the In Situ State of Stress at the Spent Fuel Test – Climax Site, Climax Stock, Nevada Test Site. U.S. Geological Survey Open-file Report 82-458.

Faulds, J.E., and C.D. Henry, 2008. Tectonic influences on the spatial and temporal evolution of the Walker Lane: An incipient transform fault along the evolving Pacific – North American plate boundary, *in* Spencer, J.E., and Titley, S.R., eds., Ores and orogenesis: Circum-Pacific tectonics, geologic evolution, and ore deposits. *Arizona Geological Society Digest*, 22, pp. 437-470

Ferrill, D.A., and A.P. Morris, 2003. Dilational normal faults. J*ournal of Structural Geology*, 25, pp. 183-196.

Ferrill, D.A., J. Winterle, G. Wittmeyer, D. Sims, S. Colton, A. Armstrong, and A.P. Morris, 1999. Stressed Rock Strains Groundwater at Yucca Mountain, Nevada. *GSA Today*, 9(5), pp. 1-7.

Garcia, C.A., T.R. Jackson, K.J. Halford, D.S. Sweetkind, N.A. Damar, J.M. Fenelon, and S.R. Reiner, 2017. Hydraulic characterization of volcanic rocks in Pahute Mesa using an integrated analysis of 16 multiple-well aquifer tests, Nevada National Security Site, 2009-14, U.S. Geological Survey Report 2016-5151.

Gillson, R.G., 1987. Analysis of Borehole Elongation in Yucca Flat and Pahute Mesa, Nevada Test Site, Nevada, Using the Digital Downhole Surveyor. Master's Thesis, University of Arkansas.

Gomberg, J., 1991. Seismicity and detection/location threshold in the southern Great Basin seismic network. *Journal of Geophysical Research*, 96, 16401-16414.

Haimson, B.C., 1981. A comparative study of deep hydrofracturing and overcoring stress measurements at six locations with particular interest to the Nevada Test Site. Proc Workshop on Hydraulic Fracturing Stress Measurements, U.S. National Committee for Rock Mechanics, Washington D.C., pp. 107-118.

Hamilton, R.M., B.E. Smith, F.G. Fischer, and P.J. Papanek, 1971. Seismicity of the Pahute Mesa area, Nevada Test Site, 8 December 1968 through 31 December 1970, Nevada Operations Office, U.S. Atomic Energy Commission. USGS Special Studies-89 1971.

Hardebeck, J.L., and A.J. Michael, 2006. Damped regional stress inversions: methodology and examples for southern California and the Coalinga aftershock sequence. *Journal of Geophysical Research*, 111, B11310, doi:10.1029/2005JB004144.

Hardebeck, J.L., and P.M. Shearer, 2002. A new method for determining first-motion focal mechanisms. *Bulletin of the Seismological Society of America*, 92, 2264–2276.

Harmsen, S.C., 1987. Evaluation of the seismicity in the southern Great Basin and its relationship to the tectonic framework of the region. U. S. Geological Survey Open-File Report 87-408.

Harmsen, S.C., 1991. Seismicity and focal mechanisms for the southern Great Basin of Nevada and California 1990. U. S. Geological Survey Open-File Report 91-367.

Harmsen, S.C., 1992. Seismicity and focal mechanisms for the southern Great Basin of Nevada and California 1991. U. S. Geological Survey Open-File Report 92-340.

Harmsen, S.C., 1993. Preliminary seismicity and focal mechanisms for the southern Great Basin of Nevada and California: January 1992 through September 1992. U. S. Geological Survey Open-File Report 93-369.

Harmsen, S.C., A.M. Rogers, and M.E. Meremonte, 1986. Inferences about the local stress field from focal mechanisms: applications to the earthquakes in the southern Great Basin of Nevada. *Bulletin of the Seismological Society of America*, 76, 1560-1572.

Harmsen, S.C., and C.G. Bufe, 1992. Seismicity and focal mechanisms in the southern Great Basin of Nevada and California: 1987 through 1989. U. S. Geological Survey Open-File Report, 91-572.

Jaeger, J.C., N.G.W. Cook, and R.W. Zimmerman, 2007. *Fundamentals of Rock Mechanics*, 4th Ed. Blackwell Publishing, Malden, MA.

Kelly, P.A., 2015. Lecture Notes in Solid Mechanics: Foundations of Continuum Mechanics. Available from from http://homepages.engineering.auckland.ac.nz/~pkel015/SolidMechanicsBooks/index.html.

Kisslinger, C., J.R. Bowman, and K. Koch, 1981. Procedures for computing focal mechanisms from local *(SV/PX)* data. *Bulletin of the Seismological Society of America*, 71, 1719-1729.

Klein, F.W., 2002. User's Guide to HYPOINVERSE-2000, a Fortran Program to Solve for Earthquake Locations and Magnitudes. U.S. Geological Survey Open-File Report, 2002-171, p. 121.

Lahr, J.C., 1979. HYPOELLIPSE: A computer program for determining local earth- quake hypocentral parameters, magnitude, and first motion pattern. U.S. Geological Survey Open-File Report 79-431, p. 53.

Lee, M.Y., and B.C. Haimson, 1999. Initial Stress Measurements in the Exploratory Studies Facility Yucca Mountain, Nevada. *Rock Mechanics for Industry*, Balkema, Rotterdam ISBN 90 5809 052 3.

Ljunggren, C., Y. Chang, T. Jason, and R. Christiansson, 2003. An overview of rock stress measurement methods. *International Journal of Rock Mechanics and Mining Sciences*, 20, 975-989.

Machette, M.N., and R.E. Klinger, compilers, 2002. Fault number 141b, Northern Death Valley fault zone, Mesquite Flat-Screwbean Spring section, in Quaternary fault and fold database of the United States. U.S. Geological Survey website, http://earthquakes.usgs.gov/hazards/qfaults, accessed 09/17/2016 04:02 PM

Meremonte, M.E., and A.M. Rogers, 1987. Historical catalog of southern Great Basin earthquakes 1868-1978. U.S. Geological Survey, Open-File Report 87-80.

Michael, A.J., 1984. Determination of stress from slip data: faults and folds. *Journal of Geophysical Research*, 89, 11,517-11,526.

Minor, S.A., 1989. Paleostress investigation near Rainier Mesa, Nevada Test Site. U.S. Geological Survey Paper, P.O. Box 25046, MS 913 Denver, CO 80225.

Moeck, I., G. Kwiatek, and G. Zimmermann, 2009. Slip tendency analysis, fault reactivation potential and induced seismicity in a deep geothermal reservoir. *Journal of Structural Geology*, 31(10), 1174-1182.

Morris, A., D.A. Ferrill, and D.B. Henderson, 1996. Slip tendency analysis and fault reactivation. *Geology*, 24(3), 275-278.

National Nuclear Security Administration, 2009. Phase II Corrective Action Investigation Plan Action Units 101 and 102: Central and Western Pahute Mesa, Nevada Test Site, Nye County, Nevada. U.S. Department of Energy, DOE/NV-1312.

National Research Council, 1996. *Rock Fractures and Fluid Flow: Contemporary Understanding and Applications*. National Academy Press, Washington, D.C., p. 568.

National Security Technologies (NSTec), LLC, 2014. Phase II Hydrostratigraphic Framework Model for Corrective Action Units 101 and 102: Central and Western Pahute Mesa, Nye County, Nevada. U.S. Department of Energy, National Nuclear Security Administration, Nevada Site Office, DOE/NV/25946-xxx, draft.

Oberlander, P.L., B.F. Lyles, and C.E. Russell, 2002. Summary Report: Borehole Testing and Characterization of Western Pahute Mesa – Oasis Valley ER-EC Wells. Desert Research Institute Publication No. 45195, DOE/NV/13609-23.

Pawloski, G.A., J. Murtz, and S.L. Drellack, 2010. The Underground Test Area Project of the Nevada Test Site: Building Confidence in Groundwater Flow and Transport Models at Pahute Mesa Through Focused Characterization Studies. Waste Management 2010 Conference, LLNL-CONF-422250, Phoenix, AZ, March 7-11.

Press, W.H., S.A. Teukolsky, W.T. Vetterling, and B.P. Flannery, 1996. Numerical Recipes in Fortran 90. *The Art of Scientific Computing*, 2nd Ed., Volume 2 of Fortran Numerical Recipes, Cambridge University Press, U.K.

Reasenberg, P.A., and D. Oppenheimer, 1985. FPFIT, FPPLOT, FPPAGE: Fortran computer programs for calculating and displaying earthquake fault-plane solutions. U.S. Geological Survey Open-File Rept. 85-739.

Reeves, D.M., R. Parashar, K. Pohlmann, C. Russel, and J. Chapman, 2014. Development and calibration of dual-permeability models with discontinuous fault networks. *Vadose Zone Journal*, 13(8), doi:10.2136/vzj2013.10.0183.

Reeves, D.M., R. Parashar, G. Pohll, R. Carroll, T. Badger, and K. Willoughby, 2013. Practical guidelines for horizontal hillslope drainage networks in fractured rock. *Engineering Geology*, 2(2), 1-10, doi:10.3882/j.issn.1674-2370.2012.02.001.

Rehfeldt, K.R., P. Hufschmeid, L.W. Gelhar, and M.E. Schaefer, 1989. Measuring hydraulic conductivity with the borehole flowmeter. Electric Power Research Institute, EN-6511, September 1989.

Reheis, M.C., compiler, 1994. Fault number 49c, Fish Lake Valley fault zone, Oasis section, in Quaternary fault and fold database of the United States. U.S. Geological Survey website, http://earthquakes.usgs.gov/hazards/qfaults, accessed 09/17/2016 04:03 PM.

Rogers, A.M., S.C. Harmsen, W.J. Carr, and W. Spence, 1983. Southern Great Basin seismological data report for 1981 and preliminary data analysis. U.S. Geological Survey Open-File Report 8-669.

Slate, J.L., M.E. Berry, P.D. Rowley, C.J. Fridrich, K.S. Morgan, J.B Workman, O.D. Young, G.L. Dixon, V.S. Williams, E.H. McKee, D.A. Ponce, T.G. Hildenbrand, W.C. Swadley, S.C. Lundstrom, E.B. Ekren, R.G. Warren, J.C. Cole, R.J. Fleck, M.A. Lanphere, D.A. Sawyer, S.A. Minor, D.J. Grunwald, R.J. Laczniak, C.M. Menges, J.C. Yount, and A.S. Jayko, 1999. Digital Geologic Map of the Nevada Test Site and Vicinity, Nye, Lincoln, and Clark Counties, Nevada, and Inyo County, California. U.S. Geological Survey Open-File Report 99-554-A, U. S. Geological Survey, Denver, Colorado.

Smith, K.D., J.N. Brune, M. Savage, D.M. dePolo, and A. Sheehan, 2001. The 1992 Little Skull Mountain earthquake sequence. *Bulletin of the Seismological Society of America*, 91, 1595-1606.

Smith, C., W.C. Vollendorf, and W.E. Warren, 1981. In-Situ Stress from Hydraulic Fracture Measurements in G Tunnel, Nevada Test Site. Unlimited Release SAND80-1138, Sandia National Laboratories, Albuquerque, NM 87185.

Snoke, J.A., J.W. Munsey, A.G. Teague, and G.A. Bollinger, 1984. A program for focal mechanism determination by combined use of polarity and amplitude ratio data. *Earthquake Notes*, v. 55, p. 15.

Snow, D.T., 1965. A parallel plate model of fractured permeable media. PhD Thesis, University of California, Berkeley, USA.

Springer, J.E., and R.K. Thorpe, 1981. Borehole Elongation Versus In Situ Stress Orientation. Lawrence Livermore National Laboratory, University of California, Livermore, California 94550.

Springer, J.E., R.K. Thorpe, and H.L. McKague, 1984. Borehole Elongation and its Relation to Tectonic Stress at the Nevada Test Site. U.S. Geological Survey and Lawrence Livermore National Laboratory, University of California, Livermore, California 94550.

Stock, J.M., J.H. Healy, S.H. Hickman, and M.D. Zoback, 1985. Hydraulic Fracturing Stress Measurements at Yucca Mountain, Nevada, and Relationship to the Regional Stress Field. *Journal of Geophysical Research*, 90(B8), 8691-8706.

Stuckless, J.S., and R.A. Levich, editors, 2007. The Geology and Climatology of Yucca Mountain and Vicinity, southern Nevada and eastern California. Geological Society of America Memoir 199, editors Stuckless and Levich, Boulder, CO.

Terzaghi, R., 1965. Sources of error in joint surveys. *Geotechnique*, 15, 287-304.

Von Seggern, D.H., and K.D. Smith, 1997. Seismicity in the vicinity of Yucca Mountain, Nevada, for the period October 1, 1995, to September 30, 1996. Report to the Yucca Mountain Project, DOE–YMSCO, Las Vegas NV (MOL #19981124.0334).

Von Seggern, D.H., and D.M. dePolo, 1998. Seismicity in the vicinity of Yucca Mountain, Nevada, for the period October 1, 1996, to September 30, 1997. Report to the Yucca Mountain Project, DOE–YMSCO, Las Vegas NV (DTN #MO980683117412.000).

Von Seggern, D.H., and K.D. Smith, 2001. Seismicity in the vicinity of Yucca Mountain, Nevada, for the period October 1, 1999, to September 30, 2000. Report to the Yucca Mountain Project, DOE–YMSCO, Las Vegas NV (MOL #20010725.0220).

Von Seggern, D.H., and K.D. Smith, 2002. Seismicity in the vicinity of Yucca Mountain, Nevada, for the period October 1, 2000, to September 30, 2001. Report to the Yucca Mountain Project, DOE–YMSCO, Las Vegas NV (DTN #MO0205UCC012DV.008).

Von Seggern, D.H., and K.D. Smith, 2002. Seismicity in the vicinity of Yucca Mountain, Nevada, for the period October 1, 2001, to September 30, 2002. Report to the Yucca Mountain Project, DOE–YMSCO, Las Vegas NV (MOL#20030910.0265).

Von Seggern, D.H., and K.D. Smith, 2007. Seismicity in the vicinity of Yucca Mountain, Nevada, for the period October 1, 2003, to September 30, 2004. Report to the Yucca Mountain Project, DOE–YMSCO, Las Vegas NV.

Von Seggern, D.H., K.D. Smith, and G.P. Biasi, 2001. Seismicity in the vicinity of Yucca Mountain, Nevada, for the period October 1, 1997, to September 30, 1999. Report to the Yucca Mountain Project, DOE–YMSCO, Las Vegas NV (MOL #20010725.0221).

Warpinski, N.R., and L.W. Teufel, 1991. In Situ Stress Measurements at Rainier Mesa, Nevada Test Site – Influence of Topography and Lithology on the Stress State in Tuff. *Journal of Rock Mechanics, Minerals, Science, & Geomechanics, Abstract*, v. 28, pp. 143-161.

Yow, J.L., 1984. Geologic structure mapping database, Spent Fuel Test – Climax, Nevada Test Site. DE85006267.

Zoback, M.D., 2010. *Reservoir Geomechanics*. Cambridge University Press, Cambridge, UK.

Zoback, M.D., D. Moos, and L. Mastin, 1985. Well bore breakouts and in situ stress. *Journal of Geophysical Research*, 90(B7), 5523-5530.

APPENDIX A: HAMILTON EARTHQUAKE FOCAL MECHANISMS

No record exists of the focal mechanism developed in the Hamilton *et al.* (1971) post-Benham UNE induced seismicity study. Attempts to locate sources of the Hamilton study mechanisms, first motions data, or phase data were unsuccessful. To compile the Hamilton results, focal mechanisms were determined by hand-geocoding the figure from the Hamilton study (Figure A-1) with topography (Figure A-2) and assigning reference points (lat-lons) to individual mechanism solutions (Figure A-3); each mechanism was determined 'visually' in a best-fit sense (Figure A-4). This is the only known digital compilation of the Hamilton results. As stated in the Hamilton report, some mechanisms are composite solutions, others are individual event solutions; the report does not provide detail on the particular events in the study's figure (i.e., origin times, locations, magnitudes, mechanism solutions).

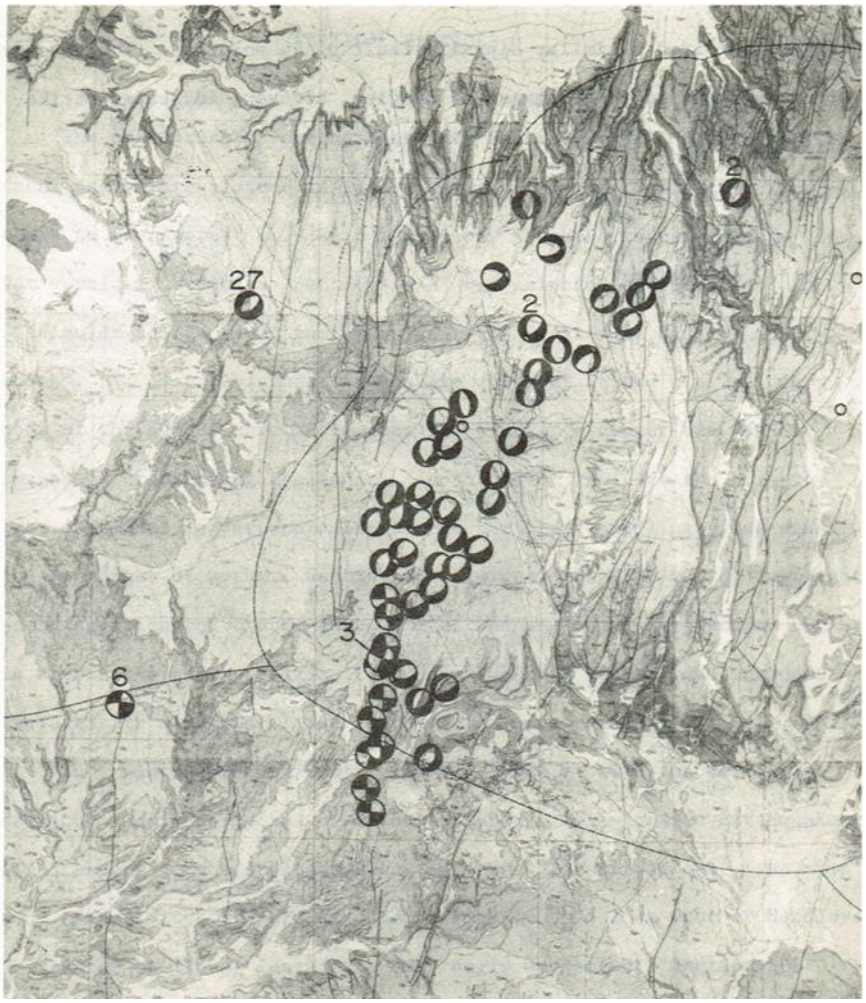

Figure A-1. Scanned image of short period focal mechanisms from Hamilton *et al.* (1971); page 59.

Figure A-2. For geo-coding, overlay of focal mechanism image (Figure A-1) on a topographic reference.

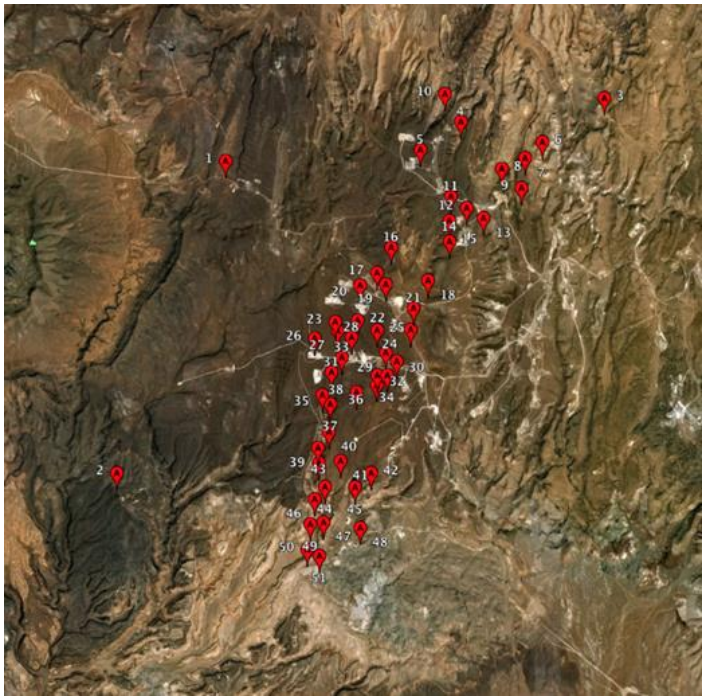

Figure A-3. KML reference map of short-period mechanism locations for visually determining solutions.

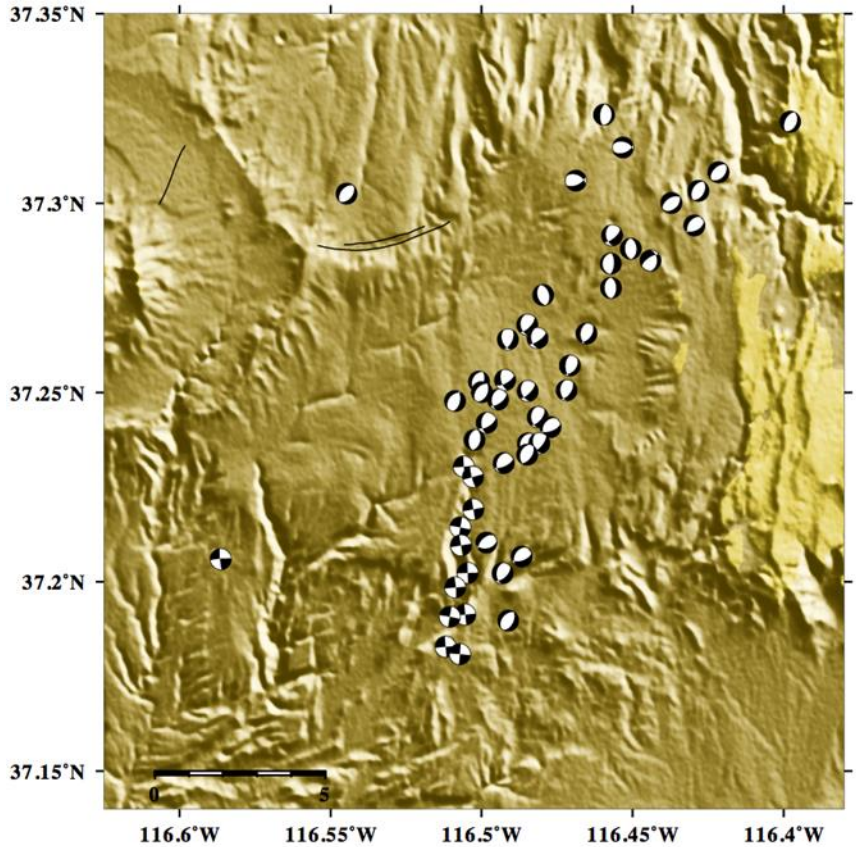

Figure A-4. Map of visually fit strike-dip-rake esimates (‘beach ball’, representation from Figure A-1).

Table A-1. Visually fit focal mechanisms solutions.

Hamilton *et al.* 1971-Induced Seismicity Short Period Mechanisms
Lon Lat Depth St dp rak Scale
-116.544698748722 37.30256500511814 10.000 40 45 -90 1.00 0
-116.5864157076541 37.20596785353285 10.000 265 85 5 1.00 0
-116.3978054946366 37.3215231563902 10.000 25 40 -90 1.00 0
-116.4531853916696 37.31471216430632 10.000 285 45 -65 1.00 0
-116.468750833125 37.30598560920463 10.000 295 45 -50 1.00 0
-116.4215725617348 37.30821227621222 10.000 45 40 -90 1.00 0
-116.428220072816 37.30330834793637 10.000 30 45 -90 1.00 0
-116.4371732955044 37.30007103458557 10.000 50 40 -95 1.00 0
-116.4295496757804 37.29413952202265 10.000 65 50 -70 1.00 0
-116.4594692439315 37.32336179851247 10.000 5 30 -90 1.00 0
-116.4567805429336 37.29155523522241 10.000 50 65 -55 1.00 0
-116.4506057330492 37.28801907272353 10.000 358 45 -90 1.00 0
-116.4440997788815 37.28487125380173 10.000 235 65 -60 1.00 0
-116.4572462317501 37.28406849232428 10.000 03 65 -90 1.00 0
-116.457151020727 37.27767798002669 10.000 359 50 -90 1.00 0

Table A-1. Visually fit focal mechanisms solutions (continued).

```
# Hamilton et al. 1971-Induced Seismicity Short Period Mechanisms
# Lon Lat Depth St dp rak Scale
 -116.4795762933399 37.27578674569381 10.000 345 45 -90 1.00 0
 -116.484897534527 37.26794642439798 10.000 45 65 -60 1.00 0
 -116.4652712738509 37.26563692350306 10.000 35 50 -70 1.00 0
 -116.4814637887552 37.26438949436972 10.000 55 70 -55 1.00 0
 -116.4913129040981 37.26405161796154 10.000 25 55 -60 1.00 0
 -116.4707857195452 37.25714774539568 10.000 40 40 -60 1.00 0
 -116.4922306496674 37.25334756061047 10.000 60 65 -35 1.00 0
 -116.500838173091 37.2528875534269 10.000 20 55 -90 1.00 0
 -116.4718738415619 37.25060858225817 10.000 35 55 -65 1.00 0
 -116.4847327201699 37.25039176888514 10.000 45 70 -55 1.00 0
 -116.5087865583802 37.24776140683926 10.000 220 40 -70 1.00 0
 -116.4999258867145 37.25015705396926 10.000 220 45 -80 1.00 0
 -116.4945811654868 37.24816903459765 10.000 55 60 -60 1.00 0
 -116.4814226020317 37.24355245599186 10.000 40 60 -65 1.00 0
 -116.4772085385409 37.24088289892995 10.000 70 60 -70 1.00 0
 -116.5023393539087 37.23749840652145 10.000 15 45 -85 1.00 0
 -116.4846900733097 37.23656900120394 10.000 20 60 -90 1.00 0
 -116.4983286677580 37.24201327042482 10.000 60 60 -50 1.00 0
 -116.480866438643 37.23661089608783 10.000 40 65 -55 1.00 0
 -116.5058579477895 37.23047546075236 10.000 85 90 -0 1.00 0
 -116.4849134564289 37.23361478965854 10.000 35 55 -80 1.00 0
 -116.5028252180078 37.22773301680198 10.000 75 90 -10 1.00 0
 -116.492674596095 37.23139627321887 10.000 65 65 -65 1.00 0
 -116.5070336029949 37.21435726436088 10.000 100 90 -0 1.00 0
 -116.5027004114153 37.21920553400302 10.000 80 90 -0 1.00 0
 -116.4984519220923 37.21038730085984 10.000 80 45 -65 1.00 0
 -116.4867250012534 37.20668879613549 10.000 70 60 -70 1.00 0
 -116.5067974731835 37.20964566611386 10.000 80 90 -0 1.00 0
 -116.5046222484831 37.20232972996942 10.000 88 90 -0 1.00 0
 -116.4930109606209 37.2023131748368 10.000 45 55 -65 1.00 0
 -116.5087438769884 37.19851529041288 10.000 85 90 5 1.00 0
 -116.5054095046597 37.1913748359906 10.000 85 90 -0 1.00 0
 -116.4911521656511 37.18976587444297 10.000 220 40 -80 1.00 0
 -116.5105650873215 37.19075879549764 10.000 100 90 -0 1.00 0
 -116.5118958687141 37.18283576569077 10.000 85 90 -0 1.00 0
 -116.5071932075793 37.18088535993502 10.000 95 90 -0 1.00 0
```

Lat: estimated Latitude
Lon: estimated Longitude
St: estimated Strike angle
Dp: estimated Dip angle
Rk: estimated Rake angle
Depth: place holder and not used in the stress inversion
Scale: arbitrary scale value for plotting

APPENDIX B: SATSI STRESS FIELD INVERSION

(Note that SATSI deviatoric stress ratios adopt the tension positive convention)

COORDINATES ARE EAST, NORTH, UP.
Stress tensors are:

X	Y	See	Sen	Seu	Snn	Snu	Suu
0	16	0.442245	-0.763199	0.205552	0.181979	0.106241	-0.624224
1	14	0.472096	-0.628633	0.000209	-0.005090	0.035823	-0.467006
2	12	0.546279	-0.786167	-0.137760	0.112959	0.248472	-0.659238
2	14	0.450653	-0.295949	-0.112770	0.028139	0.037757	-0.478793
2	17	0.255532	-0.373203	0.020670	0.105577	0.028854	-0.361109
2	18	0.359784	-0.605703	0.141240	-0.077506	0.312179	-0.282278
3	14	0.476948	-0.694336	-0.020047	0.021608	0.052843	-0.498556
4	14	0.511943	-0.806145	0.030020	0.013548	0.105427	-0.525490
4	15	0.512397	-0.808320	0.002602	0.052048	0.104542	-0.564445
5	16	0.495635	-0.884253	0.027406	0.121561	0.243279	-0.617196
7	6	0.031279	-0.823004	0.367806	1.035867	-0.357901	-1.067146
8	7	0.216814	-0.903388	0.145444	0.353817	0.138923	-0.570631
8	14	0.557204	-0.918411	0.140995	0.011841	0.088389	-0.569045
9	10	0.501306	-0.968547	-0.031144	0.148558	-0.048094	-0.649864
9	17	0.575889	-0.970066	0.102342	-0.075402	0.074055	-0.500487
10	7	0.368878	-0.920542	-0.076505	0.354625	-0.068497	-0.723503
10	8	0.332503	-0.898360	-0.168370	0.371933	-0.167537	-0.704436
10	9	0.413067	-0.956121	-0.105781	0.302680	-0.028477	-0.715746
10	11	0.650537	-0.935556	-0.151903	0.012233	0.130121	-0.662770
10	12	0.606335	-0.933852	0.041314	0.138016	0.074075	-0.744351
10	13	0.583689	-0.928043	0.050160	0.055836	0.077575	-0.639525
10	14	0.458862	-0.987704	0.074028	-0.083330	0.081632	-0.375532
10	15	0.760091	-0.891438	0.143058	-0.021286	0.007167	-0.738805
10	16	0.703864	-0.955939	0.123203	-0.201137	0.030069	-0.502727
10	17	0.569970	-0.976169	0.102851	-0.116895	0.101608	-0.453076
10	27	0.299100	-1.171723	0.309788	-0.099756	0.073930	-0.199344
11	10	0.545895	-0.940345	-0.179742	0.232426	0.087438	-0.778321
11	11	0.677841	-0.812664	-0.002475	0.196213	0.051317	-0.874054
11	15	0.861496	-0.900917	0.053950	-0.293362	-0.021874	-0.568134
11	16	0.653237	-0.969653	0.103571	-0.206004	0.150344	-0.447233
11	17	0.490346	-1.033414	0.084967	-0.125153	0.187876	-0.365193
11	23	0.320993	-1.050020	0.186204	-0.032954	-0.161269	-0.288039
11	24	0.347537	-1.038619	0.163449	-0.027904	-0.105322	-0.319633
11	25	0.325573	-0.992246	0.228487	-0.010046	-0.017669	-0.315527
11	26	0.388457	-0.998213	0.184751	0.055744	0.066708	-0.444201
12	22	0.373862	-0.968900	0.201756	-0.014021	-0.198757	-0.359841
12	24	0.373884	-1.014602	0.160237	-0.016210	-0.119576	-0.357674
12	27	0.395788	-1.031884	0.091942	-0.002844	-0.028798	-0.392944
14	22	0.365972	-0.925577	0.323644	0.017497	-0.315463	-0.383469
14	26	0.433720	-0.901408	-0.087960	0.036796	-0.119384	-0.470516
15	14	0.670209	-0.994644	0.310475	-0.294147	0.061339	-0.376062
15	15	0.454665	-0.999876	0.258194	-0.165548	-0.004290	-0.289118
16	11	0.436340	-1.049305	-0.018747	0.178372	0.157988	-0.614712

16 12 0.526630 -1.017172 0.072266 0.086523 0.072472 -0.613153
16 13 0.522495 -1.028434 0.225911 -0.346926 0.009592 -0.175569
16 14 0.593654 -0.986659 0.210891 -0.196845 0.004146 -0.396808
16 22 0.443805 -0.871341 0.232102 0.099357 0.053218 -0.543162
17 12 0.447878 -1.074801 0.092089 0.176838 0.058048 -0.624716
17 13 0.461696 -1.016619 0.153350 -0.013261 0.015160 -0.448435
17 16 0.040683 -0.873820 0.119984 0.284393 -0.272560 -0.325076
17 19 0.337860 -0.902358 0.142835 0.129844 -0.172314 -0.467705
18 8 0.583569 -0.783066 0.015099 0.211871 0.182898 -0.795441
18 23 0.524357 -0.829262 0.025975 -0.063034 -0.206637 -0.461322
19 12 0.577557 -0.959747 0.028490 0.178733 0.142629 -0.756290
19 13 0.394381 -0.968409 0.166855 0.141959 0.043207 -0.536340
19 18 0.318680 -0.806975 -0.032308 0.349993 -0.256548 -0.668673
20 8 0.671857 -0.613092 0.089055 0.200342 0.351041 -0.872199
20 9 0.737969 -0.554973 0.098809 0.136368 0.344888 -0.874336
20 10 0.774184 -0.633329 0.054704 0.076913 0.213667 -0.851097
20 11 0.662068 -0.864566 0.087564 0.183383 0.134199 -0.845451
20 12 0.569715 -0.928506 0.015646 0.228209 0.024148 -0.797924
20 13 0.412380 -0.945893 0.073556 0.228583 0.000854 -0.640963
20 19 0.201096 -0.772217 0.069043 0.158985 -0.433430 -0.360081
20 26 0.485226 -0.835635 -0.136259 0.059910 -0.153483 -0.545136
21 8 0.699908 -0.613946 0.021217 0.392424 0.357241 -1.092332
21 9 0.776127 -0.498488 0.076315 0.260746 0.369176 -1.036874
21 10 0.744523 -0.525098 0.073362 0.190300 0.333402 -0.934823
21 11 0.681545 -0.657492 0.066227 0.225779 0.234341 -0.907324
21 12 0.498881 -0.762251 -0.010896 0.342574 0.086627 -0.841454
21 19 0.085544 -0.787638 0.042963 0.014050 -0.482303 -0.099594
21 24 0.368649 -0.898786 -0.057339 -0.000646 -0.215092 -0.368003
22 7 0.648363 -0.665095 0.094955 0.518187 0.270423 -1.166550
22 8 0.643118 -0.626861 0.085574 0.406636 0.291842 -1.049754
22 9 0.733377 -0.522257 0.008547 0.408625 0.278878 -1.142003
22 15 0.166267 -0.891482 0.121720 0.316121 -0.153983 -0.482387
22 19 0.028610 -0.885660 0.094943 0.053002 -0.306628 -0.081612
23 8 0.269716 -0.888611 0.088691 0.403985 0.076728 -0.673701
23 13 0.147814 -0.740798 -0.138563 0.476633 -0.031178 -0.624447
23 15 0.084169 -0.874376 0.131001 0.342363 -0.163534 -0.426532
23 18 -0.032561 -1.025398 -0.030406 0.180469 -0.329339 -0.147908
23 19 0.027418 -0.993098 0.022788 0.105378 -0.287127 -0.132796
23 20 0.077831 -0.616089 0.021031 0.045393 0.031326 -0.123224
24 7 0.306223 -0.778023 0.130966 0.493676 0.054410 -0.799899
24 8 0.205346 -0.870288 0.031454 0.454911 -0.028292 -0.660256
24 12 -0.062585 -0.627962 -0.097097 0.720959 -0.110192 -0.658373
24 14 -0.115809 -0.777813 0.152943 0.412687 -0.205803 -0.296878
25 8 0.055257 -0.773311 0.123516 0.528867 -0.250789 -0.584124
25 9 0.132868 -0.718046 0.141675 0.666999 -0.117381 -0.799867
25 10 0.281312 -0.574383 0.056047 0.794378 -0.055760 -1.075690
25 11 0.207127 -0.500045 -0.079713 0.790058 0.034834 -0.997185
25 12 -0.243235 -0.599457 -0.215936 0.907895 -0.108998 -0.664660
25 14 -0.091267 -0.788947 0.112586 0.463314 -0.124771 -0.372047
25 18 -0.007201 -0.908065 -0.309723 0.162033 -0.275608 -0.154832
25 19 -0.033912 -1.060674 -0.229949 0.085835 -0.313284 -0.051922

25 21 0.050424 -0.894398 -0.087664 -0.124358 0.044166 0.073934
26 8 -0.096491 -0.674281 0.204478 0.706236 -0.260781 -0.609745
26 9 -0.012282 -0.733154 0.251400 0.679906 -0.181558 -0.667623
26 10 0.088796 -0.682069 0.122782 0.757350 -0.127729 -0.846146
26 11 0.054275 -0.502220 0.158404 0.826000 -0.069290 -0.880274
26 12 -0.381106 -0.410310 -0.043395 0.798128 -0.284592 -0.417021
26 20 0.063947 -0.948469 -0.111644 0.030866 -0.073451 -0.094812
26 22 0.162610 -0.932932 -0.128426 -0.051509 -0.003185 -0.111101
27 14 -0.183021 -0.570324 0.235443 0.193119 0.021847 -0.010097
27 25 0.288868 -0.942894 -0.303187 -0.039398 0.095220 -0.249470
28 9 -0.028793 -0.746286 0.199980 0.649650 -0.228307 -0.620857
28 13 -0.169605 -0.751112 0.119093 0.504643 -0.058317 -0.335038
28 14 -0.047913 -0.792343 0.123833 0.420383 -0.098145 -0.372469
28 16 0.002574 -0.879474 0.092113 0.484273 -0.083545 -0.486847
28 20 0.114975 -0.879457 -0.048301 0.039474 -0.247298 -0.154449
28 30 0.905283 -0.553543 0.137997 0.098436 0.099926 -1.003719
29 15 -0.074752 -0.896768 0.150893 0.398469 -0.109473 -0.323717
29 28 0.619971 -0.920153 -0.107910 -0.068799 0.177813 -0.551173
29 30 0.797066 -0.815788 -0.102376 -0.067606 0.124305 -0.729460
30 15 -0.169400 -0.827977 0.030636 0.689673 -0.096382 -0.520272
30 24 0.297191 -0.955962 -0.193071 -0.071246 0.045409 -0.225945
30 25 0.435186 -0.932954 -0.019968 -0.033996 0.097112 -0.401190
30 26 0.505525 -0.949238 -0.166122 -0.042379 0.202898 -0.463145
30 28 0.609360 -0.977795 -0.105581 -0.076705 0.203083 -0.532654
30 29 0.743088 -0.833590 -0.089500 -0.211467 0.290098 -0.531621
30 30 0.868833 -0.690307 0.008834 -0.009146 0.060110 -0.859687
31 15 0.020027 -0.879307 0.055257 0.514941 -0.053161 -0.534968
31 22 0.286028 -0.941129 -0.092263 -0.028163 0.027909 -0.257865
31 24 0.338141 -0.963082 -0.192131 -0.060086 0.082915 -0.278055
31 27 0.524832 -1.009292 -0.101038 -0.011793 0.161689 -0.513039
31 28 0.573057 -0.985688 -0.132804 -0.011252 0.190122 -0.561805
31 29 0.736134 -0.859451 -0.091423 -0.062928 0.235403 -0.673207
31 30 0.814231 -0.841906 -0.071168 -0.004684 0.130621 -0.809547
32 8 -0.169931 -0.853579 0.090143 0.406636 -0.149472 -0.236705
32 13 -0.045811 -0.829039 -0.135318 0.360014 -0.087086 -0.314203
32 15 0.092699 -0.915680 0.035192 0.364964 -0.069526 -0.457663
32 17 0.462953 -0.854163 0.015024 0.086954 -0.025299 -0.549907
32 18 0.647392 -0.689694 -0.122766 0.101991 -0.044666 -0.749384
32 19 0.245335 -0.862093 0.033030 -0.011942 -0.060082 -0.233393
32 20 -0.031910 -0.837029 0.123737 -0.116334 0.021364 0.148244
32 23 0.471138 -0.953186 -0.119681 -0.030527 0.136609 -0.440611
33 14 0.096990 -0.909949 -0.003121 0.326087 -0.053065 -0.423077
33 15 0.189175 -0.905334 0.031105 0.348203 -0.019688 -0.537379
33 18 0.409294 -0.874860 0.012590 -0.029080 -0.088020 -0.380214
33 21 0.309177 -0.923396 -0.108136 -0.025763 -0.006264 -0.283414
34 7 -0.015094 -0.833166 0.154422 0.447850 -0.199221 -0.432756
34 8 -0.104812 -0.860915 0.173138 0.187230 -0.258958 -0.082418
34 11 -0.141520 -0.575521 0.063805 0.159634 -0.454675 -0.018115
34 25 0.486842 -0.982491 -0.098488 0.051991 0.081093 -0.538833
34 30 0.634490 -0.920602 0.060226 0.003531 0.293567 -0.638021
35 9 0.121656 -0.895068 0.258070 0.335737 -0.229354 -0.457394

35	17	0.350690	-0.961550	0.002691	0.097056	-0.096233	-0.447746
35	18	0.403443	-0.971096	-0.010934	0.012077	-0.104191	-0.415520
35	19	0.489553	-0.915011	-0.064161	0.021993	-0.017756	-0.511546
35	25	0.501807	-0.971502	-0.118504	0.078106	0.055423	-0.579913
35	28	0.474735	-1.024035	-0.017291	0.143695	0.074331	-0.618430
36	8	0.072878	-0.851689	0.391837	0.283835	-0.328694	-0.356713
36	17	0.341932	-0.965791	-0.065547	0.088423	-0.112135	-0.430355
36	19	0.439820	-0.970925	-0.125467	0.007657	-0.089254	-0.447477
36	29	0.234428	-1.180620	-0.031647	0.303739	0.034457	-0.538167
37	26	0.742352	-0.833359	-0.012137	0.360128	0.026002	-1.102480
37	27	0.667920	-0.872408	0.070190	0.144582	0.062696	-0.812501
37	28	0.610315	-0.906095	0.063396	0.151985	-0.033509	-0.762299
38	18	0.535579	-0.932149	0.075580	0.074170	-0.146569	-0.609748
38	20	0.629610	-0.892841	-0.069212	0.124948	-0.105764	-0.754558
40	19	0.272708	-1.096618	-0.251349	-0.110942	-0.451659	-0.161767

APPENDIX C: RSTRESS DILATION AND SLIP TENDENCY VERIFICATION

Verification 1: Eigenvectors values and directions using Mathematica®

Fault Dilation Tendency Code Validation

Eigenvectors and Eigenvalues

SATSI Input for col 1, row 17 of SGB_satsi.output_stress_fits

```
s = {{1.03191, -0.555664, -0.0425700}, {-0.555664, 0.148991, 0.03818100}, {-0.04245700, 0.03818100, -1.18090}}
```

```
{{1.03191, -0.555664, -0.04257}, {-0.555664, 0.148991, 0.038181}, {-0.042457, 0.038181, -1.1809}}
```

```
v = Eigenvectors[s]
```

```
{{0.900243, -0.434828, -0.0220863}, {0.013431, -0.0230626, 0.999644}, {-0.435184, -0.900217, -0.014968}}
```

```
MatrixForm[v]
```

$$\begin{pmatrix} 0.9002428726064794` & -0.4348275100596724` & -0.022086349099380245` \\ 0.013431005335088888` & -0.023062643935186745` & 0.9996437978352126` \\ -0.4351842654723793` & -0.9002169823018789` & -0.014967961135853644` \end{pmatrix}$$

Output from Fortran DT code

$$f = \begin{pmatrix} 0.900243 & -0.434828 & -0.02208633 \\ 0.435183 & 0.900218 & 0.01496799 \\ 0.01337401 & -0.02308642 & 0.999644 \end{pmatrix}$$

```
e = Eigenvalues[s]
```

```
{1.30135, -1.18235, -0.118994}
```

Output from Fortran DT code

```
g = {1.30135, -0.118993, -1.18235}
```

```
{1.30135, -0.118993, -1.18235}
```

Extract Eigenvectors

```
v1 = {Extract[v, {1, 1}], Extract[v, {1, 2}], Extract[v, {1, 3}]}
```

```
{0.900243, -0.434828, -0.0220863}
```

```
v2 = {Extract[v, {2, 1}], Extract[v, {2, 2}], Extract[v, {2, 3}]}
```

```
{0.013431, -0.0230626, 0.999644}
```

```
v3 = {Extract[v, {3, 1}], Extract[v, {3, 2}], Extract[v, {3, 3}]}
```

```
{-0.4351842654723793`, -0.9002169823018789`, -0.014967961135853644`}
```

Check that Eigenvectors are orthogonal

```
Needs["VectorAnalysis`"]
```

```
General::obspkg: VectorAnalysis` is now obsolete. The legacy version being loaded may conflict with current functionality. See the Compatibility Guide for updating information.
DotProduct::shdw: Symbol DotProduct appears in multiple contexts {VectorAnalysis`, Global`}; definitions in context VectorAnalysis` may shadow or be shadowed by other definitions. >>
```

```
DotProduct[v1, v2]
```

```
0.000040957
```

```
DotProduct[v1, v3]
```

-1.83672×10^{-6}

```
DotProduct[v2, v3]
```

```
-0.000046208
```

```
Plot Eigenvectors

VectorPlot3D[v1, v2, v3, {x, -1, 1}, {y, -1, 1}, {z, -1, 1}, AxesLabel -> {x, y, z}]

VectorPlot3D::monopt : Options expected (instead of {z, -1, 1}) beyond position 4 in VectorPlot3D[v1, v2, v3, {x, -1, 1}, {y, -1, 1}, {z, -1, 1}, AxesLabel → {x, y, z}]. An option must be a rule or a list of rules. >>

VectorPlot3D[v1, {x, -1, 1}, {y, -1, 1}, {z, -1, 1}, AxesLabel → {x, y, z}]
```

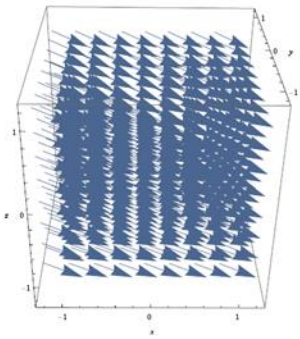


```
theta = ArcTan[Extract[v, {1, 2}] / Extract[v, {1, 1}]] * 180 / π

-25.7811

phi = ArcCos[Extract[v, {1, 3}] / √(Extract[v, {1, 1}]^2 + Extract[v, {1, 2}]^2 + Extract[v, {1, 3}]^2)] * 180 / π

91.2656

VectorPlot3D[v2, {x, -1, 1}, {y, -1, 1}, {z, -1, 1}, AxesLabel → {x, y, z}]
```

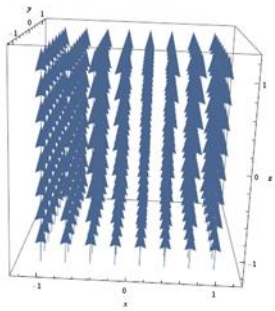


```
theta = ArcTan[Extract[v, {2, 2}] / Extract[v, {2, 1}]] * 180 / π

-59.7847

hi = ArcCos[Extract[v, {2, 3}] / √(Extract[v, {2, 1}]^2 + Extract[v, {2, 2}]^2 + Extract[v, {2, 3}]^2)] * 180 / π

1.52932

VectorPlot3D[v3, {x, -1, 1}, {y, -1, 1}, {z, -1, 1}, AxesLabel → {x, y, z}]
```

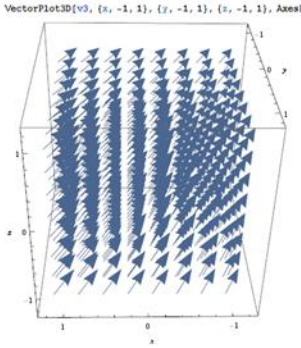


```
theta = ArcTan[Extract[v, {3, 2}] / Extract[v, {3, 1}]] * 180 / π

64.1999

ArcCos[Extract[v, {3, 3}] / √(Extract[v, {3, 1}]^2 + Extract[v, {3, 2}]^2 + Extract[v, {3, 3}]^2)] * 180 / π

90.8576
```

Verification 2: Components of normal and shear stresses, dilation and shear tendencies for 7 fault plane orientations and normal, reverse, and strike-slip faulting regimes

```
!=================================================================
! Code testing results for reverse, strike-slip and normal faulting regimes - 6/10/15
! text extracted directly from Fortran code documentation
!
! 15, 12, 5 MPa principal stresses (reverse faulting regime)
! strike and dip values are in degrees
! sigma_s = shear component of stress, sigma_n is normal component of stress
! dt and st are dilation tendency and shear tendency
!=================================================================!
strike = 0., dip = 90., sigma_n = 15, dt = 0.00, sigma_s = 0, st = 0.00
! strike = 90., dip = 90., sigma_n = 12, dt = 0.30, sigma_s = 0, st = 0.00
! strike = 0, dip = 0., sigma_n = 15, dt = 0.00, sigma_s = 0, st = 0.00
! strike = 90., dip = 0., sigma_n = 5, dt = 1.00, sigma_s = 0, st = 0.00
! strike = 45., dip = 90., sigma_n = 13.5, dt = 0.15, sigma_s = 1.5, st = 0.11
! strike = 0., dip = 45., sigma_n = 10, dt = 0.50, sigma_s = 5, st = 0.50
! strike = 90., dip = 45., sigma_n = 8.5, dt = 0.65, sigma_s = 3.5, st = 0.41
!
! 15, 5, 12 MPa principal stresses 6/10/15 (strike-slip faulting regime)
!
=================================================================
====
! strike = 0., dip = 90., sigma_n = 15, dt = 0.00, sigma_s = 0, st = 0.00
! strike = 90., dip = 90., sigma_n = 5, dt = 1.00, sigma_s = 0, st = 0.00
! strike = 0, dip = 0., sigma_n = 12, dt = 0.30, sigma_s = 0, st = 0.00
! strike = 90., dip = 0., sigma_n = 12, dt = 0.30, sigma_s = 0, st = 0.00
! strike = 45., dip = 90., sigma_n = 10, dt = 0.50, sigma_s = 5, st = 0.50
! strike = 0., dip = 45., sigma_n = 13.5, dt = 0.15, sigma_s = 1.5, st = 0.11
! strike = 90., dip = 45., sigma_n = 8.5, dt = 0.65, sigma_s = 3.5, st = 0.41
!
! 12, 5, 15 MPa principal stresses 6/10/15 (normal faulting regime)
!
=================================================================
====
! strike = 0., dip = 90., sigma_n = 12, dt = 0.30, sigma_s = 0, st = 0.00
! strike = 90., dip = 90., sigma_n = 5, dt = 1.00, sigma_s = 0, st = 0.00
! strike = 0, dip = 0., sigma_n = 15, dt = 0.00, sigma_s = 0, st = 0.00
! strike = 90., dip = 0., sigma_n = 15, dt = 0.00, sigma_s = 0, st = 0.00
! strike = 45., dip = 90., sigma_n = 8.5, dt = 0.65, sigma_s = 3.5, st = 0.41
! strike = 0., dip = 45., sigma_n = 13.5, dt = 0.15, sigma_s = 1.5, st = 0.11
! strike = 90., dip = 45., sigma_n = 10, dt = 0.50, sigma_s = 5, st = 0.50
!
! 17, 11, 21 MPa principal stresses 6/10/15 (normal faulting regime)
! (Stock et al., 1985)
!=================================================================
! strike = 0., dip = 90., sigma_n = 17, dt = 0.40, sigma_s = 0, st = 0.00
! strike = 90., dip = 90., sigma_n = 5, dt = 1.00, sigma_s = 0, st = 0.00
! strike = 0, dip = 0., sigma_n = 21, dt = 0.00, sigma_s = 0, st = 0.00
! strike = 90., dip = 0., sigma_n = 21, dt = 0.00, sigma_s = 0, st = 0.00
! strike = 45., dip = 90., sigma_n = 14, dt = 0.70, sigma_s = 3, st = 0.21
! strike = 0., dip = 45., sigma_n = 19, dt = 0.20, sigma_s = 2, st = 0.11
```

! strike = 90., dip = 45., sigma_n = 16, dt = 0.50, sigma_s = 5, st = 0.31
! Note that dilation and slip tendency range and direction is in agreement with Ferrill *et al.* (1999)
! "Stressed Rock Strains Groundwater at Yucca Mountain, Nevada", GSA Today, 9(5), 1-8.
!
! conclusions:
! => All stresses are acting perpendicular to axes, i.e., If SHmax = x, strike = 0., dip = 90.,
! sigma_n = SHmax.
! => Rotate all fault orientations relative to SHmax rotation from x-axis (average N37degE)
! => Stress balance (normal + shear) verifies computation of shear stress at off-diagonal strikes/dips
! => Max slip tendency is in agreement with Anderson classification scheme
!==========

Verification 3: Spatial trends and values of Ferrill *et al.* (1999)

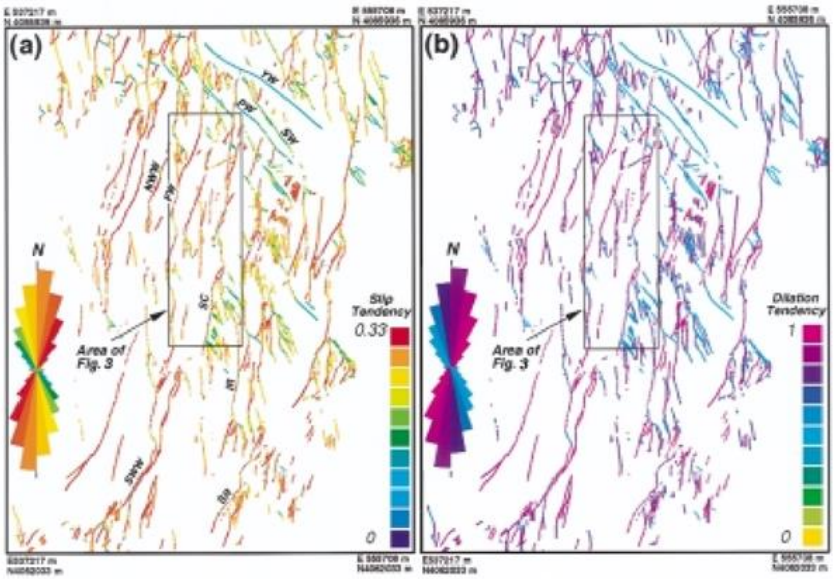

Figure 4. (a) Slip tendency map of Yucca Mountain faults mapped by Simonds et al. (1995). The rose diagram shows cumulative fault length in 10° strike azimuth bins. The map and rose diagram are colored according to slip tendency as shown by the slip-tendency plot and the color bar in Figure 3b. The area is as shown in Figure 1. Named faults discussed in the text are labeled on the map: NWW—Northern Windy Wash, SWW—Southern Windy Wash, FW—Fatigue Wash, SC—Solitario Canyon, IR—Iron Ridge, SR—Stagecoach Road, PW—Pagany Wash, SW—Sever Wash, and YW—Yucca Wash. (b) Dilation tendency map of Yucca Mountain faults. The map and rose diagram are colored according to dilation tendency as shown by the dilation-tendency plot and color bar in Figure 3c. The area is as shown in Figure 1.

Figure C-1. Figure from Ferrill *et al.* (1999) using Stock *et al.* (1985) stress field to compute (a) slip tendency and (b) dilation tendency. Note the similarity in spatial trends with Figures 23 and 24 (slip tendency) and Figures 16 and 17 (dilation tendency) for PM Phase II faults.

Verification 4: Stereonet projections of dilation and slip tendency

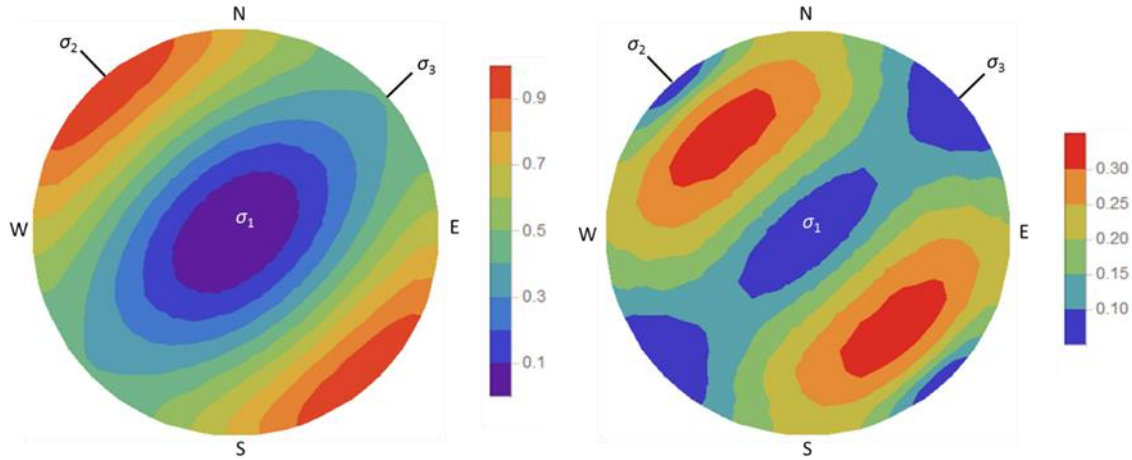

Figure C-2. Southern-hemisphere, equal-area stereonet plot of poles to planes of dilation tendency (left) and slip tendency (right) for average Pahute Mesa stress field directions (S_{Hmax} = N42˚E) and Stock *et al.* (1985) stress magnitudes. Note that the maximum dilation and slip tendency values of 1.0 and 0.33, respectively, are in agreement with the maximum dilation and slip tendency computed at Yucca Mountain by Ferrill *et al.* (1999).

Verification 5: Mapping dilation and slip tendency values onto fault map

Mapping dilation and slip tendency values for the total 15,625 fault segments onto the combined NSTec (2014) PM Phase II and Slate *et al.* (1999) fault map for a constant (average) stress field orientation provides a verification check on: (1) the process of correctly digitizing the 394 faults into 100 m long segments, (2) RStress accurately both reads and outputs the digitized fault segments, (3) RStress does not erroneously assign zero or NaN values to fault segments (i.e., all of the faults are covered by dilation and slip tendency values), and (4) visual confirmation that faults of similar strike are consistently assigned consistent values of dilation and slip tendency.

Figure C-3. Values of dilation tendency plotted on top of combined fault map. Note perfect correspondence between fault map and dilation tendency segments.

Figure C-4. Second figure: Values of slip tendency plotted on top of combined fault map. Note perfect correspondence between fault map and slip tendency segments.

APPENDIX D: COMPILED DILATION AND SLIP TENDENCY VALUES

This appendix contains dilation and slip tendency values for large-scale faults (Table D1) and background fractures (Tables D2-D8). The dilation and slip tendency values reported represent the average computed from spatially varying and average horizontal stress directions. Faults and fractures enhanced for fluid flow are bolded. Values of *H* listed in Tables D2-D8 represent the vertical distance of the fracture in the borehole according to Equation (12).

Table D-1. Average dilation and tendency values for all faults and structures shown in Figure 12.

Faults	**Symbol**	**Dilation Tendency**			**Slip Tendency**		
		1.5	**2.5**	**3.2**	**1.5**	**2.5**	**3.2**
ER-20-7 Fault	20_7	**0.80**	0.76	0.76	0.21	0.45	0.57
ER-20-8 Fault	20_8	**0.94**	**0.94**	**0.93**	0.18	0.40	0.54
Almendro	AL	**0.84**	**0.81**	**0.81**	0.20	0.43	0.57
Ammonia Tanks caldera structural margin	ATCSM	0.64	0.58	0.57	0.16	0.32	0.40
Big Burn Valley fault	BBV	0.61	0.54	0.52	0.15	0.28	0.35
Bare Mountain fault	BM	0.75	0.70	0.69	0.22	0.44	0.55
Black Mountain Caldera structural margin	BMCSM	0.67	0.61	0.60	0.17	0.34	0.43
Buteo	BU	0.77	0.73	0.73	0.20	0.41	0.52
Beatty Wash fault	BW	0.73	0.68	0.67	0.20	0.39	0.49
Boxcar fault	BX	**0.82**	0.79	0.78	0.21	0.45	0.58
Claim Canyon Caldera structural margin	CCCSM	0.67	0.61	0.59	0.16	0.31	0.39
Colson Pond Fault	CPF	0.64	0.58	0.57	0.22	0.40	0.48
East Estuary fault	EE	0.63	0.56	0.54	0.18	0.35	0.43
East Greeley fault	EG	0.70	0.64	0.63	0.21	0.42	0.52
East Thirsty Canyon structural zone	ETCSZ	0.74	0.69	0.69	0.23	0.46	0.56
Fleur-de-Lis fault	FDL	0.63	0.57	0.55	0.22	0.40	0.48
Grouse Canyon Caldera Margin	GCCSMNW	**0.85**	**0.82**	**0.82**	0.18	0.40	0.52
Handley fault	HA	**0.92**	**0.91**	**0.91**	0.19	0.42	0.56
Hogback fault	HOG	0.73	0.68	0.67	0.22	0.44	0.54
Hot Springs Lineament	HSL	0.64	0.57	0.56	0.22	0.40	0.48
Moat Fault #10	M10	0.75	0.70	0.69	0.23	0.47	0.58
Moat Fault #14	M14	0.54	0.45	0.43	0.15	0.27	0.31
Moat Fault #19	M19	0.58	0.51	0.49	0.20	0.35	0.42
Moat Fault #2	M2	0.68	0.63	0.61	0.22	0.43	0.52
Moat Fault #22	M22	**0.84**	**0.81**	**0.81**	0.21	0.45	0.58
Moat Fault #23	M23	**0.92**	**0.91**	**0.91**	0.19	0.41	0.56

Table D-1. Average dilation and tendency values for all faults and structures shown in Figure 12 (continued).

Faults	Symbol	Dilation Tendency			Slip Tendency		
		1.5	**2.5**	**3.2**	**1.5**	**2.5**	**3.2**
Moat Fault #24	M24	0.77	0.73	0.72	0.23	0.47	**0.60**
Moat Fault #25	M25	0.72	0.67	0.66	0.22	0.44	0.55
Moat Fault #26	M26	0.63	0.57	0.55	0.21	0.39	0.47
Moat Fault #27	M27	0.72	0.67	0.66	0.23	0.46	0.56
Moat Fault #28	M28	0.73	0.68	0.67	0.23	0.46	0.56
Moat Fault #29	M29	0.73	0.68	0.67	0.23	0.46	0.56
M3 Fault	M3	0.72	0.67	0.65	0.23	0.45	0.56
Moat Fault #30	M30	0.71	0.66	0.64	0.22	0.43	0.53
Moat Fault #31	M31	0.76	0.73	0.72	0.21	0.44	0.56
Moat Fault #32	M32	0.76	0.72	0.71	0.22	0.46	0.58
Moat Fault #33	M33	0.71	0.66	0.65	0.23	0.44	0.55
Moat Fault #4	M4	0.66	0.60	0.58	0.21	0.40	0.49
M5N	M5N	**0.80**	0.77	0.76	0.23	0.48	**0.61**
M5S	M5S	0.75	0.71	0.70	0.23	0.46	0.57
Moat Fault #6	M6	0.59	0.51	0.50	0.17	0.32	0.38
Moor Hen Meadow structural zone	MHMSZ	0.51	0.42	0.39	0.16	0.27	0.31
Northern Timber Moat structural zone	NTMMSZ	0.45	0.35	0.32	0.11	0.19	0.22
Pah Canyon fault	PAH	0.57	0.49	0.47	0.16	0.30	0.36
Paintbrush Canyon fault	PC	0.63	0.56	0.55	0.21	0.39	0.47
Paintbrush Canyon Fault North	PCN	0.43	0.32	0.29	0.10	0.15	0.17
Purse fault	PU	0.75	0.70	0.69	0.21	0.43	0.54
Rainier Mesa 3	RaM3	0.75	0.71	0.70	0.20	0.41	0.51
Rainier Mesa 4	RaM4	**0.89**	**0.87**	**0.87**	0.20	0.45	0.59
Ribbon Cliff structural zone	RCSZ	0.48	0.39	0.36	0.14	0.25	0.28
Resurgent Dome Fault #1	RM1	0.46	0.36	0.34	0.11	0.19	0.22
Resurgent Dome Fault #10	RM10	**0.87**	**0.85**	**0.85**	0.20	0.43	0.57
Resurgent Dome Fault #2	RM2	0.56	0.47	0.46	0.14	0.26	0.32
Resurgent Dome Fault #4	RM4	**0.91**	**0.89**	**0.89**	0.19	0.42	0.56
Resurgent Dome Fault #5	RM5	0.58	0.49	0.48	0.17	0.31	0.37
Resurgent Dome Fault #6	RM6	0.54	0.46	0.44	0.16	0.28	0.33
Resurgent Dome Fault #7	RM7	0.52	0.43	0.41	0.14	0.25	0.29
Resurgent Dome Fault #9	RM9	0.59	0.52	0.51	0.15	0.28	0.35

Table D-1. Average dilation and tendency values for all faults and structures shown in Figure 12 (continued).

Faults	Symbol	Dilation Tendency			Slip Tendency		
		1.5	**2.5**	**3.2**	**1.5**	**2.5**	**3.2**
Rainier Mesa caldera structural margin	RMCSM	0.74	0.69	0.68	0.20	0.40	0.51
Redrock Valley Caldera structural margin	RRVSM	**0.82**	0.79	0.79	0.20	0.42	0.55
Rickey fault	RY	0.77	0.74	0.73	0.22	0.45	0.57
Silent Canyon Northern structural zone	SCNSZ	0.52	0.44	0.42	0.17	0.29	0.34
Silent Canyon structural zone - east	SCSZE	0.48	0.39	0.36	0.13	0.22	0.26
Silent Canyon structural zone - west	SCSZW	0.50	0.41	0.38	0.15	0.25	0.30
Shoshone Mountain 10	SM10	0.74	0.69	0.68	0.21	0.43	0.54
Shoshone Mountain 20	SM20	0.73	0.68	0.67	0.21	0.41	0.52
Shoshone Mountain 30	SM30	**0.85**	**0.83**	**0.82**	0.20	0.43	0.56
Shoshone Mountain 6	SM6	**0.83**	**0.80**	**0.80**	0.23	0.49	**0.62**
Scrugham Peak fault	SP	0.78	0.74	0.74	0.22	0.45	0.57
Southern Pahute Mesa structural zone	SPMSZ	0.59	0.52	0.50	0.19	0.35	0.42
Split Ridge fault	SR	0.72	0.67	0.66	0.21	0.42	0.52
Southwest Area 20 caldera margin	SWA20CSM Southwest Area 20 caldera margin	0.64	0.57	0.56	0.15	0.30	0.38
West Almendro	WAL	0.66	0.59	0.58	0.20	0.37	0.46
West Boxcar fault	WB	0.60	0.53	0.51	0.19	0.35	0.42
West Estuary fault	WE	0.71	0.66	0.64	0.21	0.41	0.51
West Greeley fault	WG	0.79	0.76	0.75	0.21	0.43	0.55
West Purse fault	WP	0.74	0.70	0.69	0.23	0.46	0.57
West Silent Canyon structural zone	WSCSZ	0.51	0.42	0.40	0.16	0.28	0.32
Windy Wash fault	WW	0.79	0.75	0.74	0.21	0.44	0.57
S1	S1	0.54	0.45	0.43	0.17	0.30	0.35
S2	S2	**0.88**	**0.86**	**0.86**	0.20	0.45	0.59
S3	S3	0.57	0.50	0.48	0.18	0.33	0.40
S4	S4	**0.89**	**0.88**	**0.87**	0.21	0.46	**0.61**
S5	S5	0.67	0.61	0.60	0.20	0.38	0.47
S6	S6	0.68	0.62	0.61	0.23	0.43	0.52
S7	S7	**0.94**	**0.93**	**0.93**	0.19	0.42	0.58
S8	S8	**0.95**	**0.95**	**0.95**	0.17	0.39	0.54
S9	S9	**0.81**	0.78	0.77	0.21	0.44	0.57
S10	S10	0.68	0.62	0.61	0.22	0.42	0.52
S11	S11	**0.95**	**0.95**	**0.95**	0.17	0.39	0.53
S12	S12	0.60	0.53	0.51	0.20	0.37	0.44

Table D-1. Average dilation and tendency values for all faults and structures shown in Figure 12 (continued).

Faults	Symbol	Dilation Tendency			Slip Tendency		
		1.5	**2.5**	**3.2**	**1.5**	**2.5**	**3.2**
S13	S13	0.67	0.61	0.60	0.22	0.43	0.52
S14	S14	0.54	0.46	0.44	0.17	0.29	0.34
S15	S15	0.79	0.76	0.75	0.23	0.48	**0.61**
S16	S16	**0.91**	**0.89**	**0.89**	0.20	0.44	0.59
S17	S17	**0.95**	**0.95**	**0.95**	0.18	0.39	0.53
S18	S18	**0.91**	**0.89**	**0.89**	0.20	0.44	0.59
S19	S19	0.56	0.48	0.46	0.18	0.31	0.37
S20	S20	0.70	0.65	0.63	0.22	0.43	0.53
S21	S21	**0.80**	0.76	0.76	0.20	0.41	0.52
S22	S22	0.69	0.64	0.62	0.23	0.44	0.53
S23	S23	0.50	0.40	0.38	0.15	0.26	0.30
S24	S24	0.76	0.71	0.70	0.21	0.42	0.54
S25	S25	**0.87**	**0.84**	**0.84**	0.22	0.48	**0.63**
S26	S26	0.75	0.71	0.70	0.23	0.47	0.59
S27	S27	**0.91**	**0.89**	**0.89**	0.21	0.47	**0.63**
S28	S28	0.73	0.68	0.67	0.21	0.42	0.53
S29	S29	0.55	0.47	0.45	0.18	0.32	0.37
S30	S30	**0.94**	**0.93**	**0.92**	0.19	0.43	0.57
S31	S31	0.68	0.62	0.61	0.22	0.41	0.50
S32	S32	0.76	0.72	0.71	0.22	0.45	0.56
S33	S33	0.59	0.52	0.50	0.19	0.35	0.42
S34	S34	0.74	0.70	0.69	0.22	0.43	0.55
S35	S35	0.53	0.44	0.42	0.17	0.29	0.34
S36	S36	0.71	0.66	0.65	0.20	0.40	0.50
S37	S37	0.69	0.63	0.62	0.18	0.35	0.45
S38	S38	**0.96**	**0.95**	**0.95**	0.17	0.38	0.52
S39	S39	0.52	0.43	0.41	0.16	0.28	0.32
S40	S40	0.75	0.71	0.70	0.18	0.37	0.47
S41	S41	0.72	0.67	0.66	0.22	0.44	0.54
S42	S42	0.78	0.74	0.73	0.23	0.47	0.59
S43	S43	0.48	0.38	0.36	0.13	0.22	0.26
S44	S44	**0.95**	**0.94**	**0.94**	0.17	0.38	0.52
S45	S45	0.74	0.69	0.68	0.21	0.43	0.54
S46	S46	0.63	0.57	0.55	0.20	0.38	0.46
S47	S47	0.75	0.70	0.69	0.23	0.47	0.58
S48	S48	**0.83**	**0.80**	**0.80**	0.23	0.48	**0.62**
S49	S49	0.79	0.75	0.75	0.22	0.45	0.57
S50	S50	0.73	0.68	0.67	0.18	0.36	0.47

Table D-1. Average dilation and tendency values for all faults and structures shown in Figure 12 (continued).

Faults	Symbol	Dilation Tendency			Slip Tendency		
		1.5	**2.5**	**3.2**	**1.5**	**2.5**	**3.2**
S51	S51	0.60	0.52	0.50	0.17	0.31	0.38
S52	S52	0.64	0.58	0.57	0.22	0.41	0.49
S53	S53	0.71	0.66	0.65	0.22	0.44	0.55
S54	S54	0.77	0.73	0.72	0.23	0.47	0.59
S55	S55	0.73	0.68	0.67	0.23	0.46	0.56
S56	S56	0.58	0.50	0.48	0.17	0.32	0.39
S57	S57	**0.83**	**0.80**	**0.80**	0.23	0.48	**0.62**
S58	S58	**0.82**	0.78	0.78	0.22	0.45	0.58
S59	S59	0.73	0.68	0.67	0.22	0.44	0.54
S60	S60	**0.89**	**0.88**	**0.87**	0.21	0.46	**0.60**
S61	S61	**0.85**	**0.83**	**0.82**	0.22	0.48	**0.62**
S62	S62	0.75	0.71	0.70	0.23	0.48	0.59
S63	S63	**0.80**	0.77	0.76	0.23	0.48	**0.60**
S64	S64	**0.87**	**0.85**	**0.85**	0.22	0.48	**0.63**
S65	S65	**0.90**	**0.89**	**0.89**	0.20	0.46	**0.61**
S66	S66	**0.92**	**0.91**	**0.90**	0.19	0.44	0.59
S67	S67	0.73	0.69	0.67	0.22	0.43	0.53
S68	S68	0.41	0.30	0.28	0.07	0.10	0.11
S69	S69	**0.84**	**0.81**	**0.81**	0.22	0.47	**0.60**
S70	S70	0.64	0.57	0.55	0.20	0.38	0.46
S71	S71	0.43	0.32	0.30	0.09	0.14	0.16
S72	S72	0.72	0.67	0.66	0.21	0.42	0.52
S73	S73	0.68	0.62	0.61	0.22	0.43	0.52
S74	S74	0.54	0.45	0.43	0.16	0.28	0.34
S75	S75	0.62	0.55	0.53	0.20	0.37	0.45
S76	S76	0.46	0.36	0.34	0.12	0.20	0.23
S77	S77	0.69	0.64	0.62	0.21	0.41	0.51
S78	S78	**0.93**	**0.93**	**0.93**	0.19	0.41	0.56
S79	S79	0.73	0.69	0.67	0.22	0.43	0.54
S80	S80	0.41	0.30	0.28	0.08	0.12	0.14
S81	S81	0.69	0.63	0.62	0.22	0.43	0.52
S82	S82	0.61	0.54	0.52	0.19	0.36	0.43
S83	S83	0.76	0.72	0.71	0.22	0.46	0.57
S84	S84	**0.81**	0.78	0.78	0.20	0.41	0.53
S85	S85	0.59	0.51	0.49	0.18	0.32	0.39
S86	S86	0.73	0.69	0.67	0.23	0.46	0.57
S87	S87	0.71	0.66	0.65	0.21	0.41	0.52
S88	S88	0.73	0.68	0.66	0.21	0.42	0.52

Table D-1. Average dilation and tendency values for all faults and structures shown in Figure 12 (continued).

Faults	Symbol	Dilation Tendency			Slip Tendency		
		1.5	2.5	3.2	1.5	2.5	3.2
S89	S89	0.78	0.74	0.73	0.23	0.47	0.59
S90	S90	**0.89**	**0.88**	**0.87**	0.20	0.44	0.58
S91	S91	**0.89**	**0.87**	**0.87**	0.19	0.42	0.55
S92	S92	0.74	0.69	0.68	0.23	0.47	0.57
S93	S93	**0.83**	**0.80**	**0.80**	0.21	0.45	0.58
S94	S94	0.79	0.75	0.75	0.20	0.42	0.54
S95	S95	**0.95**	**0.94**	**0.94**	0.18	0.39	0.54
S96	S96	0.79	0.75	0.74	0.23	0.47	**0.60**
S97	S97	0.79	0.75	0.74	0.23	0.49	**0.61**
S98	S98	0.76	0.72	0.71	0.22	0.46	0.57
S99	S99	**0.81**	0.78	0.77	0.22	0.46	0.59
S100	S100	0.71	0.66	0.65	0.22	0.44	0.54
S101	S101	**0.89**	**0.87**	**0.87**	0.20	0.43	0.57
S102	S102	**0.86**	**0.84**	**0.84**	0.22	0.49	**0.64**
S103	S103	0.78	0.74	0.74	0.23	0.48	**0.60**
S104	S104	0.44	0.33	0.31	0.10	0.16	0.19
S105	S105	**0.80**	0.77	0.76	0.23	0.49	**0.62**
S106	S106	**0.92**	**0.92**	**0.92**	0.19	0.42	0.56
S107	S107	0.75	0.71	0.70	0.22	0.45	0.56
S108	S108	**0.80**	0.76	0.75	0.21	0.43	0.55
S109	S109	0.70	0.64	0.63	0.22	0.43	0.52
S110	S110	**0.86**	**0.84**	**0.83**	0.21	0.44	0.57
S111	S111	**0.81**	0.78	0.77	0.23	0.47	**0.60**
S112	S112	0.78	0.74	0.73	0.22	0.46	0.58
S113	S113	0.74	0.69	0.68	0.23	0.46	0.56
S114	S114	0.75	0.71	0.70	0.23	0.46	0.58
S115	S115	**0.85**	**0.83**	**0.82**	0.21	0.46	0.59
S116	S116	**0.88**	**0.87**	**0.86**	0.21	0.46	**0.61**
S117	S117	**0.80**	0.77	0.76	0.22	0.47	**0.60**
S118	S118	**0.86**	**0.84**	**0.83**	0.21	0.45	0.59
S119	S119	**0.82**	0.79	0.78	0.23	0.49	**0.62**
S120	S120	**0.81**	0.78	0.77	0.22	0.46	0.58
S121	S121	**0.89**	**0.87**	**0.87**	0.21	0.48	**0.63**
S122	S122	**0.81**	0.78	0.77	0.21	0.43	0.55
S123	S123	0.48	0.38	0.36	0.13	0.22	0.26
S124	S124	0.61	0.53	0.52	0.20	0.37	0.44
S125	S125	0.71	0.66	0.65	0.22	0.44	0.55
S126	S126	0.71	0.66	0.64	0.19	0.38	0.48

Table D-1. Average dilation and tendency values for all faults and structures shown in Figure 12 (continued).

Faults	Symbol	Dilation Tendency			Slip Tendency		
		1.5	**2.5**	**3.2**	**1.5**	**2.5**	**3.2**
S127	S127	0.59	0.52	0.50	0.17	0.32	0.39
S128	S128	0.55	0.46	0.45	0.18	0.31	0.36
S129	S129	0.79	0.75	0.74	0.22	0.47	0.59
S130	S130	**0.87**	**0.85**	**0.84**	0.20	0.44	0.57
S131	S131	0.70	0.65	0.64	0.22	0.44	0.54
S132	S132	0.70	0.65	0.63	0.22	0.43	0.53
S133	S133	**0.82**	0.79	0.78	0.22	0.48	**0.61**
S134	S134	**0.84**	**0.81**	**0.80**	0.20	0.42	0.54
S135	S135	0.65	0.59	0.58	0.21	0.40	0.48
S136	S136	0.78	0.74	0.73	0.21	0.43	0.54
S137	S137	0.73	0.68	0.66	0.22	0.43	0.53
S138	S138	0.64	0.57	0.55	0.19	0.37	0.45
S139	S139	0.74	0.70	0.69	0.22	0.45	0.57
S140	S140	**0.86**	**0.84**	**0.83**	0.21	0.46	**0.60**
S141	S141	**0.84**	**0.81**	**0.81**	0.22	0.47	**0.61**
S142	S142	**0.83**	0.79	0.79	0.22	0.47	**0.60**
S143	S143	0.76	0.71	0.70	0.22	0.45	0.56
S144	S144	0.67	0.61	0.59	0.21	0.39	0.48
S145	S145	0.64	0.57	0.56	0.20	0.38	0.47
S146	S146	0.73	0.68	0.67	0.23	0.46	0.56
S147	S147	**0.96**	**0.96**	**0.96**	0.17	0.38	0.52
S148	S148	**0.85**	**0.83**	**0.82**	0.21	0.45	0.59
S149	S149	**0.94**	**0.93**	**0.93**	0.18	0.41	0.56
S150	S150	**0.82**	0.79	0.79	0.22	0.47	**0.61**
S151	S151	**0.88**	**0.86**	**0.86**	0.21	0.46	**0.60**
S152	S152	**0.85**	**0.83**	**0.82**	0.23	0.48	**0.63**
S153	S153	0.77	0.74	0.73	0.22	0.45	0.56
S154	S154	**0.88**	**0.86**	**0.86**	0.19	0.41	0.55
S155	S155	0.61	0.53	0.52	0.20	0.37	0.44
S156	S156	**0.88**	**0.86**	**0.85**	0.21	0.46	**0.60**
S157	S157	**0.80**	0.77	0.76	0.23	0.48	**0.60**
S158	S158	0.76	0.72	0.71	0.22	0.45	0.56
S159	S159	**0.90**	**0.89**	**0.88**	0.20	0.44	0.59
S160	S160	0.77	0.74	0.73	0.22	0.45	0.57
S161	S161	**0.83**	**0.80**	0.79	0.19	0.40	0.52
S162	S162	0.78	0.74	0.73	0.23	0.47	0.59
S163	S163	0.76	0.72	0.72	0.21	0.44	0.55
S164	S164	0.68	0.63	0.61	0.22	0.42	0.52

Table D-1. Average dilation and tendency values for all faults and structures shown in Figure 12 (continued).

Faults	Symbol	Dilation Tendency			Slip Tendency		
		1.5	2.5	3.2	1.5	2.5	3.2
S165	S165	**0.97**	**0.97**	**0.97**	0.16	0.35	0.48
S166	S166	**0.91**	**0.91**	**0.90**	0.20	0.44	**0.60**
S167	S167	**0.88**	**0.86**	**0.86**	0.19	0.41	0.54
S168	S168	0.58	0.51	0.49	0.18	0.33	0.40
S169	S169	0.75	0.70	0.69	0.21	0.43	0.54
S170	S170	**0.87**	**0.85**	**0.84**	0.21	0.44	0.58
S171	S171	**0.96**	**0.96**	**0.96**	0.16	0.37	0.50
S172	S172	**0.82**	0.79	0.79	0.22	0.47	**0.60**
S173	S173	0.72	0.67	0.66	0.22	0.44	0.55
S174	S174	**0.94**	**0.94**	**0.93**	0.18	0.40	0.55
S175	S175	**0.81**	0.78	0.77	0.20	0.41	0.53
S176	S176	0.73	0.68	0.67	0.22	0.45	0.56
S177	S177	**0.84**	**0.81**	**0.80**	0.22	0.48	**0.62**
S178	S178	0.49	0.39	0.37	0.14	0.24	0.28
S179	S179	0.66	0.59	0.58	0.21	0.41	0.49
S180	S180	0.65	0.59	0.57	0.21	0.40	0.49
S181	S181	0.72	0.66	0.65	0.21	0.42	0.53
S182	S182	**0.82**	**0.80**	0.79	0.21	0.44	0.57
S183	S183	0.57	0.48	0.47	0.17	0.31	0.37
S184	S184	0.64	0.57	0.56	0.19	0.36	0.44
S185	S185	**0.88**	**0.86**	**0.86**	0.20	0.45	0.59
S186	S186	**0.95**	**0.94**	**0.94**	0.18	0.41	0.55
S187	S187	0.68	0.63	0.61	0.20	0.39	0.49
S188	S188	**0.95**	**0.95**	**0.95**	0.17	0.38	0.53
S189	S189	**0.96**	**0.96**	**0.96**	0.17	0.38	0.52
S190	S190	**0.95**	**0.94**	**0.94**	0.17	0.39	0.54
S191	S191	0.54	0.45	0.44	0.16	0.29	0.35
S192	S192	0.74	0.70	0.69	0.20	0.41	0.52
S193	S193	**0.80**	0.77	0.77	0.23	0.47	**0.60**
S194	S194	**0.87**	**0.85**	**0.85**	0.22	0.48	**0.63**
S195	S195	0.70	0.64	0.63	0.23	0.44	0.53
S196	S196	**0.90**	**0.89**	**0.89**	0.20	0.44	0.59
S197	S197	**0.91**	**0.89**	**0.89**	0.19	0.44	0.58
S198	S198	**0.91**	**0.90**	**0.89**	0.19	0.42	0.56
S199	S199	**0.95**	**0.95**	**0.95**	0.18	0.39	0.53
S200	S200	**0.88**	**0.87**	**0.86**	0.20	0.43	0.56
S201	S201	**0.95**	**0.94**	**0.94**	0.18	0.40	0.55
S202	S202	0.76	0.72	0.70	0.21	0.44	0.56

Table D-1. Average dilation and tendency values for all faults and structures shown in Figure 12 (continued).

Faults	Symbol	Dilation Tendency			Slip Tendency		
		1.5	2.5	3.2	1.5	2.5	3.2
S203	S203	**0.88**	**0.86**	**0.85**	0.20	0.44	0.58
S204	S204	**0.95**	**0.95**	**0.95**	0.17	0.39	0.53
S205	S205	0.71	0.66	0.65	0.22	0.43	0.54
S206	S206	0.56	0.48	0.46	0.18	0.32	0.38
S207	S207	**0.95**	0.95	0.95	0.17	0.38	0.52
S208	S208	**0.88**	**0.87**	**0.87**	0.21	0.45	0.59
S209	S209	**0.88**	**0.86**	**0.86**	0.20	0.43	0.56
S210	S210	0.63	0.57	0.55	0.18	0.33	0.41
S211	S211	0.47	0.37	0.35	0.11	0.19	0.22
S212	S212	**0.82**	0.79	0.78	0.22	0.47	**0.60**
S213	S213	0.43	0.32	0.29	0.10	0.16	0.17
S214	S214	0.71	0.66	0.65	0.22	0.43	0.54
S215	S215	0.51	0.41	0.40	0.15	0.27	0.31
S216	S216	**0.85**	**0.82**	**0.82**	0.22	0.48	**0.62**
S217	S217	0.60	0.52	0.51	0.20	0.36	0.43
S218	S218	**0.81**	0.78	0.77	0.23	0.49	**0.62**
S219	S219	**0.86**	**0.83**	**0.83**	0.21	0.46	0.59
S220	S220	0.41	0.30	0.28	0.08	0.11	0.12
S221	S221	0.77	0.73	0.73	0.22	0.44	0.56
S222	S222	0.51	0.41	0.39	0.14	0.25	0.29
S223	S223	**0.85**	**0.82**	**0.82**	0.21	0.46	0.59
S224	S224	0.73	0.69	0.67	0.22	0.44	0.55
S225	S225	**0.86**	**0.85**	**0.84**	0.21	0.44	0.58
S226	S226	0.40	0.29	0.27	0.06	0.09	0.11
S227	S227	0.58	0.50	0.48	0.18	0.33	0.39
S228	S228	0.44	0.33	0.31	0.10	0.16	0.18
S229	S229	0.45	0.35	0.33	0.12	0.20	0.22
S230	S230	0.51	0.42	0.40	0.16	0.28	0.32
S231	S231	0.71	0.66	0.65	0.22	0.44	0.54
S232	S232	0.68	0.62	0.61	0.22	0.43	0.52
S233	S233	0.41	0.31	0.28	0.08	0.11	0.13
S234	S234	**0.94**	**0.94**	**0.94**	0.18	0.40	0.54
S235	S235	**0.80**	0.77	0.76	0.23	0.49	**0.62**
S236	S236	**0.94**	**0.93**	**0.92**	0.19	0.42	0.57
S237	S237	0.53	0.44	0.42	0.15	0.28	0.32
S238	S238	0.48	0.38	0.36	0.13	0.22	0.25
S239	S239	**0.80**	0.77	0.76	0.23	0.48	**0.61**
S240	S240	0.48	0.38	0.36	0.12	0.21	0.24

Table D-1. Average dilation and tendency values for all faults and structures shown in Figure 12 (continued).

Faults	Symbol	Dilation Tendency			Slip Tendency		
		1.5	**2.5**	**3.2**	**1.5**	**2.5**	**3.2**
S241	S241	0.69	0.63	0.62	0.22	0.44	0.53
S242	S242	0.70	0.64	0.63	0.23	0.44	0.54
S243	S243	0.58	0.50	0.48	0.18	0.32	0.39
S244	S244	0.43	0.33	0.30	0.10	0.17	0.19
S245	S245	0.69	0.64	0.62	0.21	0.41	0.51
S246	S246	**0.95**	**0.94**	**0.94**	0.18	0.40	0.55
S247	S247	**0.97**	**0.97**	**0.97**	0.16	0.35	0.48
S248	S248	**0.94**	**0.92**	**0.92**	0.19	0.42	0.57
S249	S249	**0.95**	**0.95**	**0.95**	0.17	0.38	0.53
S250	S250	0.56	0.48	0.46	0.17	0.32	0.37
S251	S251	**0.86**	**0.84**	**0.83**	0.21	0.45	0.59
S252	S252	0.56	0.49	0.47	0.18	0.32	0.38
S253	S253	0.49	0.40	0.38	0.15	0.25	0.29
S254	S254	0.66	0.59	0.58	0.22	0.42	0.50
S255	S255	0.50	0.40	0.38	0.15	0.26	0.30
S256	S256	0.79	0.76	0.75	0.22	0.46	0.58
S257	S257	0.77	0.73	0.72	0.22	0.45	0.56
S258	S258	0.58	0.50	0.48	0.13	0.24	0.30
S259	S259	0.86	0.84	0.83	0.21	0.45	0.59
S260	S260	0.47	0.38	0.35	0.12	0.20	0.23
S261	S261	0.70	0.65	0.64	0.23	0.44	0.54
S262	S262	0.40	0.29	0.26	0.06	0.09	0.10
S263	S263	0.75	0.71	0.70	0.20	0.40	0.50
S264	S264	**0.94**	**0.94**	**0.93**	0.18	0.41	0.56
S265	S265	**0.88**	**0.87**	**0.87**	0.20	0.44	0.58
S266	S266	**0.94**	**0.94**	**0.94**	0.18	0.41	0.55
S267	S267	**0.86**	**0.84**	**0.83**	0.20	0.41	0.54
S268	S268	**0.86**	**0.84**	**0.83**	0.20	0.41	0.54
S269	S269	**0.81**	0.78	0.77	0.22	0.45	0.57
S270	S270	**0.91**	**0.90**	**0.90**	0.20	0.46	**0.61**
S271	S271	0.76	0.73	0.72	0.23	0.47	0.59
S272	S272	**0.90**	**0.89**	**0.88**	0.21	0.47	**0.63**
S273	S273	**0.80**	0.77	0.76	0.20	0.43	0.55
S274	S274	**0.87**	**0.85**	**0.84**	0.22	0.46	**0.61**
S275	S275	**0.84**	**0.82**	**0.81**	0.23	0.48	**0.62**
S276	S276	**0.82**	0.79	0.78	0.23	0.49	**0.63**
S277	S277	0.74	0.69	0.68	0.23	0.47	0.58
S278	S278	**0.84**	**0.81**	**0.80**	0.21	0.45	0.58

Table D-1. Average dilation and tendency values for all faults and structures shown in Figure 12 (continued).

Faults	Symbol	Dilation Tendency			Slip Tendency		
		1.5	2.5	3.2	1.5	2.5	3.2
S279	S279	0.67	0.61	0.60	0.22	0.42	0.51
S280	S280	0.76	0.71	0.70	0.23	0.46	0.57
S281	S281	**0.91**	**0.89**	**0.89**	0.20	0.43	0.58
S282	S282	**0.83**	**0.80**	0.79	0.22	0.47	**0.61**
S283	S283	0.72	0.68	0.66	0.23	0.45	0.56
S284	S284	0.63	0.56	0.55	0.21	0.39	0.47
S285	S285	**0.87**	**0.85**	**0.85**	0.22	0.48	**0.63**
S286	S286	0.55	0.47	0.45	0.17	0.30	0.36
S287	S287	0.70	0.65	0.63	0.22	0.43	0.53
S288	S288	0.65	0.58	0.57	0.22	0.41	0.49
S289	S289	0.47	0.37	0.35	0.13	0.22	0.25
S290	S290	0.58	0.50	0.48	0.19	0.35	0.41
S291	S291	0.56	0.48	0.46	0.18	0.33	0.38
S292	S292	0.79	0.75	0.74	0.23	0.48	**0.60**
S293	S293	0.55	0.48	0.46	0.18	0.32	0.38
S294	S294	0.70	0.64	0.63	0.22	0.43	0.52
S295	S295	0.40	0.28	0.26	0.06	0.08	0.08
S296	S296	**0.91**	**0.90**	**0.89**	0.19	0.41	0.55
S297	S297	**0.88**	**0.86**	**0.85**	0.21	0.46	**0.61**
S298	S298	**0.84**	**0.82**	**0.81**	0.22	0.48	**0.62**
S299	S299	**0.87**	**0.84**	**0.84**	0.21	0.46	**0.61**
S300	S300	**0.86**	**0.83**	**0.83**	0.21	0.45	0.58
S301	S301	**0.84**	**0.82**	**0.81**	0.23	0.48	**0.62**
S302	S302	0.70	0.65	0.64	0.23	0.44	0.55
S303	S303	**0.90**	**0.89**	**0.89**	0.21	0.46	**0.62**
S304	S304	**0.82**	0.78	0.78	0.22	0.46	0.59
S305	S305	**0.82**	0.78	0.77	0.22	0.46	0.58
S306	S306	0.73	0.68	0.66	0.20	0.41	0.51
S307	S307	**0.91**	**0.89**	**0.89**	0.19	0.42	0.57
S308	S308	0.69	0.63	0.62	0.22	0.43	0.52
S309	S309	**0.84**	**0.81**	**0.81**	0.21	0.45	0.58
S310	S310	**0.80**	0.77	0.76	0.22	0.46	0.58
S311	S311	0.69	0.64	0.62	0.22	0.44	0.53
S312	S312	**0.97**	**0.97**	**0.97**	0.16	0.36	0.49
S313	S313	0.79	0.76	0.75	0.23	0.48	**0.61**
S314	S314	0.76	0.73	0.72	0.22	0.45	0.57
S315	S315	**0.86**	**0.84**	**0.84**	0.21	0.46	**0.60**

Table D-2. Average dilation and slip tendency values for all fractures detected in ER-EC-1.

Depth (ft)	Depth (m)	Azimuth	Dip	Dilation Tendency			Slip Tendency			H (m)
				1.50	2.50	3.20	1.50	2.50	3.20	
2,261.70	689.37	262.136	76.8744	0.70	0.68	0.64	0.24	0.46	0.56	1.3
2,264.90	690.34	205.019	62.3208	0.75	0.75	0.75	0.31	0.58	0.71	0.6
2,268.80	**691.53**	**214.547**	**66.371**	**0.84**	**0.83**	**0.83**	**0.29**	**0.57**	**0.73**	**0.7**
2,288.60	697.57	272.705	80.5056	0.62	0.58	0.53	0.21	0.38	0.45	1.9
2,339.80	713.17	30.9362	52.2653	0.62	0.62	0.62	0.33	0.56	0.67	0.4
2,343.30	714.24	80.0981	67.6145	0.65	0.63	0.60	0.26	0.48	0.57	0.8
2,348.70	715.88	97.001	71.0471	0.53	0.49	0.44	0.20	0.35	0.40	0.9
2,372.20	723.05	59.2788	49.5833	0.55	0.55	0.54	0.31	0.52	0.61	0.4
2,458.40	749.32	93.0426	72.7846	0.58	0.54	0.49	0.22	0.38	0.45	1.0
2,461.40	750.23	99.3316	74.112	0.53	0.49	0.43	0.19	0.32	0.38	1.1
2,465.30	751.42	117.758	75.6032	0.41	0.36	0.28	0.10	0.15	0.17	1.2
2,469.50	752.70	120.24	67.9325	0.36	0.31	0.24	0.10	0.14	0.15	0.8
2,479.00	755.60	108.119	61.4883	0.38	0.34	0.29	0.16	0.24	0.27	0.6
2,482.60	756.70	105.936	73.9088	0.47	0.42	0.36	0.16	0.26	0.30	1.1
2,484.90	757.40	105.743	68.4304	0.44	0.40	0.34	0.17	0.26	0.30	0.8
2,488.00	**758.34**	**59.0187**	**69.2433**	**0.83**	**0.82**	**0.82**	**0.28**	**0.55**	**0.70**	**0.8**
2,502.90	762.88	80.7048	71.9196	0.69	0.66	0.63	0.25	0.47	0.57	1.0
2,521.00	768.40	88.1113	48.8778	0.39	0.37	0.34	0.24	0.36	0.41	0.4
2,535.30	772.76	80.7028	72.1289	0.69	0.66	0.63	0.25	0.47	0.57	1.0
2,538.70	773.80	70.5127	68.2089	0.74	0.73	0.71	0.28	0.53	0.65	0.8
2,546.50	776.17	112.463	57.1557	0.33	0.29	0.24	0.15	0.20	0.22	0.5
2,549.90	777.21	116.21	64.2274	0.36	0.31	0.25	0.13	0.17	0.19	0.6
2,558.70	**779.89**	**55.513**	**80.276**	**0.94**	**0.93**	**0.93**	**0.19**	**0.43**	**0.58**	**1.8**
2,560.90	780.56	122.516	72.4569	0.38	0.33	0.25	0.09	0.11	0.12	1.0
2,580.70	786.60	93.4771	76.4797	0.59	0.55	0.50	0.21	0.38	0.44	1.3
2,583.80	787.54	99.3906	78.4992	0.55	0.50	0.44	0.18	0.32	0.38	1.5
2,604.70	793.91	111.076	82.9352	0.47	0.41	0.34	0.12	0.21	0.24	2.5
2,607.70	794.83	101.039	83.4371	0.55	0.50	0.44	0.17	0.31	0.36	2.7
2,610.10	795.56	95.6229	82.6704	0.59	0.55	0.50	0.19	0.36	0.42	2.4
2,615.10	797.08	99.163	83.7888	0.56	0.52	0.46	0.18	0.33	0.38	2.9
2,618.80	798.21	109.809	83.6983	0.48	0.42	0.35	0.13	0.22	0.26	2.8
2,621.10	798.91	101.873	83.9582	0.54	0.49	0.43	0.17	0.30	0.35	2.9
2,621.30	798.97	107.387	62.7901	0.40	0.36	0.30	0.17	0.25	0.28	0.6
2,624.30	799.89	110.023	61.7258	0.37	0.33	0.27	0.16	0.22	0.25	0.6
2,635.70	803.36	130.471	68.7166	0.35	0.30	0.22	0.08	0.08	0.08	0.8
2,638.00	804.06	131.925	64.8862	0.33	0.28	0.21	0.09	0.09	0.09	0.7
2,638.00	804.06	115.392	80.7241	0.43	0.38	0.30	0.10	0.17	0.19	1.9
2,642.30	805.37	108.054	74.5314	0.46	0.41	0.35	0.15	0.24	0.28	1.1
2,643.70	805.80	87.1831	76.1272	0.65	0.62	0.58	0.23	0.43	0.51	1.3

Table D-2. Average dilation and slip tendency values for all fractures detected in ER-EC-1 (continued).

Depth (ft)	Depth (m)	Azimuth	Dip	Dilation Tendency			Slip Tendency			H (m)
				1.50	2.50	3.20	1.50	2.50	3.20	
2,644.80	806.14	261.728	60.8142	0.57	0.55	0.52	0.27	0.45	0.53	0.6
2,660.80	811.01	86.4536	49.064	0.40	0.38	0.36	0.24	0.37	0.43	0.4
2,663.90	811.96	93.501	50.7454	0.38	0.35	0.32	0.22	0.33	0.38	0.4
2,668.80	813.45	77.2668	83.6864	0.78	0.76	0.73	0.23	0.47	0.60	2.8
2,680.00	816.86	87.9291	46.5438	0.36	0.34	0.32	0.23	0.35	0.40	0.3
2,690.50	820.06	97.9857	61.546	0.45	0.42	0.37	0.21	0.33	0.37	0.6
2,697.50	822.20	67.0061	49.5458	0.52	0.51	0.50	0.30	0.49	0.57	0.4
2,702.70	**823.78**	**232.972**	**76.428**	**0.92**	**0.92**	**0.92**	**0.21**	**0.47**	**0.63**	**1.3**
2,714.00	827.23	262.149	73.0458	0.68	0.65	0.62	0.25	0.46	0.56	1.0
2,718.70	828.66	76.5019	76.7267	0.76	0.74	0.71	0.24	0.49	0.61	1.3
2,726.70	**831.10**	**226.668**	**82.3215**	**0.98**	**0.98**	**0.98**	**0.13**	**0.30**	**0.41**	**2.3**
2,727.00	831.19	261.564	71.4174	0.67	0.65	0.62	0.25	0.47	0.56	0.9
2,727.10	**831.22**	**64.9754**	**80.0982**	**0.88**	**0.87**	**0.85**	**0.22**	**0.49**	**0.64**	**1.8**
2,733.30	833.11	278.998	61.6689	0.44	0.41	0.36	0.20	0.32	0.36	0.6
2,733.50	**833.17**	**70.6793**	**80.0361**	**0.83**	**0.81**	**0.79**	**0.23**	**0.49**	**0.63**	**1.8**
2,733.80	833.26	263.698	62.5409	0.57	0.55	0.52	0.26	0.44	0.52	0.6
2,734.30	833.41	76.2867	80.2597	0.78	0.76	0.73	0.23	0.48	0.61	1.8
2,734.60	833.51	135.648	68.121	0.35	0.30	0.23	0.09	0.10	0.10	0.8
2,735.40	**833.75**	**245.189**	**78.7099**	**0.87**	**0.86**	**0.84**	**0.23**	**0.50**	**0.64**	**1.6**
2,745.80	836.92	267.69	64.0183	0.56	0.53	0.49	0.25	0.42	0.49	0.6
2,749.10	**837.93**	**55.1777**	**77.6032**	**0.92**	**0.92**	**0.91**	**0.21**	**0.46**	**0.62**	**1.4**
2,768.80	843.93	273.955	85.1753	0.62	0.58	0.52	0.20	0.37	0.44	3.7
2,855.90	870.48	285.255	68.3545	0.45	0.40	0.35	0.17	0.27	0.31	0.8
2,903.70	**885.05**	**68.2844**	**80.8143**	**0.86**	**0.84**	**0.82**	**0.22**	**0.49**	**0.63**	**1.9**
2,909.20	886.72	331.35	35.0931	0.16	0.14	0.12	0.13	0.17	0.18	0.2
2,910.50	887.12	337.751	50.5877	0.32	0.29	0.25	0.18	0.26	0.29	0.4
2,958.00	901.60	**63.5677**	**73.8128**	**0.84**	**0.83**	**0.82**	**0.25**	**0.52**	**0.67**	**1.1**
2,990.30	911.44	93.1943	61.6556	0.49	0.46	0.42	0.23	0.37	0.42	0.6
3,119.70	950.88	**243.629**	**74.0673**	**0.85**	**0.84**	**0.83**	**0.25**	**0.52**	**0.67**	**1.1**
3,486.90	1,062.81	290.355	72.5876	0.43	0.38	0.32	0.14	0.22	0.25	1.0
3,490.20	1,063.81	345.201	55.7656	0.41	0.38	0.34	0.21	0.33	0.37	0.5
3,492.40	1,064.48	307.15	62.7472	0.32	0.27	0.21	0.09	0.10	0.10	0.6
3,493.20	1,064.73	304.978	66.0218	0.34	0.29	0.22	0.09	0.10	0.11	0.7
3,738.30	1,139.43	274.92	65.7087	0.51	0.47	0.43	0.22	0.36	0.41	0.7
3,740.10	1,139.98	262.564	63.2346	0.59	0.57	0.54	0.26	0.45	0.53	0.6
3,807.50	1,160.53	144.194	67.6095	0.37	0.33	0.26	0.12	0.16	0.18	0.8
3,807.90	1,160.65	102.553	47.4503	0.29	0.27	0.23	0.18	0.26	0.29	0.3

Table D-2. Average dilation and slip tendency values for all fractures detected in ER-EC-1 (continued).

Depth (ft)	Depth (m)	Azimuth	Dip	Dilation Tendency			Slip Tendency			H (m)
				1.50	2.50	3.20	1.50	2.50	3.20	
3,813.50	1,162.35	99.0123	65.9369	0.48	0.44	0.39	0.20	0.32	0.37	0.7
3,815.30	1,162.90	87.5841	56.2039	0.48	0.45	0.42	0.25	0.40	0.46	0.5
3,817.00	1,163.42	69.7039	60.5451	0.66	0.65	0.63	0.30	0.53	0.63	0.6
3,844.60	1,171.83	80.4483	64.677	0.62	0.60	0.57	0.27	0.47	0.56	0.7
3,845.60	1,172.14	93.3113	68.6809	0.55	0.51	0.46	0.22	0.38	0.44	0.8
3,879.00	1,182.32	53.7337	33.1225	0.29	0.29	0.29	0.25	0.38	0.43	0.2
3,905.30	1,190.34	68.5478	46.2184	0.46	0.45	0.44	0.29	0.46	0.53	0.3
4,344.30	1,324.14	322.745	46.8889	0.23	0.20	0.16	0.12	0.15	0.16	0.3
4,345.60	1,324.54	266.173	60.4545	0.53	0.51	0.48	0.25	0.42	0.49	0.5
4,720.50	1,438.81	308.843	49.2785	0.23	0.20	0.15	0.11	0.11	0.11	0.4
4,737.10	1,443.87	351.806	51.248	0.41	0.39	0.36	0.24	0.36	0.41	0.4
4,893.40	1,491.51	39.8412	48.0809	0.56	0.56	0.56	0.32	0.54	0.63	0.3
4,894.40	1,491.81	34.8334	43.3842	0.47	0.47	0.47	0.31	0.49	0.57	0.3
4,895.30	1,492.09	38.565	44.2692	0.49	0.49	0.49	0.31	0.50	0.59	0.3
4,898.10	1,492.94	51.7318	55.495	0.67	0.67	0.66	0.32	0.57	0.69	0.5
4,958.10	**1,511.23**	**204.543**	**76.9524**	**0.91**	**0.90**	**0.90**	**0.22**	**0.48**	**0.64**	**1.3**
4,962.30	1,512.51	5.24538	20.9284	0.10	0.10	0.10	0.14	0.21	0.23	0.1

Table D-3. Average dilation and slip tendency values for all fractures detected in ER-EC-2A.

Depth (ft)	Depth (m)	Azimuth	Dip	Dilation Tendency			Slip Tendency			H
				1.50	2.50	3.20	1.50	2.50	3.20	
1,456.90	**444.06**	**21.4743**	**66.4862**	**0.80**	**0.80**	**0.79**	**0.29**	**0.57**	**0.71**	**0.7**
1,545.00	**470.92**	**233.327**	**68.9398**	**0.84**	**0.83**	**0.83**	**0.28**	**0.55**	**0.71**	**0.8**
1,567.20	**477.68**	**239.271**	**66.4871**	**0.78**	**0.77**	**0.76**	**0.29**	**0.56**	**0.70**	**0.7**
1,568.80	478.17	210.891	51.2591	0.61	0.61	0.61	0.33	0.56	0.67	0.4
1,594.90	486.13	256.194	66.3955	0.65	0.63	0.61	0.27	0.48	0.58	0.7
1,598.70	487.28	252.007	57.0592	0.58	0.56	0.55	0.29	0.49	0.58	0.5
1,607.70	490.03	39.9674	54.5503	0.67	0.67	0.66	0.33	0.58	0.70	0.4
1,859.80	566.87	305.171	68.6902	0.35	0.30	0.23	0.09	0.09	0.09	0.8
1,966.10	599.27	293.956	76.3522	0.42	0.36	0.29	0.11	0.16	0.18	1.3
2,717.80	828.39	121.524	83.3345	0.41	0.35	0.26	0.05	0.08	0.09	2.7
2,732.30	832.81	125.689	81.4026	0.40	0.34	0.26	0.04	0.05	0.06	2.1
2,741.40	835.58	105.165	77.019	0.47	0.42	0.35	0.15	0.24	0.28	1.3
2,814.40	857.83	117.504	70.8093	0.38	0.33	0.26	0.10	0.13	0.15	0.9
2,816.80	858.56	125.916	73.0255	0.37	0.32	0.24	0.07	0.07	0.08	1.0

Table D-3. Average dilation and slip tendency values for all fractures detected in ER-EC-2A (continued).

Depth (ft)	Depth (m)	Azimuth	Dip	Dilation Tendency			Slip Tendency			H
				1.50	2.50	3.20	1.50	2.50	3.20	
2,848.90	868.34	339.17	74.025	0.52	0.48	0.42	0.19	0.32	0.37	1.1
3,033.20	**924.52**	**36.3828**	**59.3237**	**0.74**	**0.74**	**0.74**	**0.32**	**0.59**	**0.73**	**0.5**
3,161.10	963.50	133.715	68.5375	0.36	0.31	0.23	0.09	0.10	0.10	0.8
3,436.80	1,047.54	109.051	74.762	0.44	0.38	0.32	0.13	0.20	0.24	1.1
3,487.80	1,063.08	99.3031	71.9443	0.49	0.45	0.39	0.18	0.30	0.35	1.0
3,492.40	1,064.48	95.2849	71.478	0.52	0.48	0.43	0.20	0.34	0.39	0.9
3,494.90	1,065.25	109.754	69.0497	0.41	0.36	0.29	0.14	0.20	0.23	0.8
3,501.90	1,067.38	86.6993	71.9227	0.60	0.57	0.53	0.23	0.41	0.48	1.0
4,900.60	**1,493.70**	**22.4652**	**69.7412**	**0.85**	**0.84**	**0.83**	**0.27**	**0.55**	**0.71**	**0.8**
4,937.60	1,504.98	13.965	66.3927	0.76	0.75	0.74	0.29	0.55	0.68	0.7
4,941.80	**1,506.26**	**19.3988**	**71.8611**	**0.85**	**0.85**	**0.83**	**0.26**	**0.53**	**0.69**	**0.9**

Table D-4. Average dilation and slip tendency values for all fractures detected in ER-EC-4.

Depth (ft)	Depth (m)	Azimuth	Dip	Dilation Tendency			Slip Tendency			H
				1.50	2.50	3.20	1.50	2.50	3.20	
1,071.50	326.59	86.5792	70.5236	0.59	0.56	0.52	0.23	0.40	0.48	0.9
1,097.10	334.40	279.276	48.0708	0.30	0.28	0.24	0.18	0.26	0.29	0.3
1,107.80	337.66	108.658	47.6202	0.26	0.23	0.19	0.15	0.19	0.21	0.3
1,115.80	340.10	253.959	54.5777	0.53	0.51	0.49	0.28	0.46	0.54	0.4
1,169.30	356.40	262.581	31.8904	0.20	0.19	0.18	0.19	0.27	0.30	0.2
1,275.70	**388.83**	**256.352**	**80.4125**	**0.75**	**0.72**	**0.69**	**0.23**	**0.47**	**0.58**	**1.8**
1,304.70	397.67	294.515	45.3838	0.22	0.19	0.15	0.13	0.15	0.16	0.3
1,334.60	**406.79**	**243.005**	**70.428**	**0.79**	**0.78**	**0.77**	**0.27**	**0.53**	**0.67**	**0.9**
1,777.70	541.84	100.504	28.6041	0.12	0.11	0.10	0.13	0.17	0.18	0.2
1,958.10	596.83	331.25	65.5073	0.42	0.38	0.31	0.17	0.25	0.28	0.7
2,171.00	661.72	138.842	38.7943	0.17	0.15	0.12	0.12	0.13	0.14	0.3
2,171.40	661.84	138.698	49.6828	0.25	0.22	0.17	0.12	0.14	0.16	0.4
2,172.00	662.03	139.11	59.1413	0.32	0.27	0.22	0.12	0.15	0.16	0.5
2,172.20	662.09	150.607	54.1973	0.33	0.30	0.25	0.17	0.23	0.26	0.4
2,234.80	681.17	289.639	55.212	0.32	0.28	0.22	0.15	0.20	0.22	0.4
2,240.10	682.78	127.262	76.6492	0.38	0.33	0.25	0.06	0.07	0.07	1.3
2,240.40	682.87	277.728	56.5732	0.39	0.36	0.31	0.20	0.29	0.33	0.5
2,255.70	687.54	299.326	45.3387	0.22	0.19	0.14	0.12	0.13	0.13	0.3
2,258.50	688.39	288.497	53.2754	0.31	0.27	0.22	0.15	0.20	0.22	0.4
2,411.00	734.87	294.553	78.9101	0.42	0.36	0.29	0.09	0.15	0.16	1.6

Table D-4. Average dilation and slip tendency values for all fractures detected in ER-EC-4 (continued).

Depth (ft)	Depth (m)	Azimuth	Dip	Dilation Tendency			Slip Tendency			H
				1.50	2.50	3.20	1.50	2.50	3.20	
2,433.10	741.61	103.921	71.0972	0.45	0.40	0.34	0.16	0.25	0.29	0.9
2,455.10	748.31	108.831	77.4503	0.45	0.40	0.32	0.12	0.20	0.23	1.4
2,464.30	751.12	270.144	81.8704	0.62	0.58	0.53	0.20	0.37	0.45	2.2
2,489.80	758.89	299.19	79.1574	0.40	0.35	0.27	0.07	0.10	0.11	1.6
2,533.60	772.24	273.585	65.7227	0.49	0.46	0.41	0.21	0.34	0.39	0.7
2,534.00	772.36	157.7	53.4466	0.36	0.33	0.29	0.20	0.28	0.32	0.4
2,561.10	780.62	287.721	66.8585	0.40	0.36	0.30	0.15	0.22	0.24	0.7
2,576.80	785.41	141.133	67.7464	0.38	0.33	0.26	0.12	0.16	0.18	0.8
2,579.50	786.23	115.723	49.4966	0.25	0.22	0.17	0.13	0.15	0.16	0.4
2,637.40	803.88	96.1911	68.8207	0.49	0.45	0.40	0.20	0.32	0.37	0.8
2,698.00	822.35	281.07	82.2711	0.51	0.46	0.40	0.16	0.28	0.32	2.3
2,699.20	822.72	298.335	66.6921	0.35	0.30	0.24	0.10	0.13	0.14	0.7
2,922.90	890.90	85.8407	51.0325	0.41	0.39	0.36	0.24	0.37	0.41	0.4
2,942.50	896.87	79.619	36.1746	0.26	0.25	0.24	0.21	0.31	0.35	0.2
2,952.70	899.98	114.443	60.8997	0.33	0.29	0.23	0.13	0.16	0.18	0.6
2,995.40	913.00	97.7251	51.5873	0.34	0.31	0.28	0.20	0.28	0.31	0.4
3,008.40	**916.96**	**53.4927**	**69.6583**	**0.84**	**0.84**	**0.83**	**0.27**	**0.55**	**0.71**	**0.8**
3,132.20	954.69	116.873	73.0057	0.39	0.34	0.26	0.10	0.13	0.15	1.0
3,134.70	955.46	105.011	63.7626	0.40	0.36	0.30	0.16	0.24	0.27	0.6
3,151.90	960.70	87.5637	42.8041	0.30	0.29	0.26	0.21	0.31	0.35	0.3
3,174.50	967.59	100.682	54.5155	0.35	0.32	0.28	0.19	0.26	0.30	0.4
3,227.00	983.59	115.012	72.5463	0.40	0.34	0.27	0.11	0.15	0.16	1.0
3,268.50	996.24	96.495	59.2481	0.42	0.38	0.34	0.20	0.31	0.35	0.5
3,273.90	997.88	105.655	46.7054	0.26	0.23	0.19	0.16	0.21	0.23	0.3
3,336.40	1,016.93	105.178	60.6507	0.37	0.33	0.28	0.17	0.23	0.27	0.6
3,339.30	1,017.82	63.3424	45.4115	0.46	0.45	0.44	0.29	0.46	0.53	0.3

Table D-5. Average dilation and slip tendency values for all fractures detected in ER-EC-5.

Depth (ft)	Depth (m)	Azimuth	Dip	Dilation Tendency			Slip Tendency			H
				1.5	2.5	3.2	1.5	2.5	3.2	
1,902.80	**579.97**	**58.5325**	**78.497**	**0.93**	**0.92**	**0.92**	**0.20**	**0.45**	**0.60**	**1.5**
1,904.30	**580.43**	**60.7367**	**75.2103**	**0.89**	**0.89**	**0.88**	**0.24**	**0.50**	**0.66**	**1.2**
1,905.10	**580.67**	**57.1877**	**78.5285**	**0.93**	**0.93**	**0.93**	**0.20**	**0.44**	**0.59**	**1.5**
1,911.00	**582.47**	309.293	76.2408	0.39	0.33	0.25	0.06	0.08	0.08	1.3
1,914.20	**583.45**	**63.5129**	**74.1999**	**0.87**	**0.86**	**0.85**	**0.25**	**0.52**	**0.67**	1.1
1,920.80	**585.46**	**53.7976**	**70.5561**	**0.88**	**0.88**	**0.87**	**0.26**	**0.54**	**0.70**	**0.9**
1,973.30	601.46	146.218	63.94	0.35	0.30	0.24	0.12	0.15	0.17	0.6
1,974.00	601.68	133.322	59.469	0.30	0.26	0.19	0.10	0.10	0.10	0.5
1,974.70	601.89	115.515	57.6974	0.33	0.30	0.24	0.15	0.20	0.22	0.5
1,993.70	607.68	101.051	61.4249	0.45	0.42	0.37	0.21	0.33	0.37	0.6
1,995.70	608.29	132.802	69.4801	0.35	0.30	0.23	0.08	0.08	0.09	0.8
2,005.00	611.12	84.5885	73.9767	0.69	0.67	0.63	0.25	0.47	0.57	1.1
2,025.20	617.28	300.03	85.4627	0.44	0.38	0.30	0.09	0.15	0.17	3.9
2,071.40	631.36	145.659	69.9089	0.38	0.33	0.26	0.10	0.14	0.16	0.9
2,074.20	632.22	295.661	63.7663	0.37	0.33	0.27	0.14	0.20	0.23	0.6
2,076.10	632.80	279.721	51.1771	0.36	0.34	0.30	0.21	0.31	0.35	0.4
2,088.50	**636.57**	**64.3393**	**77.8236**	**0.89**	**0.88**	**0.87**	**0.22**	**0.49**	**0.64**	**1.4**
2,106.10	**641.94**	**62.3229**	**67.4468**	**0.81**	**0.80**	**0.79**	**0.29**	**0.56**	**0.71**	**0.7**
2,107.00	**642.21**	**52.2667**	**73.0643**	**0.91**	**0.91**	**0.90**	**0.24**	**0.51**	**0.67**	**1.0**
2,109.60	643.01	50.1744	56.2925	0.69	0.69	0.69	0.33	0.59	0.71	0.5
2,226.20	678.55	286.457	46.4335	0.28	0.26	0.22	0.18	0.25	0.27	0.3
2,227.40	678.91	274.53	49.7922	0.38	0.36	0.33	0.23	0.34	0.39	0.4
2,228.50	679.25	236.626	51.111	0.59	0.59	0.59	0.32	0.55	0.65	0.4
2,229.30	679.49	236.201	44.4333	0.48	0.48	0.48	0.31	0.50	0.58	0.3
2,230.20	679.76	236.132	48.944	0.56	0.56	0.55	0.32	0.53	0.63	0.4
2,231.50	680.16	263.773	51.6999	0.47	0.46	0.43	0.27	0.43	0.49	0.4
2,236.60	681.72	269.153	69.3003	0.62	0.59	0.55	0.25	0.43	0.52	0.8
2,238.30	682.23	290.736	65.3766	0.41	0.37	0.31	0.16	0.25	0.28	0.7
2,453.90	**747.95**	**73.004**	**80.4574**	**0.84**	**0.83**	**0.80**	**0.23**	**0.49**	**0.63**	**1.9**
2,454.90	748.25	268.482	83.1226	0.70	0.67	0.63	0.22	0.44	0.53	2.6
2,459.80	749.75	266.984	78.5776	0.70	0.67	0.63	0.23	0.45	0.55	1.5
2,462.80	750.66	277.252	72.5614	0.57	0.53	0.48	0.21	0.37	0.43	1.0
2,467.30	**752.03**	**56.5914**	**79.4203**	**0.94**	**0.94**	**0.94**	**0.19**	**0.42**	**0.58**	**1.7**
2,468.50	**752.40**	**257.806**	**81.6402**	**0.80**	**0.78**	**0.75**	**0.23**	**0.49**	**0.61**	**2.1**
2,470.60	**753.04**	**257.499**	**84.5518**	**0.81**	**0.79**	**0.77**	**0.22**	**0.48**	**0.61**	**3.3**

Table D-6. Average dilation and slip tendency values for all fractures detected in ER-EC-6.

Depth (ft)	Depth (m)	Azimuth	Dip	Dilation Tendency			Slip Tendency			H
				1.5	2.5	3.2	1.5	2.5	3.2	
1,631.70	497.34	279.78	76.5512	0.53	0.49	0.43	0.19	0.32	0.37	1.3
1,713.60	522.31	304.575	34.9343	0.13	0.11	0.09	0.10	0.11	0.11	0.2
1,719.90	524.23	118.201	60.0752	0.32	0.28	0.22	0.12	0.16	0.17	0.5
1,723.20	525.23	268.56	77.4313	0.64	0.61	0.56	0.22	0.41	0.49	1.4
1,735.90	529.10	269.134	74.7535	0.62	0.59	0.54	0.23	0.41	0.48	1.1
1,788.20	**545.04**	**230.372**	**64.5923**	**0.81**	**0.81**	**0.80**	**0.30**	**0.58**	**0.73**	**0.7**
1,828.20	557.24	279.888	53.6649	0.37	0.34	0.30	0.20	0.29	0.33	0.4
1,925.60	586.92	279.423	63.1967	0.45	0.41	0.36	0.20	0.31	0.36	0.6
1,961.30	597.80	60.3719	57.7525	0.67	0.66	0.66	0.31	0.56	0.68	0.5
2,168.90	661.08	281.015	44.1043	0.27	0.25	0.22	0.18	0.25	0.28	0.3
2,415.20	**736.15**	**252.78**	**75.845**	**0.78**	**0.77**	**0.74**	**0.25**	**0.50**	**0.63**	**1.2**
2,415.30	**736.18**	**248.688**	**73.1419**	**0.80**	**0.78**	**0.77**	**0.26**	**0.52**	**0.66**	**1.0**
2,417.90	**736.98**	**243.318**	**72.2519**	**0.83**	**0.82**	**0.81**	**0.26**	**0.53**	**0.68**	**1.0**
2,419.10	**737.34**	**244.87**	**78.4894**	**0.87**	**0.86**	**0.84**	**0.23**	**0.50**	**0.65**	**1.5**
2,419.40	**737.43**	**247.955**	**79.7775**	**0.85**	**0.83**	**0.82**	**0.23**	**0.49**	**0.64**	**1.7**
2,441.30	744.11	275.498	68.0003	0.52	0.48	0.43	0.21	0.35	0.41	0.8
2,641.00	804.98	243.191	47.7077	0.50	0.50	0.49	0.30	0.49	0.57	0.3
2,754.50	839.57	160.556	58.2931	0.40	0.37	0.32	0.20	0.30	0.33	0.5
3,131.40	954.45	324.323	50.0775	0.26	0.22	0.18	0.13	0.16	0.17	0.4
3,224.30	982.77	277.885	65.2441	0.48	0.44	0.39	0.21	0.33	0.38	0.7
3,231.00	984.81	266.728	82.9323	0.68	0.65	0.60	0.22	0.43	0.51	2.5
3,235.20	986.09	261.068	81.6728	0.73	0.71	0.67	0.23	0.46	0.57	2.1
3,292.10	1,003.43	267.669	78.9038	0.65	0.62	0.58	0.22	0.42	0.50	1.6
3,328.90	1,014.65	51.9803	56.986	0.69	0.69	0.69	0.32	0.58	0.70	0.5
3,531.70	1,076.46	253.904	70.9996	0.74	0.72	0.69	0.27	0.51	0.63	0.9
3,556.10	1,083.90	267.641	78.0425	0.65	0.62	0.58	0.22	0.42	0.50	1.5
3,688.70	1,124.32	284.428	78.4283	0.50	0.45	0.39	0.16	0.27	0.31	1.5
3,802.80	1,159.09	263.577	56.4757	0.51	0.49	0.46	0.26	0.43	0.49	0.5
3,863.80	1,177.69	272.648	44.7194	0.32	0.30	0.27	0.21	0.31	0.35	0.3
4,039.20	1,231.15	71.9637	43.7646	0.41	0.40	0.39	0.27	0.42	0.49	0.3
4,156.30	**1,266.84**	**254.922**	**77.2982**	**0.77**	**0.75**	**0.73**	**0.24**	**0.49**	**0.62**	**1.4**
4,424.80	1,348.68	48.2538	57.3881	0.70	0.70	0.70	0.32	0.59	0.72	0.5
4,425.80	1,348.98	46.9351	58.7777	0.73	0.73	0.73	0.32	0.59	0.73	0.5
4,428.00	1,349.65	58.3943	62.1439	0.74	0.74	0.73	0.31	0.57	0.71	0.6
4,625.40	1,409.82	272.62	67.8221	0.54	0.51	0.46	0.23	0.38	0.44	0.8
4,655.10	1,418.87	177.079	60.3613	0.55	0.53	0.49	0.26	0.43	0.50	0.5

Table D-7. Average dilation and slip tendency values for all fractures detected in ER-EC-7.

Depth	Azimuth	Dip	Dilation Tendency			Slip Tendency			H
			1.5	2.5	3.2	1.5	2.5	3.2	
930.3	**52.99**	**74.9875**	**0.92**	**0.92**	**0.92**	**0.23**	**0.48**	**0.65**	**1.2**
936.6	65.3984	62.0685	0.71	0.71	0.70	0.30	0.56	0.68	0.6
939.4	75.0804	68.0329	0.71	0.70	0.68	0.28	0.52	0.63	0.8
1,005.00	**67.1157**	**75.118**	**0.84**	**0.83**	**0.82**	**0.25**	**0.52**	**0.66**	**1.2**
1,030.10	**246.077**	**72.4376**	**0.82**	**0.82**	**0.81**	**0.26**	**0.53**	**0.68**	**1.0**
1,061.90	**230.528**	**78.6985**	**0.96**	**0.95**	**0.95**	**0.18**	**0.40**	**0.55**	1.6
1,065.40	**248.908**	**75.8035**	**0.83**	**0.82**	**0.81**	**0.25**	**0.51**	**0.66**	**1.2**
1,221.40	109.307	66.8645	0.42	0.38	0.32	0.16	0.25	0.28	0.7
1,232.20	119.093	68.9469	0.38	0.33	0.26	0.12	0.16	0.18	0.8
1,271.00	123.338	54.9708	0.28	0.25	0.19	0.12	0.14	0.14	0.4
1,273.70	68.0615	63.3488	0.71	0.71	0.69	0.30	0.55	0.67	0.6
1,275.60	**62.5216**	**77.9446**	**0.89**	**0.89**	**0.88**	**0.22**	**0.49**	**0.65**	**1.5**
1,276.90	303.357	56.423	0.29	0.25	0.20	0.12	0.14	0.14	0.5
1,277.70	310.772	50.3526	0.24	0.21	0.15	0.11	0.11	0.11	0.4
1,299.40	297.313	72.866	0.41	0.36	0.28	0.12	0.17	0.20	1.0

Table D-8. Average dilation and slip tendency values for all fractures detected in ER-EC-8.

Depth (ft)	Depth (m)	Azimuth	Dip	Dilation Tendency			Slip Tendency			H
				1.5	2.5	3.2	1.5	2.5	3.2	
684.8	208.72704	313.321	53.3116	0.26	0.23	0.17	0.11	0.12	0.12	0.4
685.3	208.87944	289.008	66.8195	0.40	0.36	0.30	0.15	0.22	0.25	0.7
689.2	210.06816	295.017	62.703	0.35	0.30	0.24	0.13	0.17	0.19	0.6
698.4	212.87232	305.324	68.6867	0.35	0.30	0.23	0.09	0.09	0.09	0.8
707	215.4936	290.815	73.2495	0.43	0.38	0.31	0.13	0.20	0.23	1.0
724.5	220.8276	288.331	82.3741	0.47	0.42	0.35	0.13	0.22	0.26	2.3
734.7	223.93656	106.358	75.5257	0.47	0.42	0.35	0.15	0.24	0.28	1.2
754.9	230.09352	111.906	66.4745	0.38	0.34	0.27	0.14	0.20	0.22	0.7
755.8	230.36784	90.9837	81.8022	0.62	0.59	0.54	0.21	0.39	0.46	2.2
767.3	233.87304	83.9557	77.3837	0.67	0.64	0.61	0.23	0.44	0.53	1.4
817.6	249.20448	102.256	82.2291	0.52	0.47	0.40	0.16	0.28	0.33	2.3
829.7	**252.89256**	**70.0553**	**78.1867**	**0.81**	**0.80**	**0.77**	**0.24**	**0.50**	**0.63**	**1.5**
837.6	255.30048	142.371	67.0299	0.37	0.32	0.25	0.12	0.16	0.17	0.7
843.1	256.97688	136.407	66.0997	0.35	0.30	0.23	0.10	0.11	0.12	0.7
849.8	259.01904	130.177	59.7373	0.30	0.26	0.19	0.10	0.10	0.10	0.5
887.4	270.47952	96.51	63.2978	0.47	0.43	0.38	0.21	0.33	0.38	0.6
917.9	279.77592	113.869	56.7471	0.31	0.28	0.22	0.14	0.18	0.20	0.5

Table D-8. Average dilation and slip tendency values for all fractures detected in ER-EC-8 (continued).

Depth (ft)	Depth (m)	Azimuth	Dip	Dilation Tendency			Slip Tendency			H
				1.5	2.5	3.2	1.5	2.5	3.2	
922	281.0256	129.042	58.2364	0.29	0.25	0.19	0.10	0.10	0.10	0.5
935.7	285.20136	116.368	62.8878	0.35	0.30	0.23	0.12	0.16	0.17	0.6
1,109.20	338.08416	262.905	72.8321	0.66	0.63	0.59	0.25	0.45	0.54	1.0
1,110.30	338.41944	259.882	81.2685	0.73	0.71	0.68	0.23	0.46	0.57	2.0
1,184.20	360.94416	285.254	60.7119	0.38	0.34	0.29	0.17	0.25	0.28	0.6
1,284.20	391.42416	80.2039	82.8595	0.73	0.71	0.68	0.23	0.46	0.57	2.5
1,521.60	463.78368	288.987	69.0085	0.42	0.37	0.31	0.14	0.22	0.25	0.8
1,524.50	464.6676	67.0223	59.9534	0.66	0.65	0.64	0.30	0.53	0.64	0.5
1,527.00	465.4296	252.111	45.1297	0.42	0.41	0.40	0.28	0.42	0.49	0.3
1,528.80	465.97824	275.054	69.9826	0.53	0.49	0.44	0.21	0.35	0.40	0.9
1,529.60	466.22208	69.1546	42.1973	0.39	0.38	0.37	0.27	0.42	0.48	0.3
1,565.30	**477.10344**	**59.0915**	**74.1584**	**0.86**	**0.86**	**0.85**	**0.25**	**0.52**	**0.67**	**1.1**
1,567.00	**477.6216**	**63.9459**	**70.9333**	**0.81**	**0.80**	**0.78**	**0.27**	**0.54**	**0.68**	**0.9**
1,623.60	494.87328	255.533	72.3515	0.72	0.70	0.68	0.26	0.49	0.61	1.0
1,645.10	501.42648	265.903	62.8	0.55	0.52	0.48	0.25	0.42	0.48	0.6
1,646.60	501.88368	274.071	63.787	0.49	0.45	0.41	0.22	0.35	0.40	0.6
1,701.90	**518.73912**	**222.03**	**75.8007**	**0.94**	**0.94**	**0.94**	**0.21**	**0.44**	**0.60**	**1.2**
1,751.90	533.97912	246.168	57.9275	0.63	0.62	0.62	0.31	0.53	0.63	0.5
1,761.30	536.84424	240.847	46.3234	0.49	0.48	0.47	0.30	0.49	0.56	0.3
1,907.10	581.28408	**58.9706**	**76.8025**	**0.89**	**0.88**	**0.87**	**0.23**	**0.50**	**0.65**	**1.3**
1,915.70	583.90536	**43.5345**	**77.0847**	**0.95**	**0.95**	**0.95**	**0.19**	**0.42**	**0.57**	**1.4**
1,921.60	585.70368	62.7976	59.8457	0.68	0.67	0.66	0.31	0.55	0.66	0.5
1,924.10	586.46568	**49.2962**	**70.5508**	**0.88**	**0.87**	**0.87**	**0.26**	**0.54**	**0.70**	**0.9**
1,931.30	588.66024	**55.4193**	**69.4924**	**0.84**	**0.84**	**0.83**	**0.27**	**0.55**	**0.71**	**0.8**
1,949.60	594.23808	36.8641	55.576	0.68	0.68	0.68	0.33	0.58	0.71	0.5
1,961.20	597.77376	260.068	69.0061	0.65	0.63	0.60	0.26	0.47	0.56	0.8
1,987.00	605.6376	79.7138	83.8919	0.74	0.72	0.69	0.22	0.46	0.57	2.9

STANDING DISTRIBUTION LIST

Wilhelm Wilborn
UGTA Activity Lead
Nevada Field Office
National Nuclear Security Administration
U.S. Department of Energy
P.O. Box 98518
Las Vegas, NV 89193-8518
Bill.Wilborn@nnsa.doe.gov

Sarah Hammond, Contracting Officer
Office of Acquisition Management
NNSA Service Center
Pennsylvania and H Street, Bldg. 20388
P.O. Box 5400
Albuquerque, NM 87185-5400
Sarah.Hammond@nnsa.doe.gov

Chuck Russell
Division of Hydrologic Sciences
Desert Research Institute
755 E. Flamingo Road
Las Vegas, NV 89119-7363
Chuck.Russell@dri.edu

Jenny Chapman
DOE Program Manager
Division of Hydrologic Sciences
Desert Research Institute
755 E. Flamingo Road
Las Vegas, NV 89119-7363
Jenny.Chapman@dri.edu

*****Nevada State Library and Archives
State Publications
100 North Stewart Street
Carson City, NV 89701-4285

Irene Farnham
Navarro
P.O. Box 98952
M/S NSF167
Las Vegas, NV 89193-8952
Irene.Farnham@nv.doe.gov

Kay Birdsell
Los Alamos National Laboratory
P.O. Box 1663 M/S T003
Los Alamos, NM 87544
khb@lanl.gov

P.K. Ortego
National Security Technologies, LLC
P.O. Box 98521
M/S NLV082
Las Vegas, NV 89193-8521
ortegopk@nv.doe.gov

Andy Tompson
Lawrence Livermore National Laboratory
P.O. Box 808, L-231
Livermore, CA 94551-0808
Tompson1@llnl.gov

Jeffrey Sanders
U.S. Geological Survey
Nevada Water Science Center
160 N. Stephanie St.
Henderson, NV 89074-8829
jvsanders@usgs.gov

Ken Rehfeldt
Navarro
P.O. Box 98952
M/S NSF 167
Las Vegas, NV 89193-8952
Ken.Rehfeldt@nv.doe.gov

Brian Haight
Navarro
P.O. Box 98952
M/S NSF 167
Las Vegas, NV 89193-8952
Brian.Haight@nv.doe.gov

Archives Getchell Library
University of Nevada, Reno
1664 N. Virginia St.
Reno, NV 89557
dcurtis@unr.edu

DeLaMare Library/262
University of Nevada, Reno
1664 N. Virginia St.
Reno, NV 89557
dcurtis@unr.edu

Document Section, Library
University of Nevada, Las Vegas
4505 Maryland Parkway
Las Vegas, NV 89154
sue.wainscott@unlv.edu

†Library
Southern Nevada Science Center
Desert Research Institute
755 E. Flamingo Road
Las Vegas, NV 89119-7363

‡Nuclear Testing Archive
ATTN: Martha DeMarre
National Security Technologies, LLC
Mail Stop 400
PO Box 98521
Las Vegas, NV 89193-8521
demarrme@nv.doe.gov
(2 CDs)

ʃOffice of Scientific and Technical Information
U.S. Department of Energy
P.O. Box 62
Oak Ridge, TN 37831-9939

All on distribution list receive one electronic PDF copy, unless otherwise noted.

***** 12 paper copies
† 3 paper copies; CD with pdf (from which to print)
‡ compact disc only
ʃ electronic copy (pdf) only